

ABSTRACT

Title of Document: MOLECULAR DYNAMICS STUDIES OF METALLIC NANOPARTICLES

Brian John Henz, Ph.D., 2009

Directed By: Professor Michael R. Zachariah, Departments of Mechanical Engineering and Chemistry

Metal nanoparticles have many desirable electrical, magnetic, optical, chemical, and physical properties. In order to utilize these properties effectively it is necessary to be able to accurately predict their size-dependent properties. One common method used to predict these properties is with numerical simulation. The numerical simulation technique used throughout this effort is the molecular dynamics (MD) simulation method. Using MD simulations I have investigated various metallic nanoparticle systems including gold nanoparticles coated with an organic self-assembled monolayer (SAM), the self-propagating high-temperature synthesis (SHS) reaction of nickel and aluminum nanoparticles, and the mechano-chemical behavior of oxide coated aluminum nanoparticles. The model definition, boundary conditions, and results of these simulations are presented in the following dissertation.

In the first material system investigated MD simulations are used to probe the structure and stability of alkanethiolate self-assembled monolayers (SAMs) on gold nanoparticles. Numerous results and observations from this parametric study are presented here. By analyzing the mechanical and chemical properties of gold nanoparticles at temperatures below the melting point of gold, with different SAM chain lengths and surface coverage properties, we have determined that the material system

is metastable. The model and computational results that provide support for this hypothesis are presented.

The second material system investigated, namely sintering of aluminum and nickel, is explored in chapter 4. In this chapter MD simulations are used to simulate the kinetic reaction of Ni and Al particles at the nanometer scale. The affect of particle size on reaction time and temperature for separate nanoparticles has been considered as a model system for a powder metallurgy process. Coated nanoparticles in the form of Ni-coated Al nanoparticles and Al-coated Ni nanoparticles are also analyzed as a model for nanoparticles of one material embedded within a matrix of the second. Simulation results show that the sintering time for separate and coated nanoparticles is dependent upon the number of atoms or volume of the sintering nanoparticles and their surface area. We have also found that nanoparticle size and surface energy is an important factor in determining the adiabatic reaction temperature for both systems, coated and separate, at nanoparticle sizes of less than 10nm in diameter.

The final material system investigated in chapters 5 and 6 is the oxide coated aluminum nanoparticle. This material system is simulated using the reactive force field (ReaxFF) potential which is capable of considering the charge transfer that occurs during oxidation. The oxidation process of oxide coated aluminum nanoparticles has been observed to occur at a lower temperature and a faster rate than micron sized nanoparticles, suggesting a different oxidation mechanism. From this effort we have discovered that the oxidation process for nanometer sized oxide coated aluminum particles is the result of an enhanced transport due to a built-in electric field induced by the oxide shell. In contrast to the currently assumed pressure driven diffusion

process the results presented here demonstrate that the high temperature oxidation process is driven by the electric field present in the oxide layer. This electric field accounts for over 90% of the mass flux of aluminum ions through the oxide shell. The computed electric fields show good agreement with published theoretical and experimental results.

The final chapter includes some important conclusions from this work and highlights some future work in these areas. Future work that is outlined includes efforts that are currently underway to analyze the interactions of multiple alkanethiolate coated gold nanoparticles in vacuum and in solvent. Other future efforts are farther out over the horizon and include using advanced computing techniques such as general purpose graphical processing units (GPGPU) to expand simulation sizes and physical details over what it is currently possible to simulate.

MOLECULAR DYNAMICS STUDIES OF METALLIC NANOPARTICLES

By

Brian John Henz

Thesis submitted to the Faculty of the Graduate School of the
University of Maryland, College Park, in partial fulfillment
of the requirements for the degree of
Doctor of Philosophy
2009

Advisory Committee:

Dr. Michael R. Zachariah, Chair

Dr. John D. Weeks

Dr. Philip DeShong

Dr. Bryan Eichhorn

Dr. Gregory S. Jackson

Dr. Raju Namburu

© Copyright by
Brian John Henz
2009

To

My family Donna, Emory, and Baby,
my parents Kevin and Linda,
and my brother Barry.

I could not have completed this effort without your unending love and unwavering support.

Acknowledgement

First and foremost, I would like to thank my PhD advisor, Professor Michael R. Zachariah, for guiding me during my research. This collaboration has provided me with the background required to pursue original research in the fascinating areas of nanoparticles and energetic materials.

I would also like to acknowledge the support of the U.S. Army Materiel Command and the U.S. Army Research Laboratory who provided the financial and logistical support for me to investigate new research directions while completing this degree. Individually, I would like to recognize the initial support by Dr. Andrew Mark who provided me with the assistance required to start down this path. I would also like to acknowledge the continued support of Mr. Charles Nietubicz and Dr. Jay Gowens without whose support I would not have been able to bring this effort to completion. Others whose discussions and comments have proved invaluable include Mr. Dale Shires and Dr. Peter Chung.

I would like to acknowledge the guidance provided by Dr. Takumi Hawa with whom I worked closely during nearly the entire process and who provided many useful insights and suggestions. Our collaborations have resulted in the bulk of material found in this dissertation.

I would also like to thank Professors John D. Weeks, Philip DeShong, Bryan Eichhorn, Gregory S. Jackson and Dr. Raju Namburu for serving on my Ph.D. committee.

Table of Contents

1	Introduction	1
1.1	Nanoparticles	1
1.1.1	Metal Nanoparticles	2
1.2	Self-Assembled Monolayers	2
1.3	Self-Propagating High-Temperature Synthesis (SHS)	3
1.4	Combustion of Oxide-Coated Nanoparticles	3
1.5	Organization of this Dissertation	4
2	Simulation Details	6
2.1	Molecular Dynamics	6
2.2	Software	7
2.2.1	Parallel Processing	7
2.2.2	Applications and Code Development	8
2.3	Empirical Potentials	10
2.3.1	Alkanethiolate Coated Gold Nanoparticle	10
2.3.2	The Energetic Sintering Reaction of Nickel and Aluminum	18
2.3.3	Oxidation of Oxide Coated Aluminum Nanoparticle	20
2.3.4	Computation of System Properties	21
2.3.5	Pair Correlation Function	22
2.3.6	Radial Pressure Distribution	22
2.3.7	Surface Tension	25
2.3.8	Heat Capacity	26
2.3.9	Electric Field	27
3	Mechano-Chemical Stability of Gold Nanoparticles Coated with Alkanethiolate SAMs	28
3.1	Introduction	28
3.2	Background	28
3.3	Computational Modeling and Numerical Procedure	30
3.3.1	Simulating the Gold Substrate	31
3.3.2	Modeling the Alkanethiolate Chain	32
3.3.3	Binding of Sulfur to Gold	33
3.4	Simulation Results	34
3.4.1	Pair Correlation Function	36
3.4.2	Diffusion	39
3.4.3	Radial Pressure Distribution	44
3.4.4	Radial Density Distribution	52
3.5	Phase Behavior and SAM Solubility	56
3.6	SAM Phases	62
3.7	Conclusions	65
4	Molecular Dynamics Simulation of the Energetic Reaction of Ni and Al Nanoparticles	67

4.1	Introduction.....	67
4.2	Simulation Approach	68
4.3	Thermodynamic Analysis of Separate Nanoparticles.....	69
4.4	The Coalescence Processes.....	73
4.5	Phenomenological Model of Nanoparticle Reactive Sintering.....	76
4.6	MD Simulation Results of Separate Nanoparticle Reactivity.....	85
4.6.1	Analysis of Alloy Formation	88
4.7	Reactive Sintering of Core-Shell Nanoparticles	91
4.7.1	Aluminum Coated Nickel	91
4.7.2	Nickel Coated Aluminum	95
4.8	Conclusions.....	98
5	On the Role of Built-in Electric Fields on Oxidation of Oxide Coated NanoAluminum: ion mobility versus Fickian Diffusion	100
5.1	Introduction.....	100
5.2	Simulation Approach	101
5.3	Model Description	102
5.4	Results of Rapid Heating Simulations	104
5.5	Aluminum Cation Diffusion through the Oxide Shell.....	106
5.6	Induced Electric Field in Oxide Shell.....	110
5.7	Formation of Hollow Aluminum Oxide Shells.....	119
5.8	Conclusions.....	121
6	Computer Simulation of the Mechano-Chemical Behaviour of Oxide Coated Aluminum Nanoparticles	123
6.1	Introduction.....	123
6.2	Simulation Approach	125
6.3	Model Description	125
6.4	Results of Homogeneous Heating Simulation	127
6.5	Heterogeneous Laser Heating	129
6.6	Aluminum Ion Diffusion through the Oxide Shell	131
6.7	Computed Stress in Oxide Shell	134
6.8	Laser Heating Simulations.....	137
6.9	Analysis of the Size Dependency of Core Pressure.....	142
6.10	Conclusions.....	143
7	Conclusions and Future Work	145
7.1	Conclusions.....	145
7.2	Future Work	147
8	References	150

List of Tables

Table 2.1. Computed corrugation factors for alkanethiolate SAM coated gold nanoparticles.	16
Table 3.1. Computed corrugation factors for alkanethiolate SAM coated gold nanoparticles.	54
Table 4.1: Change in surface energy versus nanoparticle size.	72
Table 4.2: Computed adiabatic temperature versus nanoparticle radius, including contact of flat surfaces or infinitely sized spheres.	73
Table 5.1: Effective diffusion coefficients for core aluminum atoms with various oxide shell configurations. The effective diffusion coefficients are for general diffusion (D_{eff}) and radial diffusion (D_{radial}).	107
Table 5.2: Total charge of aluminum core and associated electric field are given here for all of the core/shell configurations considered. Note on electric field units, $N/C = 0.01 \text{ V/m}$	113
Table 5.3: Diffusion coefficient and mass flux computed at 600K, 1000K, and 2000K for all shell configurations with the 5.6nm core unless noted. The last column labeled Ratio J_e to J , is the fraction of the total mass flux due to the induced electric field, with the balance due to the concentration gradient and drift velocities.	117

List of Figures

Figure 2.1: Example metal potentials from LAMMPS. ⁹ Distances are measured in Angstroms (Å) and energy is given in electron volts (eV).	12
Figure 2.2: Published potential energy functions for Au-S binding. All units are in Angstroms (Å) or electron volts (eV)	15
Figure 2.3: Sample alkanethiolate chain with 8 carbon atoms along the backbone. ..	17
Figure 2.4: Finnis-Sinclair EAM potential data for the nickel/aluminum system. Distances are measured in Angstroms (Å) and energy is given in electron volts (eV).	19
Figure 2.5: Circle used in computing radial pressure using the Irving-Kirkwood tensor.	24
Figure 3.1: Sample alkanethiolate chain with 8 carbon atoms along the backbone. ..	33
Figure 3.2: a) Pair correlation function for bare 50Å gold nanoparticle. Note the change in shape and the location of peaks between 900 K and 1000 K. b) Pair correlation function results for the gold atoms in a 50Å gold nanoparticle coated with an alkanethiolate SAM at various temperatures with a sulfur binding energy of 184 kJ/mol. c) The pair correlation function results for the SAM coated gold nanoparticle with the lower sulfur binding energy of 126 kJ/mol. d) a comparison of the pair correlation results at 500 K for the bare nanoparticle and high (184 kJ/mol) and low (126 kJ/mol) alkanethiol binding energies.	37
Figure 3.3: a) Arrhenius plot of diffusivity for sulfur atoms. The activation energy for SAM mobility is estimated by the slope of ln(D) vs. 1/T between 100 K and 800 K. b) Ratio of sulfur diffusivity to gold diffusivity in the alkanethiol coated gold nanoparticle material system.	42
Figure 3.4: Radial pressure distribution for 50Å gold nanoparticle at various temperatures.	45
Figure 3.5: Radial pressure distribution for 50Å gold nanoparticle with alkanethiolate SAMs with differing interaction coefficients.	48
Figure 3.6: Radial pressure distribution for fully coated gold nanoparticle for range of temperatures with high binding energy (184.1 kJ/mol).	50
Figure 3.7: Radial pressure distribution for alkanethiol coated 50Å gold nanoparticle with 126 kJ/mol sulfur-gold binding energy.	51
Figure 3.8: Radial density of gold in alkanethiolate SAM coated gold nanoparticle for various surface coverage amounts.	53

Figure 3.9: Potential energy versus temperature for the alkanethiolate SAM coated gold nanoparticle with various amount of surface coverage and the 184 kJ/mol sulfur binding energy.	58
Figure 3.10: Cross section of 100% coated gold nanoparticle at 300K (a) and 600K (b), showing the dissolution of the alkanethiol chains at high temperatures. In these images the blue spheres represent gold atoms, light blue are sulfur, yellow are CH ₂ and red spheres represent CH ₃	59
Figure 3.11: a) Potential energy versus temperature for the alkanethiolate SAM coated gold nanoparticle with various amount of surface coverage and 126 kJ/mol binding energy. b) Comparison of potential energy versus temperature for fully coated nanoparticle with 184 kJ/mol and 126 kJ/mol binding energy.....	59
Figure 3.12: Plot of specific heat versus surface coverage for alkanethiolate SAM-coated gold nanoparticle showing exponential relationship between specific heat and surface coverage.....	61
Figure 3.13: Difference in radial position for the head and tail groups of the alkanethiolate chains at various surface coverage densities, drawing (a) and tilt angle (θ) (b). The alkanethiol radius is also labeled as the monolayer thickness.....	63
Figure 3.14: Drawing showing the difference in space occupied by tail molecule on curved and flat gold surfaces. Assuming a chain length of 9 carbon atoms.	64
Figure 4.1: Illustration of coalescence process showing liquid Al nanoparticle first coating the solid Ni nanoparticle and then complete alloying after the Ni nanoparticle has melted.	74
Figure 4.2: Illustration of parameters used in analytical model of reactive coalescence of Ni and Al nanoparticles.	77
Figure 4.3: a) Plot of exposed Ni and Al nanoparticle surface area as a function of distance between nanoparticle centers. b) Plot of total exposed surface area as a function of distance between nanoparticle centers. These results assume a Ni nanoparticle of radius 4.53 nm and an Al nanoparticle of 5.23 nm. Notice that the total exposed surface area is monotonically decreasing, indicating that the surface energy is also decreasing monotonically	79
Figure 4.4: Contact or interface area as a function of center-to-center distance. The contact area is increasing as the nanoparticles move closer together (right to left on x-axis).....	80
Figure 4.5: Total system surface area versus time from mathematical model and MD simulations for the sintering of 10nm diameter nanoparticles, where the final surface area of the NiAl nanoparticle is approximately 480 nm ²	82

Figure 4.6: Cross sectional view from MD simulations of Ni/Al nanoparticle sintering process showing the start of the second stage of coalescence where diffusion is the driving force as opposed to contact area maximization. Aluminum atoms are blue and nickel atoms are red.	83
Figure 4.7: Time versus temperature plot for sintering of separate 10nm diameter Al and Ni nanoparticles. The various stages of the coalescence processes are denoted on the curve, including the final completion stage that occurs after the Ni nanoparticle has melted.	85
Figure 4.8: Temperature versus time in the sintering of nanoparticles with an Ni:Al ratio of 1:1. The subscripts in the legend refer to the number of atoms of each material and correspond to nanoparticles of diameter approximately 3nm, 5nm, and 10nm. The color coded dashed lines are the computed adiabatic temperature from the thermodynamic analysis. The black dashed line is the predicted temperature for coalescence of bulk Al and Ni.	86
Figure 4.9: Reaction time versus Al nanoparticle diameter (a), Al nanoparticle surface area (b), and number of Al atoms (c). Note the nearly linear relationship (dashed line) of reaction time between number of atoms (volume) and surface area.	87
Figure 4.10: Fraction of all atoms in each compound versus fraction of Ni in compound. i.e. a data point at (0.1, 0.25) corresponds to 10% of all atoms in the system belong to the Al ₃ Ni compound.	89
Figure 4.11: Plot showing spatial distribution of Ni fractions during stages 1 and 2 of the sintering process.	90
Figure 4.12: Plot showing spatial distribution of Ni fractions during stage 3 of the sintering process.	91
Figure 4.13: Temperature versus time in the sintering of Al-coated Ni nanoparticles with an Ni:Al ratio of 1:1.	92
Figure 4.14: Comparison of thermodynamically determined adiabatic temperature for Al-coated Ni nanoparticle and results from MD simulation.	94
Figure 4.15: Reaction time versus number of Al atoms in the Al-coated Ni nanoparticle system.	94
Figure 4.16: Comparison of combustion temperature for Ni-coated Al nanoparticle versus Al-coated Ni nanoparticle.	97
Figure 4.17: Cross sections of the Ni-coated Al nanoparticle simulation model just after melting of the Al core for the 1nm (a) and 2nm (b) thick Ni shells.	98
Figure 5.1: Cross sections of some of the oxide coated aluminum nanoparticle models used in this work. a) 1nm thick, dense oxide shell. b) 1nm thick, crystalline oxide	

shell. c) 2nm thick, amorphous oxide shell. d) 2nm thick, dense oxide shell with 2:2.7 Al:O ratio. Blue spheres represent oxygen atoms and yellow spheres denote aluminum atoms.....	102
Figure 5.2: Cross section of an 8.2nm Al core with 2nm thick crystalline oxide shell. Yellow denotes Al atoms and oxygen atoms are blue.	102
Figure 5.3: Plot showing diffusion of aluminum cations (blue) through the 1nm thick oxide shell (red) as the temperature increases from 300K to 1000K and held for 100 ps.	105
Figure 5.4: Arrhenius plot of $\ln(D)$ versus $1/T$, where D is the diffusivity of the core aluminum atoms. The slope of this plot is the activation energy required for diffusion of aluminum cations and shows an expected decrease above the melting point of the core, at approximately 0.001/K.....	109
Figure 5.5: Radial charge distribution through the oxide shell for a 1nm (a) thick shell and a 2nm (b) thick shell.....	111
Figure 5.6: Schematic of assumed charge distributions affecting electric field around core surface aluminum atoms.	112
Figure 5.7: Electric field (N/C) at each of the core Al atoms in the nanoparticle core computed using Coulomb's Law. These results are for the 5.6nm core with a 2nm thick crystalline shell. Note the generally radial direction of the field.	114
Figure 5.8: Plot of mass flux versus temperature and shell configuration.....	118
Figure 5.9: Cross section of oxide (green) coated aluminum core (blue) showing surrounding oxygen (red) atoms. Higher rates of diffusion for aluminum cations is observed by aluminum atoms moving radially outward into the oxide shell atoms while adsorbed oxygen atoms remain on the outer surface or desorb from the shell. Figures a and b are at 600K and represent 10ps and 100ps of simulation time, respectively. Figures c and d are at 1000K, after 10ps and 100ps, respectively.	121
Figure 6.1: Cross sections of some of the oxide coated aluminum nanoparticle models used in this work. a) 1nm thick, dense oxide shell. b) 1nm thick, crystalline oxide shell. c) 2nm thick, amorphous oxide shell. d) 2nm thick, dense oxide shell with 2:2.7 Al:O ratio. Blue spheres represent oxygen atoms and yellow spheres denote aluminum atoms.....	126
Figure 6.2: Configuration of atoms for larger (8.2nm, left) and (21.0nm, right) nanoparticle cores. Yellow denotes aluminum atoms and oxygen atoms are blue...	126
Figure 6.3: Plot showing diffusion of aluminum cations (blue) through the oxide shell (yellow) as the temperature increases from 300K to 1000K and held for 100 ps. ...	128

Figure 6.4: Time elapsed simulation results of laser heating experiments with the 2nm thick crystalline shell at 440K and the 5.6nm core heated from 440K to 3000K..... 130

Figure 6.5: Ratio of effective radial diffusivity to the overall effective diffusivity. 132

Figure 6.6: In (a) we have plotted the diffusion coefficient for aluminum cations versus $1000 \cdot T^{-1}$ and in (b) the computed mass flux of aluminum cations through the core/shell interface is plotted versus temperature. This data is from the 5.6nm core model system and averaged over all shell configurations for a specific thickness... 133

Figure 6.7: Radial pressure distribution for 5.6nm diameter aluminum core at 600K and at 1000K with 2nm thick dense oxide shell and a non-stoichiometric ratio of aluminum to oxygen. 135

Figure 6.8: Radial pressure distribution for 8.2nm diameter aluminum core at 1000K with a 2nm crystalline oxide shell. 137

Figure 6.9: Plot of an 8.2nm aluminum core with a oxide shell at 1000K after 100ps (a), and the same nanoparticle heated using a laser resulting in a 1000K core and a 440K oxide shell after 100ps (b)..... 139

Figure 6.10: Pressure profile averaged over 8ps at 1000K for ambient heating and laser heating of 5.6nm core with 2nm crystalline oxide shell..... 140

Figure 6.11: Pressure profile averaged over 8ps at 1000K for ambient heating and laser heating of 8.2nm core with 2nm crystalline oxide shell..... 141

Figure 6.12: Cross section of 8.2nm core and oxide shell heated to 1000K by laser heating. Pressure units are MPa. 142

Figure 6.13: Plot of radial pressure for aluminum core sizes of 5.6nm, 8.2nm, and 21nm with 2nm crystalline aluminum oxide shells. 143

1 Introduction

1.1 Nanoparticles

Nanoparticles are defined as small clusters of material, typically less than 100nm in diameter. For centuries they have been used to give paint or pottery glazes a luster. In addition to their interesting optical properties nanoparticles offer many potentially interesting mechanical and chemical properties that differ from the bulk material. These properties arise because of the high surface area to volume ratio inherent at the nanometer scale. Some of the typical modern applications for nanoparticles include catalysis, biosensors, and use as drug delivery vehicles.^{1,2} Nanoparticles can also act as a bridge between the continuum and atomistic length scales because they contain a relatively small number of atoms. Nanoparticles may exhibit quantum confinement, surface Plasmon resonance, and superparamagnetism because of their small size. Understanding and utilizing these properties requires accurate experimental and computer simulation methods, the latter of which is explored here.

Some experimental observations of nanoparticles are very difficult because of the short length and time scales involved. In order to quantify the properties of individual nanoparticles computer simulation can be used in conjunction with experimentation to obtain reliable data and conclusions. For instance, from experimentation we know that oxide coated aluminum nanoparticles react near the melting point of the aluminum core, whereas micron sized particles react at higher temperatures. This reaction process is very rapid, less than 1 ms, making direct measurements difficult. This leaves researchers to consider the processes that are occurring at the nanometer length scale. By using computer simulation it is possible to draw some conclusions

and to help design future experiments that will investigate these findings. Computer simulations are also a powerful predictive tool that can be used to configure future experiments.

1.1.1 Metal Nanoparticles

Metal nanoparticles are of great interest for many applications. Gold nanoparticles may be used for drug delivery, bio-sensors, or as bio-markers because of their inert properties. Silver nanoparticles, on the other hand, are toxic and can be used to kill bacteria, control the replication of viruses, and kill fungi. Other metals such as aluminum have a high enthalpy of combustion and have been used as additives in propellants and explosives to enhance the energy release. These are just a few examples of the useful applications for metal nanoparticles that provide the motivation for this simulation effort.

1.2 Self-Assembled Monolayers

Self-assembled monolayers are single layers of molecules deposited on a substrate. They can be used to coat the surface of a material to make it hydrophobic (repel water) or hydrophilic (attract water), for passivation, or to prepare the surface for later adsorption of a second material such as attaching a drug molecule to the end of a thiol on gold nanoparticles. One point of interest is the effect that the adsorbed monolayers have on the underlying substrate. This is particularly important for nanoparticles where the surface contains a large percentage of the overall material in the substrate, and is the determining factor for the properties of the nanoparticle itself. Computer simulation of this material system should be able to provide some qualitative

and possibly quantitative results to this question of how the monolayer affects the nanoparticle surface.

1.3 Self-Propagating High-Temperature Synthesis (SHS)

SHS is a self-sustaining reaction which is a combustion process that utilizes internal chemical energy to proceed. Numerous advantages of the SHS process include relatively low energy requirements, high purity of products, and the possible formation of complex and metastable phases. There are many materials that can be formed using the SHS process including nickel aluminide (Ni_xAl_y), copper silicide (Cu_3Si), Ti_5Si_3 , NiSi , etc. The SHS formation of nickel aluminide is of great interest because of the desirable properties of the resulting alloy, specifically its high temperature strength and resistance to oxidation. For this reason and a relative wealth of published experimental data nickel aluminide is a good candidate for a further computer simulation investigation. Furthermore, nanoparticles contain excess energy in the form of surface energy that may be harnessed during the SHS reaction of nanoparticle systems and provide a possible enhancement to the sintering of nickel and aluminum nanoparticles.

1.4 Combustion of Oxide-Coated Nanoparticles

The high enthalpy of combustion from the oxidation of metal nanoparticles has prompted the addition of metal nanoparticles into propellants and explosives. It is also because of this high enthalpy of combustion that these materials also form an oxide layer during manufacture or once exposed to the atmosphere. It is therefore important to understand not only the combustive reaction of the bare nanoparticle but

also how the oxide layer affects further oxidation. MD simulation is a good method to investigate this process as it is possible to generate various oxide shell configurations and thicknesses, apply specific heating rates, and to adjust parameters at runtime to compute system sensitivities.

One material with widespread use as an energetic material is aluminum which has been extensively analyzed and modeled. Many numerical models have been developed in an attempt to understand the combustion of aluminum particles. The primary disadvantage of these models is that they may work for micron sized particles where the mean free path is much shorter than the size of the particles, but this is not the case for nanoparticles, which by definition are less than 100nm in diameter. For the burning of aluminum nanoparticles it is not possible to make continuum assumptions. Even with these complexities aluminum nanoparticles are interesting because they have been found to enhance the burning of propellants by a factor of 5 to 10 over micron size particles.

1.5 Organization of this Dissertation

In chapter 2 I give a brief overview of the molecular dynamics algorithm, software, and the empirical potentials used in this work. The software section also includes a subsection on parallel computations and methods. Chapter 3 is a final report on my investigation of alkanethiolate self-assembled monolayer coated gold nanoparticles. Chapter 4 details the results of my simulation and modeling of the sintering and SHS reaction for nickel and aluminum nanoparticles. This chapter includes simulations and comparisons with thermodynamic and phenomenological models. Chapter 5 details the results for the simulation of oxide coated aluminum nanoparticles and

the diffusion mechanism observed for the aluminum atoms in the core. Chapter 6 also investigates the oxide coated aluminum nanoparticle system but compares the MD simulation results with the various analyses available in the literature which predict a different mechanism of initiating the oxidation process. Chapter 7 includes some conclusions and future work.

2 Simulation Details

2.1 Molecular Dynamics

Molecular Dynamics (MD) simulations are used in this work to compute the equilibrium and transport properties of classical many-body systems.³ The MD algorithm defines atoms or molecules to be treated as particles that obey the laws of classical mechanics. With this treatment the particle positions are calculated using Newton's equations of motion. The Verlet algorithm is used to integrate these equations of motion and to calculate the positions of the simulated particles at all times using equation 2.1.

$$\vec{x}(t + \Delta t) = 2\vec{x}(t) - \vec{x}(t - \Delta t) + \frac{\vec{f}(t)}{m} \Delta t^2 \quad 2.1$$

In equation 2.1, \vec{x} is the position of a particle, \vec{f} is the force acting on the particle computed from interaction potentials with other particles, m is the particle mass, and $t + \Delta t$ is the time at which the particle positions are computed. A particle in the simulations performed in this work can be either a single atom as in the case of the gold atoms in a nanoparticle or a more coarse grained definition can be used to define a particle as a single molecule, such as the CH₂ monomers that make up an alkanethiolate SAM chain. For more details on the MD algorithm including the Verlet algorithm, the reader is referred to Frenkel and Smit,³ Allen and Tildesley,⁴ or Haile.⁵

2.2 Software

2.2.1 Parallel Processing

The simulation of large numbers of particles requires the use of parallel processing techniques.⁶⁻⁸ Parallel processing is typically achieved on one of two types of computer architectures; shared-address-space or message-passing. Shared-address-space architectures typically use multithreading to achieve parallelism such as the Silicon Graphics (SGI) Origin 3900 system or other symmetric multiprocessing (SMP) machines. These systems have a single shared pool of memory that any processor or thread can access for read and write operations. The second method, namely message passing, is preferred on distributed memory architectures such as clusters of personal computers (PCs) or on distributed/shared memory architectures that use a hybrid between distributed and shared memory, examples of which are clusters of SMP PCs or the IBM SP3 system.

With high accessibility and attractive performance to price ratios, clusters of PCs are currently the de facto standard for high performance computing. The PC cluster that I started this work on was the 25th ranked fastest supercomputer in the world in June 2006, the John Von Neumann LNX Cluster, Xeon 3.6 GHz, at the U. S. Army Research Laboratory (ARL) on the Aberdeen Proving Ground, MD. With this computer architecture in mind I have focused on using message passing and specifically the MPI (Message Passing Interface) library for MD software development. In 2007 I began using the MJM cluster at ARL which contains 4400 3.0 GHz Intel Woodcrest cores. This machine was primarily used during the Ni/Al sintering simulations and the start of the aluminum oxide effort. As of April of 2009 I am heavily using the

newest Cray XT5 system which contains 12,736 2.3 GHz AMD Opteron cores for simulation of the Al/Al₂O₃ material system with the ReaxFF potential.

2.2.2 Applications and Code Development

In order to prevent the development of yet another MD simulator I have taken advantage of the open source software package LAMMPS (Large-scale Atomic/Molecular Massively Parallel Simulator)⁹ from Steve Plimpton at Sandia National Laboratories (SNL). Using an open source project as a base allows me to focus on developing new inter-atomic potentials, property computations, and performance enhancements rather than spending large amounts of time developing and expanding a code-base that would most likely be abandoned when this research is completed. Supporting the source code for a complex software application requires time and money that can be used elsewhere. When open source applications exist that are used and maintained by many individuals they can stay current and don't require large resources from any single individual for maintenance and upgrades.

The LAMMPS source code is freely available and is written using object oriented (OO) practices with C++. By using OO methods LAMMPS can be easily extended to include new atomic potentials, property calculations, data output, etc. For instance, when simulating the interactions of alkanethiolate chains attached to a gold surface one empirical potential often used is the 12-3 potential that has a form very similar to the Lennard-Jones 12-6 potential. Since the LAMMPS source code is available it is simply a matter of using the included Lennard-Jones potential source code as a template to generate the 12-3 interaction. As part of this effort I have extended LAMMPS to include both the 12-3 interaction potential and the 6-term dihedral po-

tential required for the alkanethiol chains, and formatted embedded atom method potentials for gold and nickel/aluminum interactions for evaluation.

New analysis commands were also added to LAMMPS including radial pressure and density computations. I have also written post-processing routines to convert the LAMMPS dump files into the XDMF (eXtensible Modeling Data Format)¹⁰ for visualization with ParaView¹¹ or within ICE (Interdisciplinary Computing Environment).¹⁰ Some other post-processing routines include one that reads in a LAMMPS dump file and computes the time-averaged pair correlation function, another computes the pressure inside voxels, and electric fields at each atom are also computed as a post-processing routine.

In the final effort in this work to investigate the rapid heating of oxide coated aluminum nanoparticles a much more complex inter-atomic potential was required, namely the reactive force field or ReaxFF. The ReaxFF potential from Caltech was not immediately available in the LAMMPS codebase so another open source parallel MD simulator from SNL was used called GRASP (General Reactive Atomistic Simulation Program). As an update I would like to note that ReaxFF is currently available as an interaction potential within LAMMPS and so GRASP is no longer supported or required.

There are many optimizations that I have considered individually and with collaborators in order to increase the throughput of simulations on Linux clusters. These optimizations include compiler options, choice of math libraries, model cache optimizations such as using the reverse Cuthill-McKee method (RCM),¹² unique hardware utilization, and code rewriting. Each of these performance enhancements may only

increase performance by 10% or so, but combined they can dramatically decrease the time required for each simulation. For example, an MD simulation of a SAM-coated nanoparticle with 4093 Au atoms, and 529 alkanethiol chains with 10 particles each, will require approximately 30 hours of run time on 16 processor cores, with example specifications of a 3.6 GHz Intel Xeon EM64T, for 2 million timesteps, or 0.5 ns of simulated time. With a 20% increase in performance this time can be cut to 24 hours and a parametric study can be performed much more efficiently by providing results each day at the same time.

2.3 Empirical Potentials

The most computationally complex and time consuming portion of an MD simulation is the calculation of the non-bonded interactions using empirical potentials. The choice of the empirical potential is dependent upon the bonding present in the system of interest such as covalent, ionic, or metallic bonding. The potential parameter set chosen for a particular material system will affect the accuracy of the simulation results under specific conditions such as temperature and depending upon the range of fitted data such as vaporization, binding energy, etc. The following sections describe some of the empirical potentials used throughout this work.

2.3.1 Alkanethiolate Coated Gold Nanoparticle

In the alkanethiolate coated gold nanoparticle system there has been extensive effort expended in determining the method that should be used to model the metal substrate. When explicitly considering the metal substrate, the embedded-atom method (EAM)¹³⁻¹⁵ and the effective medium (EM)¹⁶⁻¹⁸ potentials have received the most at-

tention and provide the most accurate results in molecular dynamics (MD) simulations under many conditions. These methods use empirical embedding functions that originate from density functional theory (DFT) and have been successfully used to model many of the physical properties of metals. Since the embedding functions are empirical, they are computationally efficient and yet still accurate enough for many purposes. This efficiency makes it possible for large numbers of atoms to be modeled and thereby making it feasible for the analysis of realistically sized systems to be performed. Of these embedding methods, the EAM appears to currently be the most widely used to model FCC (face centered cubic) lattice metals such as Au, Ag, Cu, etc. many of which are commonly used in the manufacture of nanoparticles.

The EAM was developed as a means of calculating ground-state properties of metal systems.¹³ The embedding functions for various metals are determined by empirically fitting sublimation energy, equilibrium lattice constants, elastic constants, and various other property data points of pure metals. For binary alloys the heats of solution are also used.¹⁴ In the EAM the total energy of an atom is a combination of the embedding energy and pair potential terms as shown in equation 2.2.

$$E_{tot} = \sum_i F_i(\rho_{h,i}) + \frac{1}{2} \sum_i \sum_{j(\neq i)} \phi_{ij}(R_{ij}) \quad 2.2$$

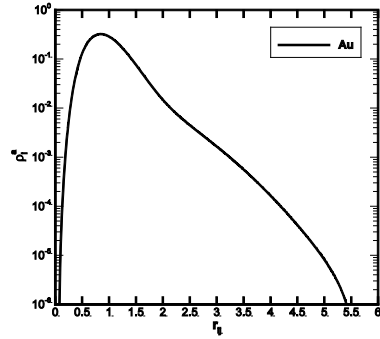
In equation 2.2, $\rho_{h,i}$ is the host electron density at atom i due to the neighboring atoms in the system. $F_i(\rho_{h,i})$ is the energy to embed atom i into the background electron density $\rho_{h,i}$, and $\phi_{ij}(R_{ij})$ is the core-core pair repulsion between atoms i and j separated by the distance R_{ij} . The electron density is approximated by the superposition of atomic densities,

$$\rho_{h,i} = \sum_{j(\neq i)} \rho_j^a(R_{ij}) \quad 2.3$$

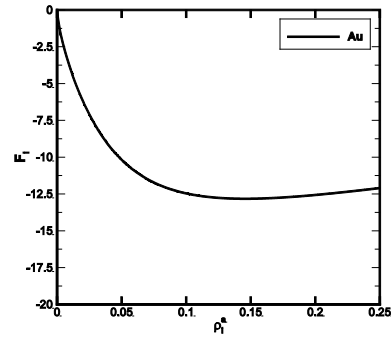
where $\rho_j^a(R_{ij})$ is the electron density contributed by atom j .¹⁴ The pair interaction term, $\phi_{ij}(R_{ij})$, is purely repulsive, and is determined by equation 2.4.

$$\phi_{AB}(R) = Z_A(R)Z_B(R)/R \quad 2.4$$

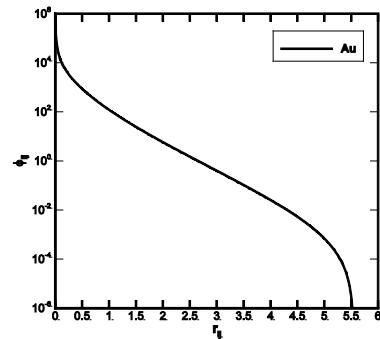
In equation 2.4, $Z_A(R)$ is the effective charge for atom type A, and similarly $Z_B(R)$ is the effective charge for atom type B¹³ with both charges being constrained to be positive.¹⁴



a) Electron Density



b) Embedding Energy



c) Pair Potential

Figure 2.1: Example metal potentials from LAMMPS.⁹ Distances are measured in Angstroms (\AA) and energy is given in electron volts (eV).

A graphical representation of the EAM data used in LAMMPS for various metals is given in Figure 2.1. For more details on the EAM potential the reader is referred to Daw and Baskes¹³ and Foiles et al.¹⁴

In many instances the analysis of an infinite flat surface, as analyzed in the literature for SAM coated gold surfaces, does not require explicit modeling of the metal substrate. Instead the surface can be modeled as a potential surface with a two dimensional energy profile. This is the case in many MEMS devices and so, thus far, most research has not considered the substrate as consisting of movable atoms, but rather as a fixed lattice.¹⁹ This simplification has a secondary benefit because not only is the overall computational complexity lowered but the mixing of potentials for the metal substrate and SAM head group is not required. In contrast, when considering nanoparticles the symmetry boundary conditions that restrict lateral movement are not present. By allowing boundary atoms to move, the surface of a nanoparticle is softer and atoms move more freely. For this reason, the model that I will use here must explicitly consider the metal substrate atoms as dynamic particles. This is in contrast to the model developed by Luedtke and Landman, who do not consider the atoms in their nanocrystallite model as dynamic particles.^{20,21}

Binding of the Head Group to the Metal Substrate

The binding of the head sulfur atom of an alkanethiol chain to the gold substrate is of great interest as it affects the location, orientation, movement, and desorption of chains from the substrate.²²⁻²⁴ Much effort has been devoted to finding accurate potentials for this issue. The level of detail required to determine the potential parameters for use in MD simulations is only satisfied by ab initio calculations such

as DFT.^{22,24} The most published potentials resulting from these calculations are the 12-3 potential,²⁵ equation 2.5, used most commonly in Monte Carlo (MC) simulations of alkanethiolates on gold^{26,27} and the Morse potential, equation 2.6, used in many of the MD simulation studies,^{19,23,27,28} and the Lennard-Jones potential given in equation 2.7. A graphical comparison of these potentials is given in Figure 2.2.

$$U_{Au-S} = \frac{C_{12}}{(z - z_0)^{12}} - \frac{C_3}{(z - z_0)^3} \quad 2.5$$

$$U_{Au-S} = D_e \left[e^{-2\alpha(r-r_0)} - 2e^{-\alpha(r-r_0)} \right] \quad 2.6$$

$$U_{Au-S} = 4\epsilon \left[\left(\frac{\sigma}{r} \right)^6 - \left(\frac{\sigma}{r} \right)^{12} \right] \quad 2.7$$

In addition to the issue of which potential best describes the binding between SAM head-group and substrate, SAM mobility must also be considered.²⁴ The choice of potential was made by evaluating the original purpose for each published data set. For instance, in Shevade et al²⁶ the authors use configurational-bias Monte Carlo simulations to study preferential adsorption and phase separation of alkanethiolate chains on gold surfaces. In this work we chose to use the empirical potential of Zhang et al¹⁹ where an accurate Morse potential is developed for the binding of alkanethiolate chains to gold surfaces using accurate *ab initio* quantum chemical calculations.

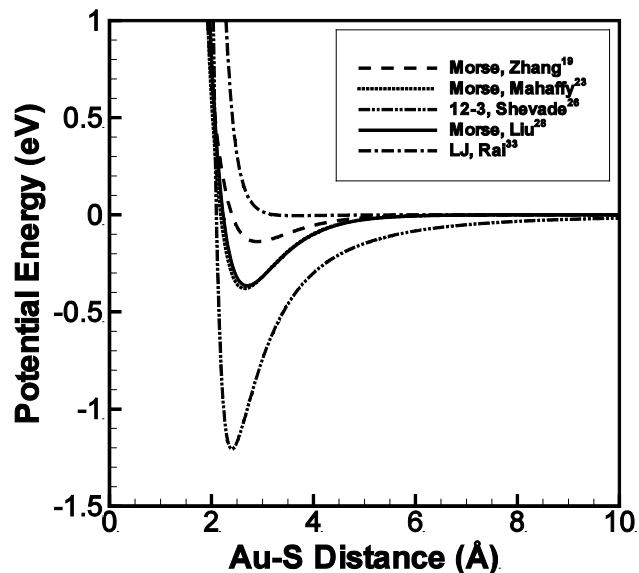


Figure 2.2: Published potential energy functions for Au-S binding. All units are in Angstroms (Å) or electron volts (eV).

Published results for this material system include the orientation of the alkanethiol chains to the gold surface, the surface area per alkanethiolate chain, and the arrangement of chains on the surface. Experimental data includes the binding energy of the chain to the gold surface with a documented value of 1.9 eV.²⁹⁻³¹ The surface area occupied by a single alkanethiolate chain is also established to be between 21.4 Å²³² and 21.6 Å²^{33,34} for flat 2-dimensional surfaces. For 3-dimensional surfaces such as nanocrystallites Landman and Luedtke have computed the surface coverage to be 15.4 Å² per chain.^{20,21}

The parameters used to compute the potential curves in Figure 2.2 are given in table 2.1. In this work I have chosen to use the parameter set from Zhang et al¹⁹ because of the previous analyses performed with this data which include chain mobility. In later sections I provide some information on how the strength of the Au-S bond affects the simulation results.

Table 2.1. Computed corrugation factors for alkanethiolate SAM coated gold nanoparticles.

Reference	Pot.	C_{12} (eV/Å ¹²)	C_3 (eV/Å ³)	z_0 (Å)	D_e (eV)	a	r_0 (Å)	σ (Å)	ϵ (eV)
Shevade ²⁶	12-3	3523.52	15.56	0.269					
Zhang ¹⁹	Morse				0.138	1.38	2.90		
Liu ²⁸	Morse				0.365	1.47	2.70		
Mahaffy ²³	Morse				0.380	1.47	2.65		
Rai ³³	LJ							3.639	0.00107

Modeling of the Alkenthiolate Chain

The polymer chain that makes up the SAM may be modeled with varying levels of detail. From the high accuracy/high computational requirements of the all-atom model to less accurate/lower computational requirement methods such as the united atom or the coarse grained bond models. In order to illustrate these methods we can consider the CH₂ molecule that makes up the backbone of the alkanethiol chain. When using the all-atom model the numerical simulation must consider the three atoms that make up the molecule as individual particles. Using the united atom model only a single pseudo atom is simulated in place of the CH₂ molecule,³⁵ and with the coarse graining techniques multiple, up to five or more, CH₂ molecules are grouped together into a single simulation particle.³⁶⁻³⁸ Which model is used for a particular simulation depends greatly upon the level of detail required in the results of interest and the physical properties of the polymer chain.

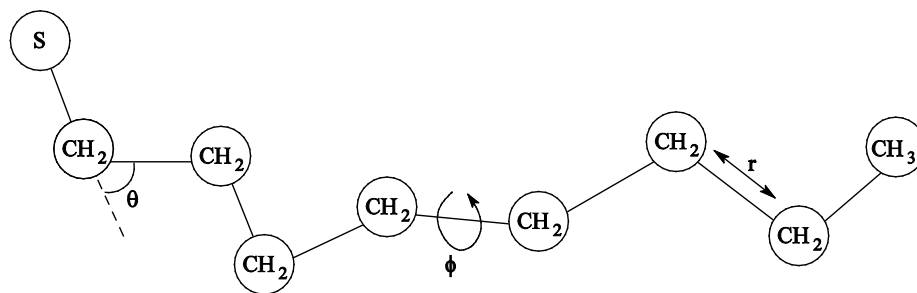


Figure 2.3: Sample alkanethiolate chain with 8 carbon atoms along the backbone.

The modeling of the alkanethiol chain using the united atom model is consistent with much of the available literature concerning alkanethiolate coated gold nanoparticles. The potentials used in the united atom model include a bending potential for the S-C-C bond and the C-C-C bond. The bending potential has either a form similar to equation 2.8 or the angle can be held fixed, thus lowering the degrees of freedom that need to be modeled. The second bond interaction is the dihedral potential between 4 bonded particles. For X-C-C-X bonds, where X can be either S or C, the potential takes the form of equation 2.9. The most apparent differences in the literature occur in the method used to model the bond lengths along the chain. The bond lengths along the chain can be held constant²⁶ with the RATTLE³⁹ algorithm or they can be modeled as harmonic bonds^{33,38} as given in equation 2.10. Both of which are frequently used. Using a harmonic potential to describe the C-C and S-C backbone bonds allows the distance between the backbone atoms to change while not allowing the bonds to break.

$$U_{bending}(\theta) = \frac{1}{2}k_{\theta}(\theta - \theta_0)^2 \quad 2.8$$

$$U_{dihedral}(\phi) = a_0 + a_1 \cos(\phi) + a_2 \cos^2(\phi) + a_3 \cos^3(\phi) + a_4 \cos^4(\phi) + a_5 \cos^5(\phi) \quad 2.9$$

$$U_{bond}(r) = \frac{1}{2} k_r (r - r_0)^2 \quad 2.10$$

By combining each of these empirical potentials for all of the inter- and intra-atomic interactions it is possible to accurately describe the alkanethiolate coated gold nanoparticle material system under various conditions.

2.3.2 The Energetic Sintering Reaction of Nickel and Aluminum

In the alkanethiolate coated gold nanoparticle simulation effort the EAM potential was used to model a monatomic material, namely gold. In this section I will discuss the use of the EAM potential as it has been extended for alloys to include heterogeneous interaction data. The particular EAM potential used in this work to describe the metal atom interactions between heterogeneous metals is the Finnis-Sinclair (FS) EAM. The FS EAM potential parameter set used to simulate aluminum and nickel interactions is from Angelo et al.⁴⁰ and is shown in figure 2.4.

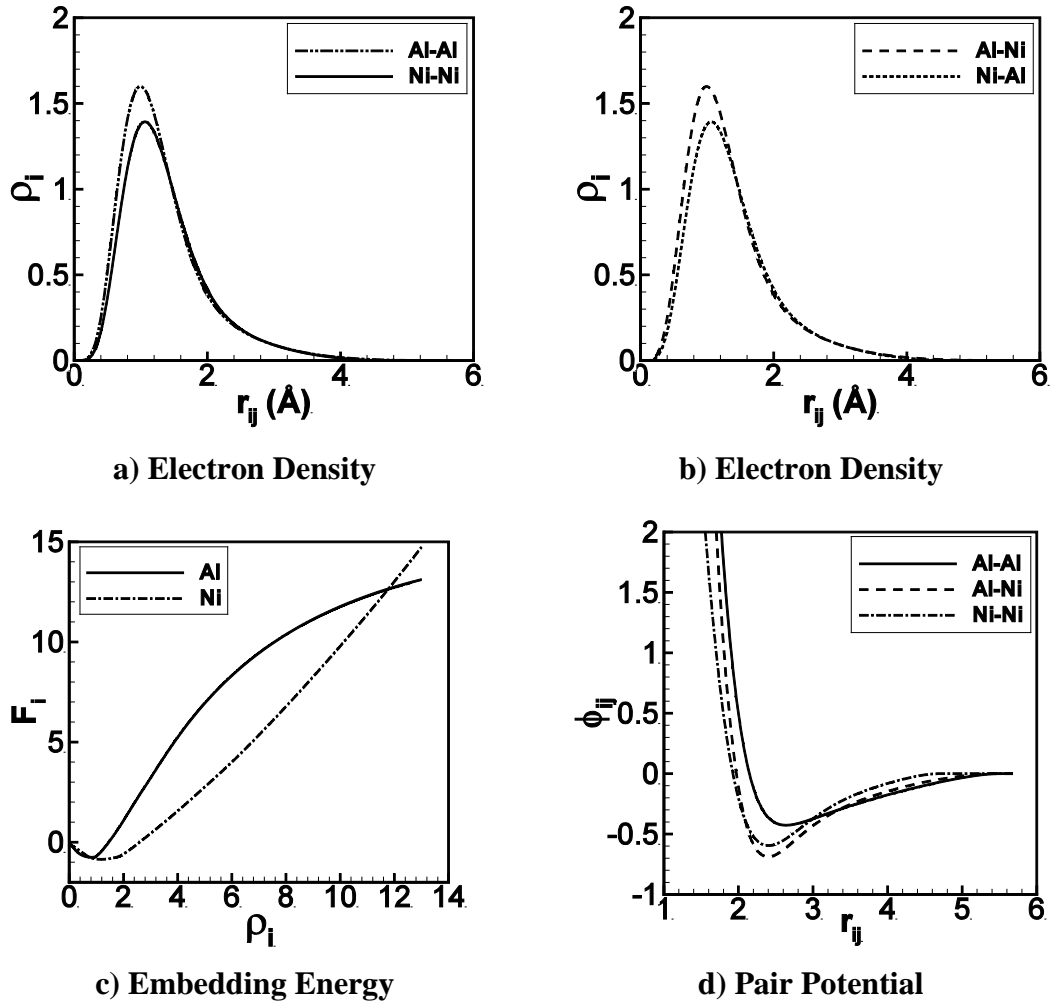


Figure 2.4: Finnis-Sinclair EAM potential data for the nickel/aluminum system. Distances are measured in Angstroms (\AA) and energy is given in electron volts (eV).

In Figure 2.4 the electron density contribution, ρ , to an aluminum atom from another aluminum atom is the same as that from a nickel atom. The reciprocal is true for nickel atoms neighbored by nickel and aluminum atoms. This is not required by the FS EAM potential and so the potential data used here is not as general as it could be, but it does take advantage of one of the benefits of the FS EAM potential. Specifically, in Figure 2.4d the pair energy of the Al-Ni bond is lower than either the Al-Al or Ni-Ni bonds. This is indicative of the high enthalpy of formation observed in the

Ni-Al material system. A second dataset from Mishin et al.⁴¹ was also considered for this investigation, although it was not used extensively here because of the over predicted melting temperature of aluminum.

2.3.3 Oxidation of Oxide Coated Aluminum Nanoparticle

The primary difference between the previous research efforts and this material system is that in order to accurately simulate the oxidation of aluminum requires the consideration of the charge transfer that occurs between aluminum and oxygen atoms. This has numerical complexities beyond a simple multibody interaction as that found in the FS EAM method. I considered two empirical potentials in order to simulate this material system. They are the Streitz-Mintmire potential and the reactive force field (ReaxFF). I chose the ReaxFF potential partly because it is implemented inside of the GRASP MD code developed by Aidan P. Thompson and now available in LAMMPS, both from SNL. ReaxFF has been demonstrated to accurately simulate the material system of interest, namely aluminum oxide.⁴² GRASP, like LAMMPS, is a parallel MD application capable of scaling to large numbers of processors on distributed memory architectures providing the capabilities required to simulate nanoparticles large enough that simulation results can be compared directly with experimental and analytic results.

The ReaxFF potential contains many more terms and is much more computationally complex than any of the previously discussed potentials. As an illustration all of the energy terms that may be provided for a material system are given in equation 2.11.

$$E_{system} = E_{bond} + E_{over} + E_{under} + E_{lp} + E_{val} + E_{pen} + E_{tors} + E_{conj} + E_{vdWaals} + E_{Coulomb} \quad 2.11$$

The terms in equation 2.11 are bond energies (E_{bond}), under-coordination penalty energies (E_{under}), lone-pairs energies (E_{lp}), over-coordination penalty energies (E_{over}), valence angles energies (E_{val}), energy penalty for handling atoms with two double bonds (E_{pen}), torsion angles energies (E_{tors}), conjugated bonds energies (E_{conj}) and terms to handle non-bonded interactions, namely van der Waals ($E_{vdWaals}$) and Coulomb ($E_{Coulomb}$) interactions. The potential terms required for the aluminum oxide material system are $E_{Coulomb}$, E_{bond} , E_{over} , and $E_{vdWaals}$.

2.3.4 Computation of System Properties

Computation of system properties is done using two methods in this work, namely as pre- or post-processing. Many system properties can be computed as a post-processing step, these include the pair correlation function, compound formation and distribution, diffusion coefficients, and electric fields, among others. These post-processing calculations require that specific data such as atomic positions, velocities, and charges are stored periodically. Other computed properties such as the radial pressure distribution must be computed at run time in order to limit the amount of information written to disk. This is because for the radial pressure distribution every atomic interaction must be considered and would therefore require storing data one or two orders of magnitude larger than for the typical post-processing calculations.

With this in mind, I have listed below most of the properties computed in this work and a brief description of the calculation involved. Further detail is usually found in the references provided.

2.3.5 Pair Correlation Function

The pair correlation function is also known as the pair distribution function or radial distribution function. It is computed using equation 2.12.

$$g(r) = \frac{V}{N^2} \left\langle \sum_i \sum_{i \neq j} \delta(\vec{r} - \vec{r}_{ij}) \right\rangle \quad 2.12$$

In equation 2.12 V is the system volume, N is the number of atoms in the system, and r are the atomic positions. The pair correlation function gives insight into the structure and phase of the material, indicating whether it is in a solid or liquid state and at what temperature that change occurs. This function can also be used to compute the ensemble average of any pair function.⁴ In this work the pair correlation function is used as an indicator of the change in morphology of metal nanoparticles that occurs because of coatings and temperature changes. Details on usage and implementation can be found in Frenkel and Smit.³

2.3.6 Radial Pressure Distribution

The radial pressure distribution is computed using two methods in this work. The first of which uses the Irving-Kirkwood (IK) pressure tensor,⁴³ and second uses the virial stress^{44,45} at each atom. The particular method used depends upon whether the interactions can be broken down into simple pair interactions (IK) or if the potential is more complex such as the ReaxFF potential in which case the virial formulation is used.

The Irving-Kirkwood Pressure Tensor

Computing the IK pressure tensor requires the computation of two terms, namely the kinetic and the configurational terms as shown in equation 2.13.

$$P_N(r) = P_K(r) + P_U(r) \quad 2.13$$

In equation 2.13 P_K represents the kinetic pressure term and P_U is the configurational pressure term. The kinetic pressure term is a function of temperature and the radial density distribution as given in equation 2.14.

$$P_K(r) = k_B T \rho(r) \quad 2.14$$

The configurational term is computed from the forces that act between pairs of particles, as defined in equation 2.14, as $du(r_{ij})/dr_{ij}$. Figure 2.5 is an illustration showing the vectors used in computing the configurational pressure term. For each shell of radius r sharing a center with the nanoparticle center, the forces between particles whose connecting line intersects the shell must be considered. Figure 2.5 shows two particles, i and j , which interact along a vector that intersects a shell of radius $|\vec{r}_A|$ twice. This pair interaction is included in the configurational term for the shell of radius, $|\vec{r}_A|$. Particles whose interaction vector \vec{r}_{ij} only crosses the shell once, i.e. one particle inside and one particle outside are also considered, but with only half of the magnitude of the previous case where both particles were outside of the shell.

$$P_U(r) = -(4\pi r^3) \sum_k |\vec{r} \cdot \vec{r}_{ij}| \frac{1}{r_{ij}} \frac{du(r_{ij})}{dr_{ij}} \quad 2.15$$

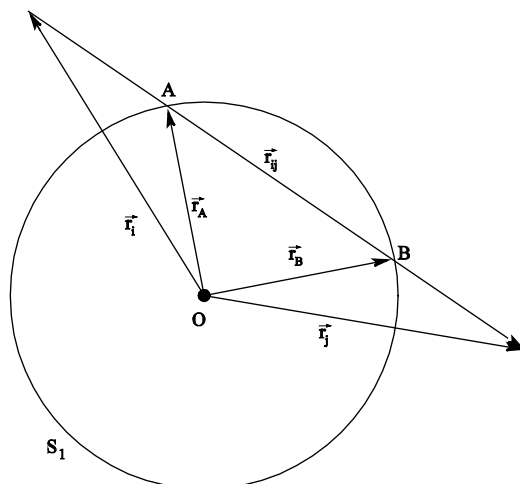


Figure 2.5: Circle used in computing radial pressure using the Irving-Kirkwood tensor.

The IK pressure tensor is used with the alkanethiolate coated gold nanoparticle material system where all of the forces on an atom can be broken down into pair interactions.

The Virial Pressure

The virial stress^{44,45} is computed on a per atom basis using both kinetic and potential energy contributions. The virial stress computation results in a 6 component stress tensor at each atom. These 6 components can then be used to compute the local pressure by summing the trace (i.e. $\sigma_{xx} + \sigma_{yy} + \sigma_{zz}$) of the tensor. This method of computing the local pressure is less preferable compared to computing the IK pressure tensor because of the difficulty in obtaining accurate results, due in part to issues associated with obtaining an accurate atomic volume for each atom in a deformed body. The virial stress method, however, is able to compute the pressure in a system where the empirical potentials used are multi-body potentials and cannot be broken down in to pair wise interactions as required by the IK pressure calculation. The virial pressure

calculation in used in GRASP for the oxide coated aluminum nanoparticle simulation effort.

2.3.7 Surface Tension

Once the radial pressure distribution has been computed using either the IK or virial methods it is possible to compute the surface tension at the various interfaces in the SAM coated nanoparticle system. These interfaces include the interface of a bare nanoparticle and a vacuum, the interface between the nanoparticle and a SAM, or between two metals. Some experimentally determined surface tension data is available and can be used to validate the MD simulation results. Surface tension in a nanoparticle is also an indication of mechanical stability. For instance, the surface tension of a small droplet is typically positive, indicating a compressive stress throughout the droplet, resulting in the observed spherical shape of a suspended liquid droplet. In a solid nanoparticle, however, it may be possible to support a tensile stress where deformation is resisted and therefore a negative surface tension indicates a metastable state.

The surface tension is computed from the MD simulation results in this work using two methods. The first is the Young-Laplace theorem given in equation 2.16.

$$\Delta P = \frac{2\gamma}{r} \tag{2.16}$$

In equation 2.16 r is the radius of the droplet under consideration, ΔP is the difference in pressure between the interior and exterior of the droplet, and γ is the surface tension at r . γ may be determined either from experimental data and used to predict the

internal pressure of the droplet (nanoparticle) or it may be extracted from MD calculations of the normal pressure at the surface of the nanoparticle.

The second, and potentially more accurate, method used to compute the surface tension is the approach outlined by Rowlinson and Widom.⁴³ This method integrates the pressure results from the interior of the droplet to a point outside the droplet, which in this case is under vacuum. The calculation takes the form of equation 2.17.

$$\gamma_i^3 = -\frac{1}{8}(p_{r_2} - p_{r_1})^2 \int_{r_1}^{r_2} r^3 \frac{dp_N(r)}{dr} dr \quad 2.17$$

In equation 2.17 p_{r_2} and p_{r_1} are the computed pressure at the maximum and minimum model radii, respectively, and $dp_N(r)/dr$ is the gradient of the normal pressure at radius r . For pressure profiles that do not have a clear demarcation of the external interface this method is a better choice for computing the surface tension, as it integrates across the interfacial area. The choice of r_1 and r_2 is somewhat arbitrary but should be chosen sufficiently away from the interfacial region to avoid noise from random variations in the region of the interface.

2.3.8 Heat Capacity

The constant volume heat capacity, C_v , of the system is computed directly from the MD simulation results as the slope of the potential energy versus temperature curve using an NVE (microcanonical canonical) ensemble. A typical simulation used to compute the heat capacity of a material system is initialized by equilibrating at a low temperature, typically room temperature for metal nanoparticles, and slowly heating and equilibrating the system at small temperature increments. This process is continued until a straight line can be drawn and the slope determined with certainty. If

the system is heated further the melting temperature will be reached at which point a discontinuity in the system potential energy is observed indicating that a phase change has occurred. The temperature increases are subsequently continued in order to determine the heat capacity of the liquid phase. It is important to note that in MD simulations of this type it is not uncommon to have difficulty in computing an accurate melting temperature and superheating and supercooling are often observed in the simulation depending upon whether the temperature is being increased or decreased, respectively.

2.3.9 Electric Field

In simulations where the atomic charge is computed the electric field at an atom can be computed. One method to compute this electric field is by using Coulomb's law, equation 2.18, to sum the discrete electric field contributions from all surrounding atoms.

$$E = \frac{q}{4\pi\epsilon_0 r^2} \hat{e}_r \tag{2.18}$$

In equation 2.18 \hat{e}_r is the radial unit vector emanating from a neighboring atom and q is the charge associated with that neighboring atom, ϵ_0 is the permittivity of a vacuum, and r is the distance to the neighboring atom. Since the contribution to the electric field is non-symmetric a complete loop over every atom is required, resulting in an $O(n^2)$ calculation. If the atomic charge is stored along with atomic positions this computation can be performed as a post-processing step. By computing the electric field it is possible to visualize the magnitude and direction of the Coulombic potential acting on an atom.

3 Mechano-Chemical Stability of Gold Nanoparticles Coated with Alkanethiolate SAMs

3.1 Introduction

Molecular dynamics simulations are used to probe the structure and stability of alkanethiolate self-assembled monolayers (SAMs) on gold nanoparticles. We have observed that the surface of gold nanoparticles become highly corrugated by the adsorption of the SAMs. Furthermore, as the temperature is increased, the SAMs dissolve into the gold nanoparticle, creating a liquid mixture at temperatures much lower than the melting temperature of the gold nanoparticle. By analyzing the mechanical and chemical properties of gold nanoparticles at temperatures below the melting point of gold, with different SAM chain lengths and surface coverage properties, we have determined that the system is metastable. The model and computational results that provide support for this hypothesis are presented.

3.2 Background

Nanoparticles are often used in applications where a high surface area to volume ratio is desired. Some of the typical applications include catalysis, biosensors, and use as drug delivery vehicles.^{1,2} A major limitation of the expanded use of these nanoparticles is that the fabrication of nanoparticles with the desired morphology and structure is challenging.⁴⁶⁻⁴⁸ Gold is a commonly used material because of its resistance to oxidation and its interesting electrical, magnetic, optical, and physical properties.²⁰ Furthermore there is a considerable knowledge base on functionalizing gold

surfaces that is being ported to analogous particles.³⁴ For these reasons and because of the availability of experimental^{49,50} and atomistic simulation data^{13, 51} gold nanoparticles are commonly chosen for basic research. For instance, using x-ray powder diffraction Cleveland et al.⁵⁰ discovered that small 10-20Å diameter gold nanoparticles form a truncated-decahedral motif geometry. Using molecular dynamics (MD) simulations Lewis et al.⁵² were able to determine the melting process for gold nanoparticles. This last result is important because the authors found that the surface atoms melt first, and at a temperature below that of the atoms in the core of the nanoparticle. The implications of this for coated nanoparticles is that the surface atoms, where binding of the monolayer takes place, is affected by a lower temperature than is expected from the melting temperature of the entire nanoparticle. The results of these past efforts are built upon in this work in order to analyze the nature and role of surface functionalization.

Coating of gold surfaces and nanoparticles with a self-assembled monolayer (SAM) exposes many additional applications for gold nanoparticles including lithography, lubrication, catalysis, biocompatible materials, and biosensors.^{20,26} There have been numerous experimental^{31,32,53} and numerical^{19,21,26} studies performed that have attempted to characterize the properties of alkanethiolate SAM coated gold surfaces. Simulations investigating alkanethiolate SAM coated gold surfaces accurately predict the c(4x2) superlattice structure of alkanethiols on an Au(111) surface.¹⁹ Additional work has predicted the segregation of SAM chains adsorbed on a gold surface by length,²⁶ surface frictional forces,²⁷ and phase behavior.⁵⁴ Efforts to characterize the alkanethiolate SAM coated gold nanoparticle system have been limited to

atomistic simulations considering a single alkanethiol chain, and a small (less than 100 atom) gold cluster^{19,54} or MD simulations of small nanoparticles that ignore the mobility of gold atoms.^{20,21}

The use of coatings for surface passivation has been found to significantly reduce the degree to which agglomeration and sintering will occur.^{55,56} In addition to surface passivation other affects related to the passivation layer investigated computationally here and elsewhere include changes in the internal pressure and surface tension.⁵⁷

This chapter is focused on understanding the effect of the alkanethiolate SAM on gold nanoparticles using MD simulations. Using the pair correlation function we estimate the melting temperature of the particle, and the affect that the SAM has on the particle surface. We clarify the relationship between surface coverage and structure of the particle by introducing a corrugation factor, and identify the phase transition mechanism of SAM coated gold nanoparticles. We find that the SAM coated particles are mechanically unstable as determined by the radial pressure profile.

3.3 Computational Modeling and Numerical Procedure

ab-initio quantum chemical calculations have been used to simulate gold clusters with short alkanethiolate SAMs, primarily to determine potential parameters for MD or MC computations. The *ab-initio* calculations show that the gold crystal lattice is perturbed by the adsorbed ligand.⁵⁸ The consequence of the perturbation is an increase in Au-Au bond length of up to 20%. The increase in bond length is observed around the adsorption site with relaxation propagating to the second layer. These re-

sults suggest that the MD simulations should include dynamic gold atoms in order to accurately consider the nanoparticle/SAM system.

Alkanethiolate chains adsorbed on a flat surface made of immobile gold atoms are limited to diffusion in only two dimensions, whereas, chains adsorbed onto a nanoparticle surface with mobile gold atoms may diffuse in three dimensions. This disparity in model detail is expected to provide more insight into the SAM coated nanoparticle system, than previously available. The inclusion in the simulation of a surface constructed of dynamic gold atoms should be able to more accurately predict alkanethiol chain movement than the limited movement possible on a flat surface of fixed gold atoms.

The size of the model system investigated here is determined by approximating experimentally realistic systems. The manufacture of consistently sized small diameter nanoparticles becomes more difficult at diameters of less than 50Å, therefore, in this work 50Å diameter gold nanoparticles (4093 gold atoms) with and without SAMs are considered. The SAM considered consists of alkanethiolate chains that contain a sulfur atom head group that binds to the gold surface, and a carbon backbone with 3 to 18 carbon atoms comprising the alkyl chain.

The MD simulations in this work are carried out using the LAMMPS (Large-scale Atomic/Molecular Massively Parallel Simulator)⁹ software

3.3.1 Simulating the Gold Substrate

In this effort the gold substrate atoms are explicitly considered as dynamic atoms, requiring that an accurate potential be used to simulate these atomic interactions. We chose the EAM for modeling the gold substrate because of its reported ac-

curacy, and the potentially important extensions developed for the EAM for modeling surfaces, such as the extended EAM (XEAM),⁶⁰ and the surface EAM (SEAM).⁶¹ The actual EAM potential used in this work is taken from LAMMPS.⁹ Also considered was a second dataset from Voter and Chen.⁶² A detailed discussion of the method as used in this work can be found in Daw et al.^{13,14}

3.3.2 Modeling the Alkanethiolate Chain

The alkanethiolate polymer chain may be simulated with a range of computational complexity depending upon the resources available, and the accuracy of results required. For MD simulations, the three methods available for modeling the alkanethiolate chain are the high-accuracy/high computational requirement all-atom model, the less accurate/lower computational requirement united atom method, and the coarse grained bond model. These methods can be compared by considering their treatment of the CH₂ molecule that makes up the backbone of the alkanethiolate chain. When using the all-atom model, the numerical simulation must consider three particles for each molecule and the interactions between each. Using the united atom model only one particle is simulated for each molecule,³⁵ which eliminates the intermolecular interactions, and limits the number of intramolecular interaction potentials required. Finally, with the coarse grained model, multiple molecules are clustered together into one particle with perhaps five or more CH₂ molecules grouped into one simulated particle.³⁶⁻³⁸ For the simulations in this work we have chosen the united atom method, which is computationally more efficient than the all atom method, yet provides sufficient accuracy for the current analysis.²¹

The modeling of the alkanethiolate chain using the united atom model is consistent with many of the published studies for the alkanethiolate coated gold material system.^{19,20,21,54} An example of the alkanethiolate polymer chain model used in this work is shown in Figure 3.1. The potentials used in the united atom model include a bending potential for the S-C-C bond and the C-C-C bond. Additionally there is a dihedral potential for the X-C-C-X bonds, where X can be either S or C. Using a harmonic bond to describe the C-C and S-C backbone bonds allows the distance between the backbone atoms to change while not allowing the bonds to break during the simulation.

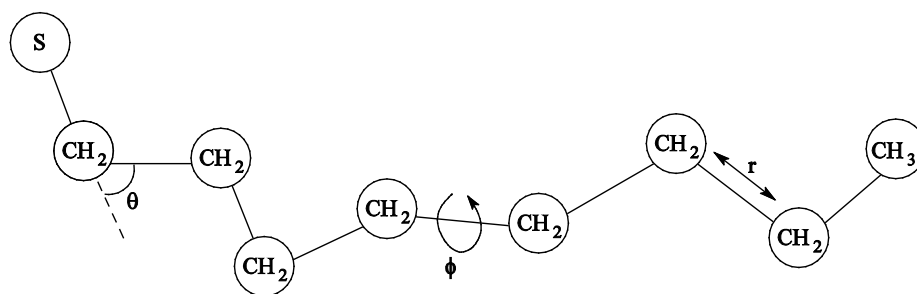


Figure 3.1: Sample alkanethiolate chain with 8 carbon atoms along the backbone.

The potentials and parameter values for the bending angle and dihedral angle from Figure 3.1 and used in this work are given in Shevade et al.,²⁶ the bond stretch parameters are given in Rai et al.³³

3.3.3 Binding of Sulfur to Gold

The binding potential of the head sulfur atom of an alkanethiol chain to the gold substrate is of great interest as it affects the location, orientation, movement, and desorption of chains from the gold surface.^{20,23,24} There has been significant effort devoted to finding accurate potentials for simulating the sulfur to gold binding energy

from *ab-initio* methods.^{20,24} The most commonly published potentials resulting from these calculations are the 12-3 potential,²⁵ used most commonly in Monte Carlo (MC) simulations of alkanethiolates on gold surfaces^{26,27} and the Morse potential, used in many of the MD simulation studies.^{19,23,27,28} In addition to the issue of which potential best describes the binding between SAM headgroup and substrate, the possibility of SAM mobility must also be considered.²⁴ Since the Morse potential, Eq. 3.1, can mimic a partially covalent bond,¹⁹ it is used in MD simulations along with the parameters given by Zhang et al¹⁹ to model the Au-S bond. The parameters for Eq. 3.1 are $D_e = 13.3\text{kJ/mol}$, $\alpha = 1.38$, and $r_0 = 2.903\text{\AA}$.

$$U_{Morse}(r) = D_e \left[e^{-2\alpha(r-r_0)} - 2e^{-\alpha(r-r_0)} \right] \quad 3.1$$

The binding energy of the alkanethiol chain to the gold surface has been determined to be around 184.1 kJ/mol²⁶ when all of the sulfur-gold interactions are considered. Although this reported value is often referenced, there are several studies that report the sulfur-gold bond energy to be closer to 126.0 kJ/mol.^{63,64} This discrepancy in the binding energy is large, and so in this work we will investigate using both binding energies in order to understand the affect that binding energy has on the computed results. For the sulfur-gold binding energy of 126.0 kJ/mol, the Morse potential parameter $D_e = 9.108\text{ kJ/mol}$.

3.4 Simulation Results

In this section, the results from the MD simulations are presented and analyzed. In order to study the effects of the alkanethiolate SAM on the gold nanoparticle we have computed many system properties. These properties include diffusion coefficients, radial pressure and density distributions, melting temperature, and the pair cor-

relation function. A corrugation factor that describes the depth to which the gold surface is modified by the adsorbed alkanethiolate chains is also defined in this section. Each of these results is a data point of the changes the nanoparticle surface experiences with the adsorption of the alkanethiolate SAM. For instance, the diffusion coefficient is used to compute the mobility of the SAM chains that are adsorbed on the surface of the nanoparticle, and the mobility of the gold atoms near the surface of the nanoparticle. The combination of these two coefficients will partially define the phase of the materials near and on the nanoparticle surface and also help in predicting if nucleation of the SAM chains will occur. Nucleation may occur under low surface coverage conditions when the chains form dense groups and uneven surface coverage. The density distribution is used to find the depth to which the sulfur atoms penetrate the surface of the gold nanoparticle and to compute the corrugation factor.

The simulation results will also be compared for the two sulfur-gold binding energies considered in this work. The computed results will be compared and discussed in order to better understand how the head group binding energy affects the properties of the nanoparticle and anticipated trends for these properties. It is expected that the lower binding energy will have less of an effect on the properties of the gold nanoparticle than the high sulfur binding energy. On the other hand some anticipated processes such as desorption will possibly be observed only at the lower binding energy because the temperature required for desorption will be lower.

The simulation is initialized with a sphere of FCC lattice gold atoms at 0 K. By applying a random velocity distribution to the gold atoms the temperature is raised to 10 K and then slowly increased over 10^7 time steps to 1400 K, or above the bulk

melting temperature of gold. By rescaling the velocity the temperature is then decreased to 300 K over $8 \cdot 10^6$ time steps and then held for another $8 \cdot 10^6$ time steps. The temperature rescaling fix is finally removed in order to determine if the total energy of the system remains constant or conserved. The nanoparticle now contains many large facets with (111) and (100) faces, as one would expect from experimental observations.⁶⁵ Next, the alkanethiol chains are randomly distributed around the nanoparticle with the sulfur head group at the equilibrium distance from the gold surface. The alkanethiol chains are initially orientated radially from the nanoparticle center. The alkanethiol chains were initialized with 100% gauche defects. The affect of this initialization on the observed simulation results is negligible as many of the gauche defects are removed during equilibration. The only result that would not be considered accurate is a quantitative measurement of the fraction of gauche defects under various conditions. The number of chains is determined by the requested surface area per chain. The temperature is again initialized to 10 K and slowly heated to 300 K and then held until the total system energy remains constant, indicating that equilibrium has been achieved. The temperature during equilibration of the alkanethiolate coated nanoparticle is not allowed to increase beyond 300 K because desorbtion is expected to occur beyond this temperature.³⁴

3.4.1 Pair Correlation Function

The pair correlation function, $g(r)$, is defined as the number of atoms a distance r from a given atom compared with the number of atoms at the same distance in an ideal gas at the same density.⁴ The pair correlation function for a bare 50Å diameter gold nanoparticle is shown in Figure 3.2 for a range of temperatures.

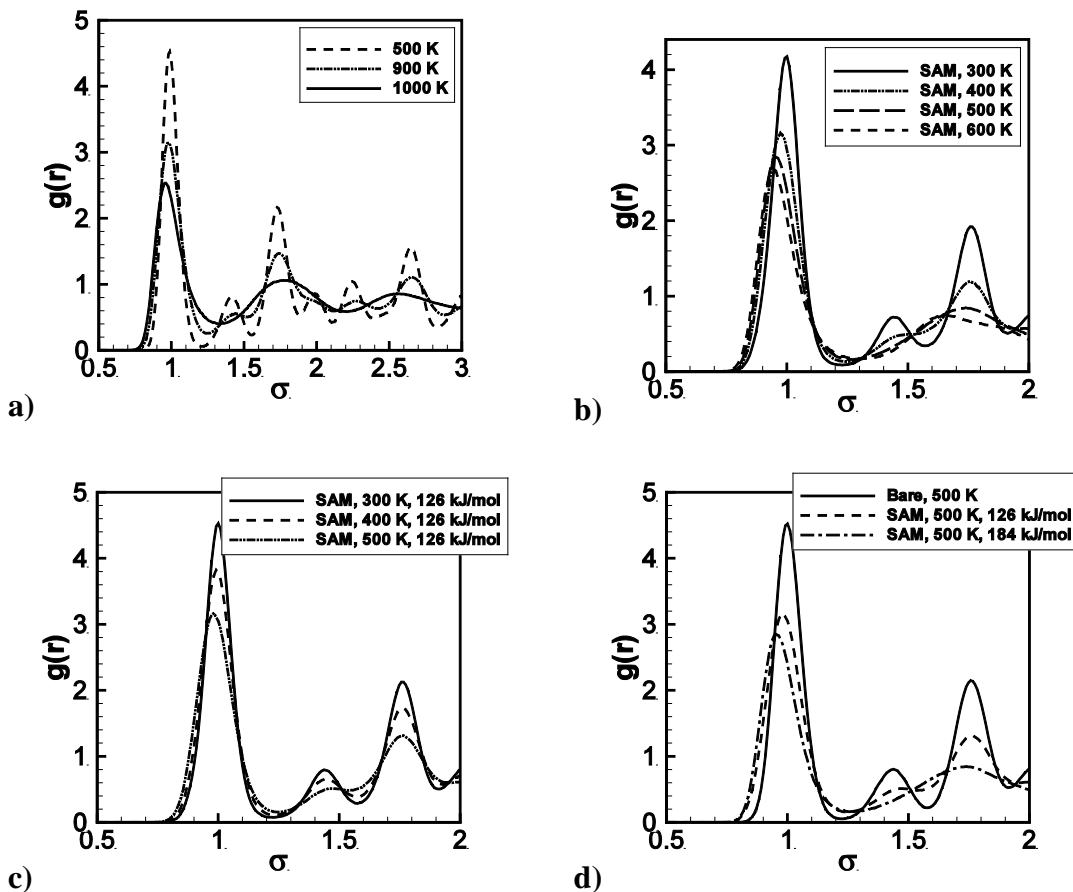


Figure 3.2: In figures a-d the x-axis has been normalized by the nearest neighbor distance for gold, i.e. $\sigma=r/2.88\text{\AA}$. a) Pair correlation function for bare 50\AA gold nanoparticle. Note the change in shape and the location of peaks between 900 K and 1000 K. b) Pair correlation function results for the gold atoms in a 50\AA gold nanoparticle coated with an alkanethiolate SAM at various temperatures with a sulfur binding energy of 184 kJ/mol. c) The pair correlation function results for the SAM coated gold nanoparticle with the lower sulfur binding energy of 126 kJ/mol. d) a comparison of the pair correlation results at 500 K for the bare nanoparticle and high (184 kJ/mol) and low (126 kJ/mol) alkanethiol binding energies.

The results in Figure 3.2a indicate that a phase transition occurs in the nanoparticle from a crystalline solid at 900 K to a liquid at 1000 K, and as expected, this temperature range is below that of the bulk melting temperature of 1340 K.⁵²

For a spherical nanoparticle the melting temperature can be crudely predicted from experimental data using Eq. 3.2, where ρ_S and ρ_L are the specific mass of the solid and liquid phases, respectively. γ_S and γ_L are the surface energies of the solid and liquid phases, respectively, D_p is the particle diameter, L is the heat of fusion, and T_∞ and $T(D_p)$ are the bulk and size dependent melting temperatures, respectively. Using published data for gold⁵² the predicted melting temperature of a 50Å diameter gold nanoparticle is about 995 K. This result is within the range of our MD simulation prediction for the melting temperature.

$$\frac{T(D_p) - T_\infty}{T_\infty} = \frac{4}{\rho_S L D_p} [\gamma_S - \gamma_L (\rho_S / \rho_L)^{2/3}] \quad 3.2$$

Next we compare the pair correlation function results for the uncoated gold nanoparticle to the results for an alkanethiolate coated gold nanoparticle. The coating considered is a complete coating, meaning one chain per 15.4Å² of surface area on the gold nanoparticle,⁶⁶ and is about 30% denser than the packing density on a flat surface (one chain per 21.4Å²).³² The pair correlation function results for the alkanethiolate SAM-coated gold nanoparticle show a nanoparticle with a crystalline structure for temperatures below 400 K, and an amorphous structure above 600 K, see Figure 3.2b. The pair correlation function is computed for the gold atoms only in Figure 3.2b. By only considering the gold atoms in computing the pair correlation function, the structure of the nanoparticle is analyzed separately from the SAM. At 500 K, the structure of the gold nanoparticle has changed to a less ordered structure, similar to that observed during the melting of the uncoated gold nanoparticle. This change in the pair correlation function indicates that a structural change occurs in the gold na-

noparticle between 400 K and 500 K, as opposed to the melting that is observed for pure gold above 900K.

In the next set of simulations we considered the lower gold-sulfur binding energy of 126 kJ/mol. In these simulations the chain-chain interactions use the interaction potentials discussed earlier. In Figure 3.2c the pair correlation results for the fully coated gold nanoparticle are plotted for temperatures of 300K, 400K, and 500K. Notice that at 500K the nanoparticle is still highly structured. This indicates that the nanoparticle does not undergo a phase change at 500K as is observed in the high binding energy results. In Figure 3.2d the pair correlation results for the gold nanoparticle at 500K is compared for the uncoated, and coated nanoparticles with high and low binding energy. In this figure the effect of the high binding energy is clearly evident. The lower degree of crystallinity with the higher binding energy as compared to the lower binding energy plot indicates a more liquid-like structure at 500K.

3.4.2 Diffusion

From the results of the previous section it is apparent that the alkanethiolate SAM coating has an appreciable effect on the properties of the gold nanoparticle. In order to gain a better understanding of the SAM, and how it interacts with the gold nanoparticle we have computed the diffusion coefficient for the SAM and the gold atoms. The alkanethiolate chain is primarily bound to the gold nanoparticle through the sulfur-gold interactions at the head of the chain. The diffusion coefficient of the sulfur atoms is of particular interest because it will provide insight into the mobility of the alkanethiol chains in relation to the surface gold atoms. The diffusion coefficient of the alkanethiolate chain is calculated in the MD simulations by computing the mean

squared displacement of the sulfur head group. The diffusion coefficient, D , is then evaluated using Eq. 3.3.

$$\frac{\partial \langle r^2(t) \rangle}{\partial t} = 2dD \quad 3.3$$

In Eq. 3.3, the number of dimensions available for atomic diffusion, d , is assumed to be 3, t is time, and $\langle r^2(t) \rangle$ is the mean squared displacement (MSD) of the atoms being tracked. For computing diffusion on a surface, d would typically be 2. However, for this material system the gold atoms near the nanoparticle surface are less strongly bound to the gold atoms, and are thus more mobile. This increased mobility, particularly in the radial direction provides at least a partial third dimension for movement, although it is more constrained than for a truly free atom. This movement normal to the nanoparticle surface has not previously been considered in the simulation of SAM coated gold nanoparticles or flat surfaces, but is expected to occur because of the bonding and interactions that the sulfur atoms have with the more mobile nanoparticle surface gold atoms.

The diffusivity of the alkanethiol chain is computed by tracking the movement of the sulfur head group. By only using the displacement of the sulfur head group our results are not affected by extraneous data, such as the movement of the alkanethiol backbone. In addition to studying the diffusivity of the sulfur atoms, the diffusivity of the surface gold atoms that are bound to the sulfur atoms is also calculated. By comparing the diffusivity of the surface gold atoms with that of the sulfur atoms it is possible to determine if the alkanethiolate chains are sliding over or moving with the gold surface atoms. For example, if the diffusivity of the sulfur atoms is very different from the gold atoms then the sulfur atoms are moving over the nanoparticle surface,

the SAM chains are considered mobile, and they may nucleate. Using Eq. 3.3, the diffusion coefficients for the sulfur head group and surface gold atoms are computed to be $8.05 \cdot 10^{-7} \text{ cm}^2/\text{s}$ and $9.75 \cdot 10^{-8} \text{ cm}^2/\text{s}$, respectively. These diffusion coefficients are computed for a fully coated 50 \AA gold nanoparticle at 300 K. The difference in diffusion coefficients is about one order of magnitude, indicating that the alkanethiolate SAM is relatively mobile on the nanoparticle surface. From observations of longer simulations ($>10\text{ns}$), with low surface coverage, there is no indication of nucleation of the SAM chains. This may be expected because of the attractive potential between the alkanethiolate chain and the gold surface, so that the chain monomers prefer to bond with as many gold atoms as possible in order to minimize the system energy. As such, we see no evidence at low surface coverage of free standing groups of chains.

The diffusion coefficient of the sulfur head group has been computed for various system temperatures and presented in an Arrhenius plot in Figure 3.3. There are two linear regions with slopes of -285.9 and -3477.6 , indicating two distinct phases of the alkanethiolate SAM in the temperature ranges of $100 \text{ K} - 500 \text{ K}$ and $500 \text{ K} - 800 \text{ K}$, respectively.

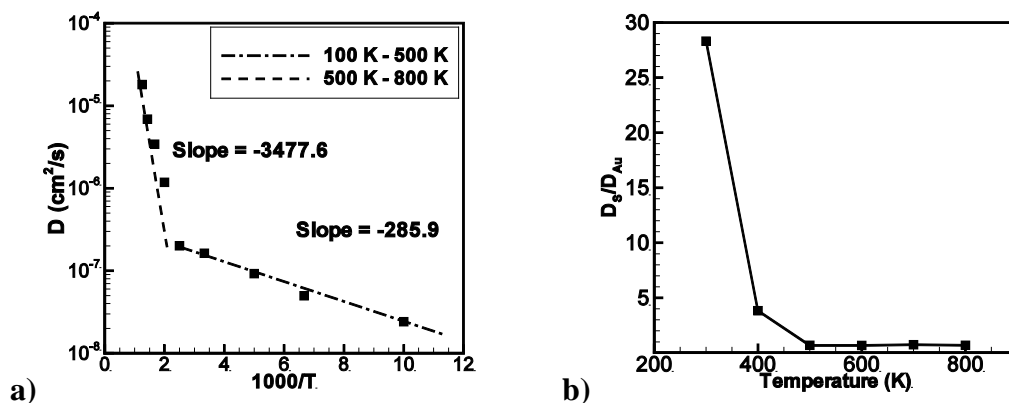


Figure 3.3: a) Arrhenius plot of diffusivity for sulfur atoms. The activation energy for SAM mobility is estimated by the slope of $\ln(D)$ vs. $1/T$ between 100 K and 800 K. b) Ratio of sulfur diffusivity to gold diffusivity in the alkanethiol coated gold nanoparticle material system.

The activation energy for the low and high temperature regions is 2.4 kJ/mol and 29.0 kJ/mol respectively. This is the expected behavior for heterodiffusion, where one type of atom diffuses on another.^{67,68} In the low temperature regime the observed activation energy corresponds to the alkanethiolate chains hopping between adsorption sites, which is observed as diffusion. For flat gold surfaces, particularly the Au(111) surface, the adsorption binding energy surface has been computed using atomistic simulations.^{19,69} These atomistic computations have determined that the difference between the minimum binding energy (face-centered cubic) site, and the maximum binding energy (atop) site is between 25.1 kJ/mol and 16.9 kJ/mol. The diffusion barrier is the energy required for an adsorbate atom to move to the next adsorption site. In Zhang et al.¹⁹ the authors have calculated the binding energy at a bridge site that would provide a possible diffusion path between adsorption sites with a diffusion barrier of 12.2 kJ/mol. Each of these published results are for flat surfaces, and report a somewhat higher activation energy than the computed activation energy

from the MD simulations for the low temperature regime. One possible explanation for the discrepancy in the calculated value is that for a curved nanoparticle surface there may be lower energy and irregular diffusion paths available for the alkanethiolate chains to diffuse along. More likely however is that all the observed activation energies are small and in part at least differences may be associated with the accuracy of the interatomic potential. Nevertheless, it does indicate a significant difference between a low temperature diffusion process, and that occurring at higher temperature.

Typically, as the temperature rises the dominant mechanism for diffusion shifts from adatoms to vacancies. However, what is occurring here is that the diffusion of the alkanethiolate chain is dominated by dissolution into the gold nanoparticle, resulting in a more highly activated process. In both instances the activation energy required for diffusion is increased, but in the former process the change in activation energy is observed to be a factor of two or more.⁶⁷ In this case the change is about one order of magnitude. The driving force for dissolution will be discussed in the next section. We notice however, in Figure 3.3b, that the diffusivity of the gold atoms is more than an order of magnitude lower than the sulfur head group atoms at low temperatures, below 500 K. This difference suggests that the alkanethiolate chains are moving freely over the gold nanoparticle surface, but at around 500K this is no longer the case, and the diffusivity of the sulfur atoms closely track those of the gold nanoparticle surface atoms. Above 500K the diffusivity of the surface gold and sulfur atoms is similar; supporting the observation that mixing of the two materials has occurred.

3.4.3 Radial Pressure Distribution

The radial pressure distribution is used in this work to quantify the affect of the adsorbed alkanethiolate SAM on the gold nanoparticle. In very small droplets the internal pressure can be much larger than the surrounding environment. One method of evaluating the radial pressure distribution is to use the normal component of the Irving-Kirkwood (IK) pressure tensor.⁴³ The IK pressure tensor comprises two terms, corresponding to a kinetic, $P_K(r,T)$, and a configurational, $P_U(r,u)$, contribution as shown in Eq. 3.4.

$$P_N(r) = P_K(r,T) + P_U(r,u) \quad 3.4$$

The kinetic pressure term is a function of temperature and the computed radial density distribution. The configurational term is computed from the interactions, u , between pairs of particles. For each shell of radius r , the forces between particles whose line of interaction intersects the shell is considered when computing the normal pressure component. The normal pressure at the surface of a nanoparticle or droplet is typically positive, indicating a compressive surface tension. The radial pressure distribution for an uncoated 50Å gold nanoparticle as a function of temperature is plotted in Figure 3.4.

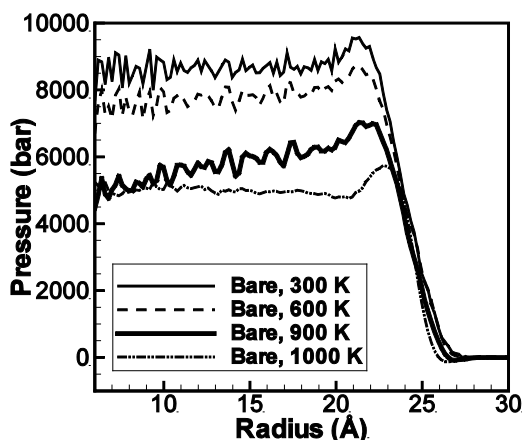


Figure 3.4: Radial pressure distribution for 50Å gold nanoparticle at various temperatures.

With the gold nanoparticle melting temperature between 900 K and 1000 K, as discussed in the pair correlation function results, the “Bare, 1000 K” curve is for liquid gold and the other curves are for a solid gold nanoparticle. The radial pressure profile below 900 K shows oscillations since the particle is in the solid phase. On the other hand, the oscillation of the pressure profile at 1000 K disappears because of greater atom mobility and indicates a phase transition in agreement with the pair correlation results previously discussed. As the temperature of the nanoparticle increases, the surface pressure decreases. This decrease of pressure with increasing temperature is expected because the reported surface tension data decreases with increasing temperature. Also, from an analysis of the terms in the IK pressure tensor, Eq. 3.4, it is apparent that if the density remains relatively constant that the kinetic pressure term will increase with increasing temperature. This means that the configurational term is decreasing at an even greater rate. The magnitude of the configurational term decreases when the interactions between the gold atoms decreases or are attractive. The fact that the configurational pressure term is negative indicates that the interactions

between the atoms is primarily attractive. The attractive potential is due to the fact that the embedding term in the EAM potential is greater in magnitude than the core repulsive term. This occurs when the gold-gold bonds are stretched as occurs during heating. Additionally, if the average coordination number of the gold atoms were to increase with increasing temperature, as is observed in silicon,⁷⁰ then the electron density would increase. This increase in electron density causes the attractive embedding term to increase while the repulsive term, which is evaluated on a pair-wise basis, will not change.

From a dimensional analysis of the Young-Laplace⁷¹ theorem shown in Eq. 3.5, this result is confirmed.

$$\Delta P = \frac{2\gamma}{r} \tag{3.5}$$

In Eq. 3.5, r is the radius of the gold nanoparticle and ΔP is the difference in pressure between the interior and exterior of the droplet, i.e. $P_{\text{inside}} - P_{\text{outside}}$. Experimentally determined and published values for gold surface tension are wide ranging and available from a limited number of sources. For the solid-gas interface the surface tension, γ_{sg} , is given as 1400mJ/m^2 , and for the liquid-gas interface, γ_{lg} , is 1128mJ/m^2 .⁷¹ For a vacuum interface, γ_{lv} is about 742mJ/m^2 at the melting point of gold.⁷² It could be expected that the difference in measured surface tension between the liquid-gas and liquid-vacuum would be minimal. From the two published sources this is not the case, and so for comparison purposes we must consider these values as representative of the expected value. Evaluation of Eq. 3.5 for our 25\AA radius particle and the published surface tension data for a vacuum interface, results in a predicted internal pressure ~ 6000 bar. This analytic result is close to that obtained from the MD

simulation at 1000K shown in Figure 3.4 . With the wide range of available data for comparison it can only be said that the predicted surface pressure and the simulated pressure are in reasonable agreement.

One can, of course, use the pressure profile from the MD simulation to directly compute the surface tension using the approach outlined by Rowlinson and Widom,⁴³ and presented in Eq. 3.6.

$$\gamma_i^3 = -\frac{1}{8} (p_{r_2} - p_{r_1})^2 \int_{r_1}^{r_2} r^3 \frac{dp_N(r)}{dr} dr \quad 3.6$$

In Eq. 3.6 p_{r1} and p_{r2} are the computed pressure at the minimum and maximum model radii, respectively, and $dp_N(r)/dr$ is the gradient of the normal pressure at radius r . Using this model, the surface tension values calculated for the bare 50Å gold nanoparticle at 900 K and 1000 K, are 751 *mN/m* and 617 *mN/m*, respectively. These temperatures bound the melting temperature of the gold nanoparticle, and the surface tension results bound the published data of 742 *mN/m*.

The combination of the results from the Young-Laplace and Rowlinson-Widom equations shows that the internal pressure computations for the uncoated gold nanoparticle are reasonable, and in the range expected. Unfortunately, there is no data available for comparison when considering the alkanethiolate coated gold nanoparticle surface.

From past efforts⁵⁶ it is expected that a surface coating will modify the nanoparticle internal pressure, through the surface tension, of the gold nanoparticle. This possibility is considered here by comparing the radial pressure distribution for gold nanoparticles with varying degrees of surface coating. The systems considered in-

clude a bare gold nanoparticle, a gold nanoparticle with only sulfur atoms adsorbed onto the surface, and finally a gold nanoparticle with alkanethiolate chains adsorbed on the surface, but with a range of interaction potentials. For bare and coated gold nanoparticles with weak SAM chain-chain interactions the internal pressure is positive, meaning a positive surface tension. This result is expected, and the decreasing pressure trend is also reasonably expected from past research involving hydrogen passivated silicon nanoparticles.⁵⁶ As observed in Figure 3.5, the pressure trends lower, and becomes negative on the interior of the fully coated nanoparticle as the chain-chain and chain-gold interaction potential parameter values are increased to the published values, indicated in Figure 3.5 by “Full Chain, 100% Cov., 300 K, full pot.”.

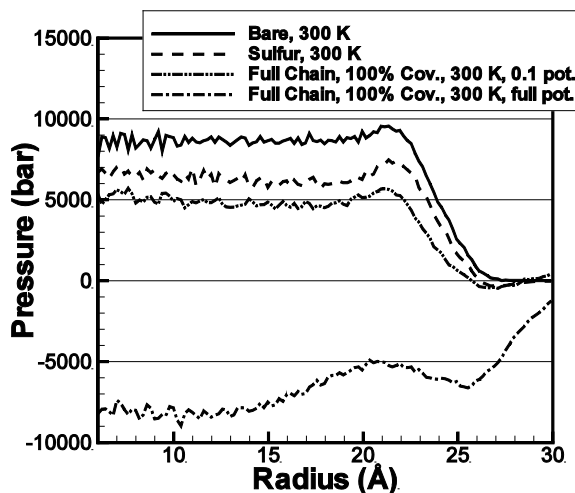


Figure 3.5: Radial pressure distribution for 50 Å gold nanoparticle with alkanethiolate SAMs with differing interaction coefficients.

As a first interpretation of this negative pressure result, one could consider the volume integral of the internal pressure distribution. Since the volume integral of the pressure distribution is negative, it indicates a mechanically unstable system, or a nanoparticle under tension. As seen in Figure 3.5, the negative pressure is observed in

the interior of the nanoparticle, and only when full chain-chain and chain-gold interactions are considered. This negative pressure result indicates that the gold nanoparticle is experiencing a tensile stress and will change its configuration over time or with increases in temperature in order to accommodate the positive stress or negative pressure. The chain-chain interactions apparently have a strong influence on the surface tension, and therefore the internal pressure of the nanoparticle. The strength of the interaction potential that will flip the internal pressure from positive and mechanically stable, to negative and mechanically unstable is still under investigation but is between 10% and 100% of the published potentials used for the alkanethiolate SAM interaction potential. Other factors that may affect the surface tension are the surface area per adsorbed alkanethiol chain, and temperature. In Figure 3.6 the radial pressure profile is plotted for a fully coated gold nanoparticle with a sulfur gold binding energy of 184.1 kJ/mol. Notice that as the temperature increases the pressure that is primarily negative at 300 K becomes positive at 700 K. As the system is held at a temperature above the melting temperature of the solution the pressure continues to increase and will most likely equilibrate to an average pressure above 0.

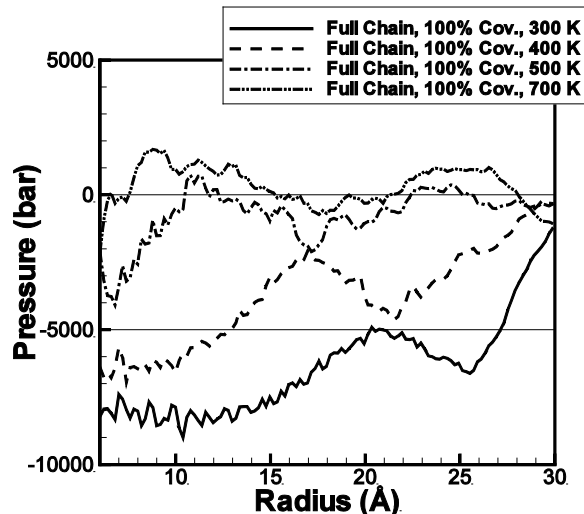


Figure 3.6: Radial pressure distribution for fully coated gold nanoparticle for range of temperatures with high binding energy (184.1 kJ/mol).

A negative surface tension resulting in a tensile stress inside the nanoparticle is not stable for a liquid nanoparticle, and will result in deformation. In a solid nanoparticle the tensile stress will exist for a time before creep⁷³ or an increase in temperature will lower the yield strength allowing the nanoparticle to yield and flow. For these reasons the solid gold nanoparticle with an alkanethiolate coating is metastable at low temperatures, but will stabilize at higher temperatures by changing shape. In this particular case, we observed as discussed in the section on diffusion that the alkanethiolate chains dissolve into the particle. This result has not been previously observed in computer simulations because the gold nanoparticle was assumed to maintain its shape, with the interaction of the alkanethiolate SAM²¹ constrained to the surface. Using the lower, 126 kJ/mol, binding energy we initially observe desorption of alkanethiolate chains from the nanoparticle surface as the temperature is increased, until the temperature is above 600K at which time the remaining alkanethiolate chains dissolve into the nanoparticle.

In Figure 3.7 the internal pressure of the alkanethiol coated gold nanoparticle is plotted from simulation data collected with a sulfur-gold binding energy of 126 kJ/mol.

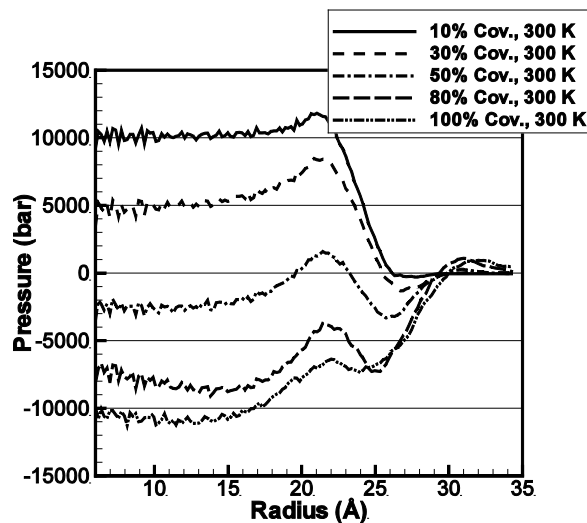


Figure 3.7: Radial pressure distribution for alkanethiol coated 50Å gold nanoparticle with 126 kJ/mol sulfur-gold binding energy.

Notice in Figure 3.7 that the internal pressure of the fully coated nanoparticle with the 126 kJ/mol sulfur binding energy is very similar to the internal pressure of the fully coated gold nanoparticle in Figure 3.5, where the binding energy of the sulfur-gold bond is 184 kJ/mol. Recall that only the sulfur-gold binding energy has been changed in Figure 3.7, whereas in Figure 3.5 the “0.1 pot.” curve represents data collected from simulations where the sulfur-gold and the chain-chain interactions have both been modified. By comparing these results we can conclude that the chain-chain interactions have a greater affect on internal pressure than the sulfur-gold binding energy. This is an important result because although the sulfur-gold binding energy has some affect on the structure of the gold nanoparticle and diffusivity, it is not the primary factor in determining stability of the nanoparticle. Additionally, the affect of

chain length on the radial pressure distribution is also considered. After computing the radial pressure distribution for alkanethiol chain lengths of 3 and 18 carbon atoms, we have found that the shorter chains result in an internal pressure about 5000 bar higher than the previously considered 9 carbon atom chains. Alternatively, the longer chains don't appear to have a greater affect on the internal pressure of the nanoparticle than the 9 carbon atom chains studied here. This leads to the conclusion that for the number of monomers considered, a longer chain has little affect on the stability of the nanoparticle, whereas a shorter chain will lower the total chain-chain interaction sufficiently to affect the nanoparticle stability.

3.4.4 Radial Density Distribution

From the computed results up to this point we have determined that the 50Å uncoated gold nanoparticle has a melting temperature between 900 K and 1000 K (pair correlation function), the SAM chains are mobile on the gold surface (diffusion coefficient), and that there are two phases for the adsorbed alkanethiolate SAM between 100 K and 800 K. In this section, the radial density results are analyzed. The radial density is computed as part of the radial pressure calculation, discussed previously. For bare nanoparticles, the radial density distribution for the gold atoms will change abruptly at the nanoparticle surface from the core density to zero. On the other hand, for coated nanoparticles, if the surface atoms move radially outward due to the presence of the alkanethiolate chains penetrating into the particle, the slope of the radial density distribution will be less steep. This phenomenon of the SAM chains penetrating into the nanoparticle surface is not a previously predicted result because past efforts to simulate alkanethiolate coated gold nanoparticles have assumed that

the gold atoms do not move as a result of the interactions with the SAM.^{21,33} These previous results have either assumed a flat surface or a nanocrystallite with immobile atoms. Modeling the gold atoms using the EAM potential provides for an investigation of whether or not the gold atoms are affected by the SAM. When analyzing the radial density, shown in Figure 3.8, it is apparent that the atoms near the surface of the gold nanoparticle are less densely packed than those in the nanoparticle core. This decrease in gold atomic density suggests that near the nanoparticle surface, the gold atoms are mixing with the alkanethiolate molecules.

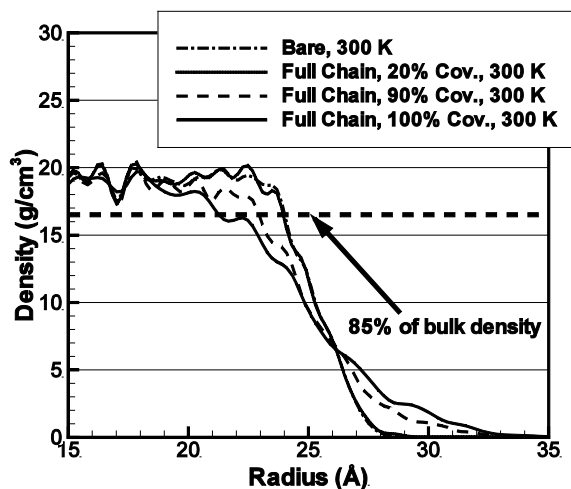


Figure 3.8: Radial density of gold in alkanethiolate SAM coated gold nanoparticle for various surface coverage amounts.

The results in Figure 3.8 show the expected steep slope for the radial density distribution of the uncoated gold nanoparticle. The slope is not vertical because the nanoparticle is nonspherical, but rather has large facets.⁵⁰ The slope of the radial density plot for the coated gold nanoparticle is less steep than the uncoated nanoparticle. The slope decreases monotonically as more SAM chains are adsorbed onto the gold surface. This decrease in slope indicates that the atoms near the surface are more dif-

fuse, resulting in the lower measured density of gold. The depth to which the gold core is affected we have labeled as the surface corrugation.

In order to quantify the surface corrugation we have defined by Eq. 3.7 a corrugation factor, C .

$$C = \frac{r(\rho = 0.85\rho_{\text{bulk}})_{\text{bare}} - r(\rho = 0.85\rho_{\text{bulk}})_{\text{coated}}}{r(\rho = 0.85\rho_{\text{bulk}})_{\text{bare}}} \quad 3.7$$

In Eq. 3.7, $r(\rho = 0.85\rho_{\text{bulk}})$ is the radial position where the computed gold density is 85% of the density of bulk gold, and the subscripts bare and coated refer to the uncoated and alkanethiolate SAM coated gold nanoparticle, respectively. This definition of the corrugation factor will produce a value of 0.0 for the bare gold nanoparticle and maximum of 1.0 for a gold nanoparticle with impurities or a dissolved solute. For coated gold nanoparticles with various percentages of surface coverage the corrugation factor has been computed, and is listed in Table 3.1.

Table 3.1. Computed corrugation factors for alkanethiolate SAM coated gold nanoparticles.

Coverage	$C_{184 \text{ kJ/mol}}$	$C_{126 \text{ kJ/mol}}$	$C_{\text{weak chain}}^1$
Bare	0.000	0.000	N/A
10%	0.004	0.003	N/A
70%	0.012	0.018	N/A
80%	0.018	0.013	N/A
90%	0.043	0.020	N/A
100%	0.107	0.081	0.019

¹ The gold-sulfur binding energy is 184 kJ/mol but all chain-chain interactions are at 10%.

The results presented in Table 3.1 show that the corrugation factor remains small, indicating little change in the nanoparticle surface, for SAM coverage below 90%. Once the coverage reaches 90%, the corrugation factor increases 2.5 times over the value at 80%, and increases by another factor of 2.5 times between 90% and 100%. With a corrugation value of 0.107, in column $C_{184 \text{ kJ/mol}}$, at full surface coverage the core of the gold nanoparticle is only about 89% of its original size. This result has two implications; first, that the surface area of the gold nanoparticle has increased because the surface is no longer smooth but wrinkled, second, the SAM chains are able to form more bonds to the increased number of exposed gold atoms, potentially increasing the binding energy of the SAM to the gold nanoparticle. The results in Table 3.1 indicate an exponential dependence of the corrugation factor on the amount of surface coverage.

In the column for the lower sulfur-gold binding energy, namely $C_{126 \text{ kJ/mol}}$, the corrugation is less pronounced indicating a lower surface effect from the adsorbed SAM. The difference in magnitude of corrugation between the high and low binding energies is relatively small, about 25%. This small change in corrugation from a 33% change in gold-sulfur binding energy may indicate that the gold-sulfur binding energy is not the most important factor in determining surface corrugation. In the final column of Table 3.1 the gold-sulfur binding energy is 184 kJ/mol but all chain-chain interactions have been lowered to 10% of the previous magnitudes. Only the 100% surface coverage data is computed, but by comparing this result with the other columns it is apparent that the chain-chain interaction has an appreciable effect on the surface

corrugation. The 90% drop in chain-chain interactions is accompanied by an 83% drop in corrugation. This is proportional to the change in corrugation observed by lowering the sulfur-gold binding energy alone.

There is experimental support for corrugation of the gold surface from the adsorption of an alkanethiol SAM.⁷⁴ In the experimental measurements it is assumed that an interior gold atom is pulled onto the surface to become an adatom. In this case the alkanethiolate chain then bonds atop this gold adatom and the gold surface is thus corrugated. Another consequence of this adatom is that the alkanethiolate is more mobile and could be construed as a lower total sulfur to gold surface binding energy than if the sulfur atom were in the vicinity of many gold atoms. A rough estimate of the measured corrugation in this case would be the gold-gold bond distance divided by the nanoparticle radius, resulting in $C_{\text{exp}}=0.116$, a result similar to the values in Table 3.1 for a 100% coated surface.

3.5 Phase Behavior and SAM Solubility

The computed potential energy (PE) of the alkanethiolate SAM coated gold nanoparticle system is used to determine the critical temperature at which mixing and phase change will occur. The computed slope of the PE versus temperature curve from the MD simulation results are used to determine the heat capacity of the system.

In Figure 3.9, the system PE is plotted versus temperature for a 50Å gold nanoparticle coated with increasing densities of the alkanethiolate SAM. For the bare nanoparticle there is a discontinuity around 980 K, which corresponds to a phase change. The SAM coated nanoparticle demonstrates a very different behavior. Initially, for small numbers of adsorbed alkanethiolate chains, the melting temperature of

the gold nanoparticle decreases, and does not occur at a unique temperature but rather over a range of temperatures. This behavior is expected for a mixture of two materials.⁷¹ The appearance of the SAM on the particle surface decreases the surface tension and internal pressure. As the coverage percentage is increased further, another behavior is observed. At higher surface coverages, above 70%, the PE of the system begins to decrease as the temperature is increased, and then after a small temperature range the PE resumes its linear increase. This behavior is explained by the mixing that occurs between the alkanethiolate chains and the gold atoms. The mixing of the SAM chains with the gold atoms is possible because of the lower binding energy of surface Au atoms. The lower binding energy of the surface atoms allows these atoms to become mobile at a lower temperature than the interior gold atoms.⁵² The surface atoms begin to mix with the alkanethiolate chains, and as the chains penetrate deeper into the nanoparticle they are able to interact with an ever increasing number of gold atoms. Once complete mixing has occurred, the PE resumes increasing monotonically.

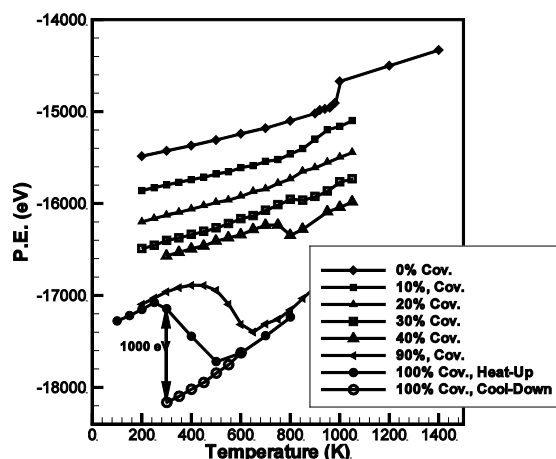


Figure 3.9: Potential energy versus temperature for the alkanethiolate SAM coated gold nanoparticle with various amount of surface coverage and the 184 kJ/mol sulfur binding energy.

As we found with the internal pressure in Figure 3.5, the structure of the SAM coated gold nanoparticle is metastable. The increase of both the surface coverage and the temperature aids this particle in transforming into a mixed structure, Figure 3.10. This result has not been previously predicted, as it was previously assumed that the SAM chains would desorb at these temperatures, as occurs on flat surfaces.¹⁹ If the SAM were to desorb, it is expected that the structure of the underlying gold nanoparticle would not be affected. This is reflected in the pair correlation data discussed earlier that shows that the gold nanoparticle with SAM coating is crystalline at a higher temperature with the lower 126 kJ/mol sulfur binding energy than with the 184 kJ/mol binding energy.

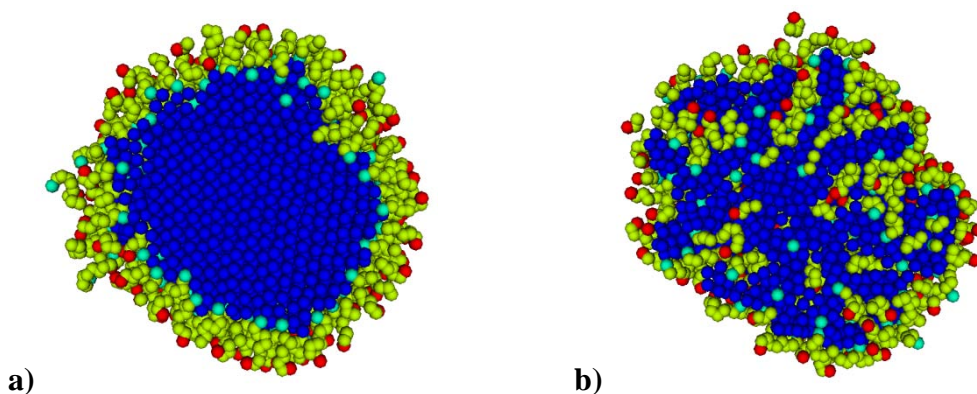


Figure 3.10: Cross section of 100% coated gold nanoparticle at 300K (a) and 600K (b), showing the dissolution of the alkanethiol chains at high temperatures. In these images the blue spheres represent gold atoms, light blue are sulfur, yellow are CH_2 and red spheres represent CH_3 .

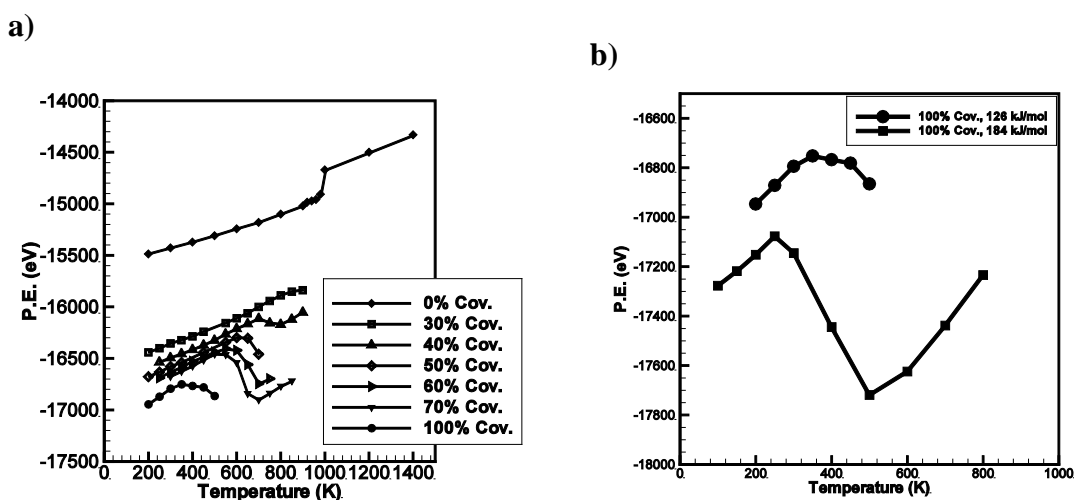


Figure 3.11: a) Potential energy versus temperature for the alkanethiolate SAM coated gold nanoparticle with various amount of surface coverage and 126 kJ/mol binding energy. b) Comparison of potential energy versus temperature for fully coated nanoparticle with 184 kJ/mol and 126 kJ/mol binding energy.

In Figure 3.11a, the PE for the 126 kJ/mol sulfur binding energy simulation is plotted along with the same curve for the higher 184 kJ/mol binding energy. During these simulations, as opposed to the 184 kJ/mol binding energy simulations, we observed some desorption of alkanethiol chains from the gold surface. This desorption process is irreversible because of the low density of desorbed chains in the simulation

volume, a realistic assumption for coated nanoparticles in a vacuum or near vacuum. In Figure 3.11b it is interesting to note that the temperature at which the decrease in PE occurs for the 126 kJ/mol sulfur binding energy is higher than the 184 kJ/mol binding energy simulations. This result confirms the observation that when considered with a lower sulfur binding energy that the alkanethiol chains have a lower propensity to dissolve into the gold nanoparticle and a higher probability of desorbing from the gold surface.

The constant volume heat capacity, C_v , of the nanoparticle system is computed directly from the slope of the PE versus temperature curve. The portion of the PE versus temperature curve used to determine the heat capacity is that below the melting temperature, or prior to mixing. For the nanoparticles studied in Figure 3.9, the specific heat capacity, C_v , is computed and plotted in Figure 3.12 for increasing amounts of surface coverage. In Figure 3.12 the computed heat capacity of the system per unit mass is increasing with increasing surface coverage. This result is reasonable since gold has a relatively low specific heat compared with the alkanethiolate chains. As more chains are added to the nanoparticle surface the fraction of the total system mass that they represent increases, resulting in the increase in the system heat capacity.

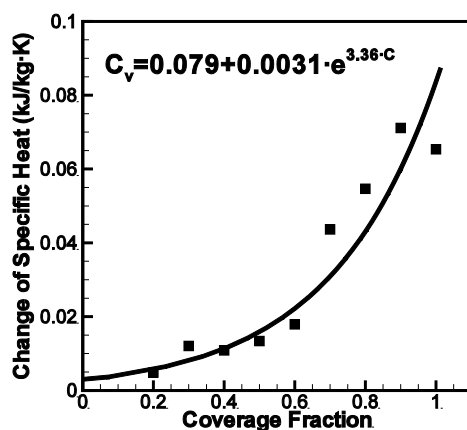


Figure 3.12: Plot of specific heat versus surface coverage for alkanethiolate SAM-coated gold nanoparticle showing exponential relationship between specific heat and surface coverage.

In addition to the heat capacity, the enthalpy of solution, H_{sol} , can be computed from the PE data. The enthalpy of solution is computed as the difference in system internal energy, between the undissolved SAM chain system prior to heating and the internal energy of the same system after cooling down to the same temperature. The PE of the system decreases as a result of the mixing that occurs in the fully coated gold nanoparticle model during an increase in temperature from 300 K to 600 K. This mixing may potentially occur completely at 300 K if it were possible to simulate long times (greater than 10 ns) in the MD simulations performed here. On the other hand, it is also possible that the activation energy for this transition to occur may be too high to complete the transition at 300 K. The measured change in system PE is 1000 eV, which is the enthalpy of solution.⁷¹ Denoting this result per unit mass of the fully coated gold nanoparticle results in an enthalpy of solution of 100 kJ/kg. These results show that the SAM has a measurable effect on not only the nanoparticle surface but the entire system.

3.6 SAM Phases

Determining the phase diagram of the SAM chains on a gold surface is of fundamental interest. There has been extensive effort to understand the various phases of the alkanethiolate SAM chain on flat gold surfaces,⁷⁵ that have found four distinct phases. The four phases are; a striped phase at low surface coverage, where the chains lie flat along the gold surface, intermediate structures for higher surface coverage, where some chains are partially standing, and others are lying flat. At high surface coverage the alkanethiolate chains are either in a highly structured $c(4 \times 2)$ phase³⁴ at low temperatures, or a more random liquid phase at higher temperatures. In this work, as in previous work involving flat surfaces, we have investigated surface coverage and temperature as determining factors for the phase of the SAM.

It is expected that the binding energy of an alkanethiolate chain to the gold surface is dependent on whether the chain is lying along the surface of the nanoparticle (physisorption for longer chains, or chemisorption for shorter chains) or standing radially outward with only the head group sulfur atom interacting with the gold surface (chemisorption).⁴⁵ The orientation of the chain is determined by measuring the tilt angle of the alkanethiolate chain which is computed by comparing the radial position of the sulfur head group to the CH_3 tail group. For an alkanethiol chain lying along the nanoparticle surface the difference in radial position between the head and tail groups will be very small. When a chain is tilted upward the radius will be at a maximum value. This radius data is then used to estimate the angle that the chains make with the nanoparticle surface and to measure the monolayer thickness.⁷⁶

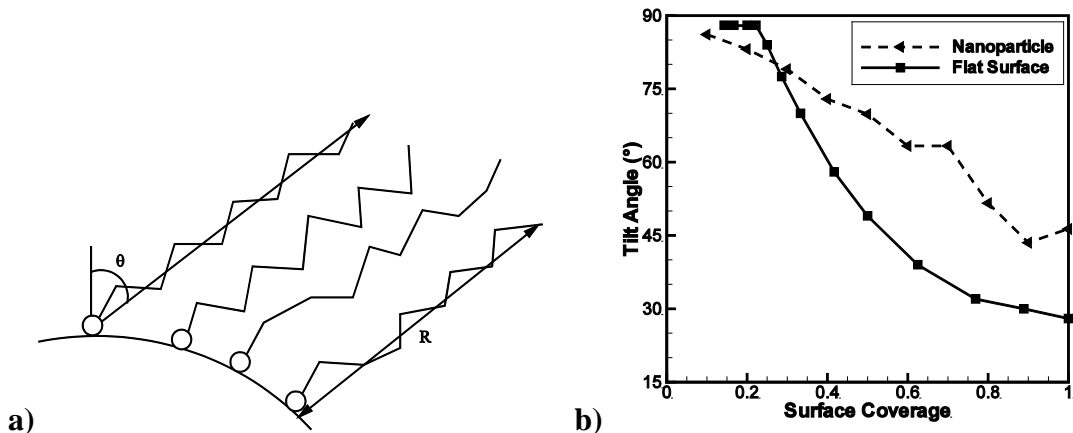


Figure 3.13: Difference in radial position for the head and tail groups of the alkanethiolate chains at various surface coverage densities, drawing (a) and tilt angle (θ) (b). The alkanethiol radius is also labeled as the monolayer thickness

In Figure 3.13b, the tilt angle of the alkanethiol SAM is plotted for 10% to 100% surface coverage. At low surface coverage the alkanethiol chains lie along the surface of the nanoparticle as indicated by the almost 90 deg. tilt angle. In between the high and low surface coverage regions the alkanethiolate chains begin to stand radially outward from the nanoparticle surface. Above 90% surface coverage the chains have all orientated themselves with the minimally observed tilt angle from the nanoparticle surface, and the maximum difference in radial position is observed. The tilt angle for the alkanethiolate SAM on a flat gold surface is also plotted for comparison. The steeper drop in angle and minimum tilt angle for the flat surface are both attributable to the geometric issues discussed next and illustrated in Figure 3.14.

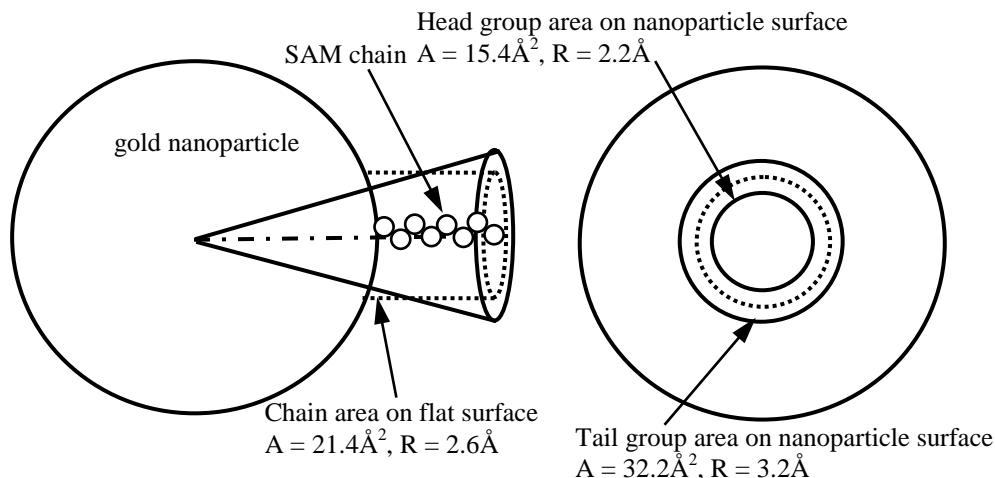


Figure 3.14: Drawing showing the difference in space occupied by tail molecule on curved and flat gold surfaces. Assuming a chain length of 9 carbon atoms.

In Figure 3.14a side and front views of an idealized spherical nanoparticle are illustrated with an alkanethiolate chain extending radially from the nanoparticle surface. The conic section in Figure 3.14 shows the volume associated with an alkanethiol chain adsorbed to the surface of a nanoparticle. The cylinder is the volume associated with an alkanethiolate chain on a flat surface. Notice that the area of the cone sliced at the nanoparticle surface is smaller (15.4Å^2) than the area of the cylinder (21.4Å^2). This gives rise to the higher packing density on the nanoparticle surface compared to the flat gold surface. At the tail of the alkanethiolate chain, for chains with 9 carbon atoms as considered here, the cone has a larger cross-sectional area than the cylinder. This larger area means that the tail of an alkanethiolate chain has less restricted movement than the tail of an alkanethiolate chain adsorbed onto a flat surface. This greater freedom of movement results in the higher tilt angle measured in this work (42 deg.) compared to the tilt angle measured for a flat gold surface (about 30 deg.).^{19,34}

3.7 Conclusions

The alkanthiolate SAM-coated gold nanoparticle has been shown to be mechanically and chemically metastable. The SAM that is adsorbed onto the surface begins to mix with the surface gold atoms at low temperatures because of the weaker gold-gold bonding of the surface atoms to the interior gold atoms. This process is more pronounced as the density of the SAM is increased and as the gold-sulfur binding energy is increased. This is demonstrated by the corrugation numbers computed previously. For full surface coverage, the SAM chains will begin to diffuse into the gold core as the temperature rises from 300 K to 500 K. This mixing process lowers the PE of the system. The diffusion activation energy of the sulfur atoms is measured to be low in this temperature range. Once the temperature has increased to around 600 K, the alkanethiolate chains are completely mixed with the gold atoms, and the activation energy for diffusion greatly increases. The PE and diffusivity results concur with this observation that a phase change in the SAM-coated gold nanoparticle system occurs around 500 K. We have therefore concluded that the melting temperature of the gold is lowered by the adsorption of alkanethiolate SAMs on the nanoparticle surface and creates a metastable system for fully covered nanoparticles of diameters around 50Å. The measured decrease in melting temperature of the nanoparticle is more pronounced as more SAM chains are adsorbed onto the nanoparticle surface.

We have also compared each of the computed results for the low, 126 kJ/mol, gold-sulfur binding energy reported in the literature to the results from the high, 184 kJ/mol binding energy. These comparisons show that the gold-sulfur binding energy does not have a large affect on the meta-stability of the nanoparticle. From these re-

sults we are able to conclude that the primary factor in determining if a nanoparticle will become metastable is the strength of the chain-chain interactions. Since experiments concur that desorption occurs in the 300K to 550K temperature range we have concluded that the 126 kJ/mol binding energy is most likely a better estimate of the true binding energy than the 184 kJ/mol value. Independent of the binding energy is the tilt angle, which is found to be greater for the nanoparticle geometry than for a flat surface.

4 Molecular Dynamics Simulation of the Energetic Reaction of Ni and Al Nanoparticles

4.1 Introduction

Nanoparticles have interesting physical properties that often vary from the bulk material. Some of these properties, including increased reactivity,⁷⁷ are due to the high surface area to volume ratio of nanoparticles, increased defects, and an altered electronic structure. With this in mind nanoparticles may provide enhanced energy release rates for explosive and propellant reactions.⁷⁸

There is considerable interest in the self-propagating high-temperature synthesis (SHS) reactions of intermetallic compounds because of the associated energy release that takes place⁷⁹ during the alloying reaction. In addition to the energetic reaction observed in these materials it is also possible to produce structural materials that contain this energy release property. Some of the application areas for SHS include alloy formation, net-shape processing, propellants, as initiators and when it is desirable for the reactants and products to be confined to the condensed state.⁸⁰

One of the compounds formed from the SHS reaction, and studied here, is NiAl or nickel aluminide. NiAl is an important alloy because of its desirable high temperature strength and oxidation resistance, due to the formation of a protective Al₂O₃ scale⁸¹ and its high energy of formation.⁸² Recently Weihs and coworkers have also used NiAl nanolaminate systems in applications of reactive welding.⁸³

Not surprisingly since the reaction involves solid starting materials, particle size has a significant effect on the properties of the reaction product and the SHS

reaction itself.⁸⁴ The simulation and analysis of nanoparticle coalescence without the SHS reaction for like materials is extensive^{52,56,85-88} and involves surface passivation,⁵⁶ size differences,^{52,85} and phase change⁵² considerations. The analysis here includes all of the previously listed concerns with an additional energy release term from the heat of formation.

The focus of this chapter is to use atomistic simulation to simulate the reactive behavior of Ni and Al nanoparticles in various configurations. Fortunately, there have been numerous efforts to determine accurate empirical potentials for simulating the Ni-Al material system.⁸⁹ Prior simulations using these empirical potentials have investigated the diffusion of Ni and Al atoms,⁸⁹ point-defect concentrations in NiAl,⁴¹ and plasticity⁹⁰ in addition to many other mechanical and chemical properties. These efforts have primarily focused on bulk materials rather than nanoparticle systems,⁹¹ even though there are many manufacturing processes that produce nanometer sized powders for SHS reactions.⁹² For this simulation effort we have chosen a set of EAM parameters that reproduce reasonably well the properties of Ni, Al, and NiAl in the temperature range of interest.

4.2 Simulation Approach

In this work we use the EAM to simulate the interactions of aluminum and nickel atoms. The EAM is used because of its accuracy and capability to scale up to material systems with over 10^6 atoms. The MD simulations are compared with thermodynamic analyses in order to provide validation of the simulation results and assess the expected energy release.

The MD simulations in this work was conducted using the LAMMPS software package.⁹ For the Ni-Al interactions the Finnis-Sinclair EAM potential⁹³ from Angelo et al.⁴⁰ was used. The Finnis-Sinclair EAM potential allows for non-symmetric embedding potential terms, potentially providing improved accuracy for metallic alloys.⁹⁴ In addition to the parameters for NiAl from Angelo et al. other authors have also developed parameters for the Ni-Al system⁴¹ that may also be described by using the Finnis-Sinclair EAM. In particular the parameter set from Mishin et al⁴¹ was found to severely over predict the melting temperature of pure aluminum which is an important parameter for this analysis.

Three primary nanoparticle sizes were considered in this work, from smallest to largest they are nanoparticles with 1289, 5635, and 36523 atoms each, which correspond approximately to aluminum nanoparticle diameters of 3nm, 5nm, and 10nm, respectively. The range of sizes was chosen because it represents nanoparticles that may be produced in the laboratory, and which offers reasonable computational time to conduct parametric studies. For the largest system studied, the 10nm diameter nanoparticle, the energetic reaction simulation requires approximately two days and 64 processor cores to complete a few nanoseconds of simulated time on 3.0 GHz Intel Woodcrest processors.

4.3 Thermodynamic Analysis of Separate Nanoparticles

The sintering of separate nanoparticles is used as a model for powder metallurgy systems where Ni and Al particles are compressed into a structural component. In addition to mechanical properties, the structural component will contain stored energy for future release through a SHS reaction. A thermodynamic analysis of the SHS

reaction for the separate Ni and Al nanoparticle system is used here to determine the expected trends and data points for simulation validation. With the thermodynamic analysis provided here we are interested in determining the system parameters of the Ni-Al nanoparticle system that contribute to the combustion temperature and reaction time. Here we have assumed an adiabatic process so that energy released to the surroundings can be ignored. This is a good approximation since the reaction occurs on relatively short time scales and the nanoparticles are expected to be included in a much larger system where the overall surface to volume ratio is small, limiting convective and radiative heat loss. The validity of this assumption is explored in a later section. The SHS reaction of an equimolar Ni and Al mixture is written as



In order to compute the adiabatic temperature for the synthesis reaction in a vacuum the enthalpy of the products and reactants must be equal.

$$H_{prod}(T_{ad}) = H_{reac}(T_0) \quad 4.2$$

Assuming that the reaction begins with the reactants at 600K, above the simulated melting temperature of the Al nanoparticles, the enthalpy of the reactants is computed as,

$$H_{reac} = (0.5)(H_{Al, fusion}) + (0.5)(H_{Al, 600K} + H_{Ni, 600K}) = 11.85 \text{ kJ/mol} \quad 4.3$$

This enthalpy result includes the enthalpy of solid Ni and liquid Al.⁸² The Al nanoparticle is assumed to be liquid because for small nanoparticles the melting temperature is known to be appreciably below the bulk melting temperature.⁹⁵ Additionally, for the EAM potential used here⁴⁰ the aluminum is liquid for these nanoparticle sizes at 600K. The choice of initial temperature will have a nearly linear affect on the adia-

batic temperature as long as the temperature is between the melting temperature of the Al and Ni nanoparticles. This linear affect has been observed in experiments,⁹⁶ and is a reasonable assumption so long as the heat capacities of the solid phases of Ni and NiAl are relatively insensitive to temperature in the ranges studied.

For the products of the SHS process the enthalpy calculation must take into account contributions from the melting of the nickel and the NiAl nanoparticle, enthalpy of formation for the NiAl alloy, and changes in surface energy. The first of these, the enthalpies of melting for Ni and NiAl have been experimentally determined to be 17.2 kJ/mol and 31.4 kJ/mol , respectively. The enthalpy of mixing for Ni and Al has garnered close scrutiny in the experimental community with a wide range of reported values. The enthalpy of formation that is used here is approximately in the middle of the reported values at about -65 kJ/mol .^{82,97,98}

The final contribution to the enthalpy of the products, results from the change in surface energy, due to the reduced total surface area of the combined nanoparticle.⁷⁰ The contribution to the change in system energy from the change in surface area is given as equation 4.4.

$$\Delta E_{surf} = \sigma_{NiAl} \cdot a_{NiAl} - (\sigma_{Ni} \cdot a_{Ni} + \sigma_{Al} \cdot a_{Al}) \quad 4.4$$

In equation 4.4, a_{NiAl} , a_{Ni} , and a_{Al} are the surface areas of the NiAl, Ni, and Al nanoparticles, respectively. For the 3nm, 5nm, and 10nm Al nanoparticles at 600K the reactant surface area is computed from the Gibbs surface⁴ as 36.32 nm^2 , 98.17 nm^2 , and 343.7 nm^2 , respectively. For the associated Ni nanoparticles at the same temperature the surface area is 27.15 nm^2 , 73.59 nm^2 , and 257.87 nm^2 , respectively. The surface energy is approximately 1115 mJ/m^2 for Al and 2573 mJ/m^2 for Ni at 600K.⁹⁹ The

surface area of the sintered NiAl nanoparticles is 50.77 nm^2 , 137.18 nm^2 , and 480.25 nm^2 for the 3nm, 5nm, and 10nm nanoparticle case, respectively. In experimental analysis of the free surface energy of NiAl near its melting point, the free surface energy has been reported as 1400 mJ/m^2 .¹⁰⁰ The approximate change in energy versus nanoparticle size is tabulated in Table 4.1.

Table 4.1: Change in surface energy versus nanoparticle size.

<u>Nanoparticle Radius (nm)</u>	<u>ΔE_{surf} (kJ/mol)</u>
3	-18.35
5	-11.41
10	-6.17

In Table 4.1 the trend is for a lower surface energy contribution to the reaction as the nanoparticle size increases. Intuitively, one may expect this because the surface area to volume ratio is also decreasing with increasing particle size, and therefore has less influence on the sintering process. With the enthalpy of formation for NiAl around -65 kJ/mol , the surface energy contribution to the change in enthalpy for sintering of 10nm diameter nanoparticles is less than 10% of the total enthalpy change. This means that even at relatively small nanoparticle sizes, e.g. 10nm, the affect of nanoparticle size on energy release is minimal.

With the preceding discussion it is possible to take into account many of the sources of enthalpy change in the reaction products including phase and surface area changes. The enthalpy of the products is now estimated as

$$H_{prod} = H_{form, NiAl} + \Delta H_{surf} + \int_{298K}^{T_{ad}} C_{p, NiAl}(T) dT + H_{melt, Ni} \quad 4.5$$

The heat capacity for solid and liquid NiAl is given in Kubaschewski et al.¹⁰¹ For the 3nm case, assuming the NiAl nanoparticle melting temperature to be about 1350K, or the melting point of a similarly sized Ni nanoparticle it is possible to compute the adiabatic reaction temperature, table 2.

Table 4.2: Computed adiabatic temperature versus nanoparticle radius, including contact of flat surfaces or infinitely sized spheres.

<u>Nanoparticle Radius (nm)</u>	<u>T_{ad} (K)</u>
3	2115
5	1920
10	1772
∞	1599

Notice in table 2 that if no surface energy contribution is considered, i.e. infinitely large spheres, the final adiabatic temperature is computed to be 1599K. In the simulation section we will observe that these results are reasonable and accurately predict the simulated increase in temperature attributable to the contribution from the surface energy.

4.4 The Coalescence Processes

For Ni and Al nanoparticles the SHS reaction consists of two processes, namely coalescence and alloying. In this work we have considered the coalescence of a two nanoparticle system with an Al and a Ni nanoparticle with an atomic ratio of unity. A

complete SHS reaction of this system will result in a single NiAl nanoparticle. The MD simulations used to work model adiabatic conditions with constant number of atoms and total system energy. The purpose of these simulations is to analyze the affect of nanoparticle size on sintering time, adiabatic combustion temperature, and to visualize the process. The assumed process is illustrated in Figure 4.1.

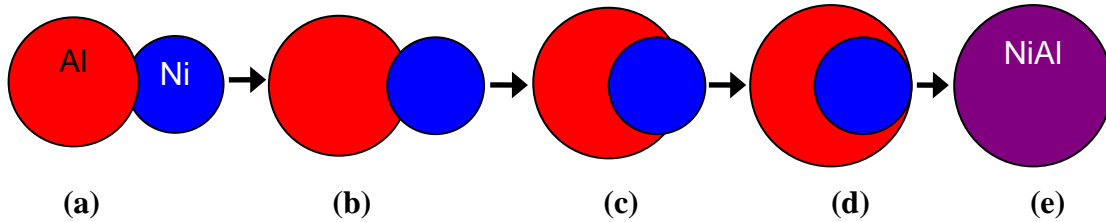


Figure 4.1: Illustration of coalescence process showing liquid Al nanoparticle first coating the solid Ni nanoparticle and then complete alloying after the Ni nanoparticle has melted.

In Figure 4.1 the nanoparticles are initially in contact at a point (a) and the Al nanoparticle is larger than the Ni nanoparticle because of the longer Al-Al bond length. The simulations are initialized at 600K so that the Al nanoparticle is liquid and the Ni nanoparticle is solid. In Figure 4.1 the sintering process proceeds with the liquid Al nanoparticle initially coating the solid Ni nanoparticle while forming some Ni-Al bonds on the surface (b-d). Next, the alloying process proceeds with the Ni nanoparticle being heated above its melting point and becoming liquid so that mixing may occur (e). The formation of Ni-Al bonds beyond the interfacial surface requires diffusion of Al into the Ni nanoparticle or Ni into the liquid Al. Either of these processes is possible but since diffusion is a relatively slow process in solid materials it is expected that the Ni nanoparticle must melt before the coalescence process proceeds appreciably.

The nanoparticle sintering process is driven by two sources of energy as previously discussed. The first of these is a decrease in surface area that lowers the total surface energy of the system. This energy release mechanism is also observed in the sintering of homogeneous material systems such as silicon nanoparticles.^{70,102} The second source of energy is from the reactive synthesis that occurs initially at the interface between the nanoparticles and later throughout the entire system. The energy release from the surface sintering is proportional to the surface area of the Ni nanoparticle that is coated by Al and in the whole system to the total number of Ni and Al atoms. Additionally, with the temperature increase there is a decrease in the viscosity of the liquid aluminum that will affect the predicted coalescence time.

The coalescence of nanoparticles in the liquid and solid phases has been examined extensively.^{52,56,85} These studies are primarily concerned with the coalescence of two liquid or two solid nanoparticles. The analysis for the Ni-Al system requires considering the coalescence of a liquid Al nanoparticle and a solid Ni nanoparticle. Lewis et al⁵² considered the coalescence of a liquid and a solid gold nanoparticle, this is similar to the situation here except that the material system considered was homogeneous.

In Lewis et al⁵² the author is able to simulate two phases occurring simultaneously for a single material by choosing the size of each nanoparticle such that at a specific temperature the phase of the nanoparticles is different. Lewis found that coalescence proceeded in two stages, first the contact area was maximized and secondly “sphericization” took place driven by surface diffusion. The first stage is much faster than the second and is very similar to the process observed here where the Al nano-

particle maximizes the contact area and partially coats the Ni nanoparticle. In this case there is an added driving force in addition to the surface energy, specifically the energy release on forming of Ni-Al bonds as compared to the formation of Al-Al and Ni-Ni bonds. During the second stage the atoms in the two nanoparticles diffuse and rearrange until the system becomes a single spherical nanoparticle. This stage is driven strongly by the formation of Ni-Al bonds and is expected to occur on a much shorter time scale than for two nanoparticles of the same material. The analytical model and MD simulation results shown in the following sections will explore this assumption.

4.5 Phenomenological Model of Nanoparticle Reactive Sintering

To gain further insight we have developed a phenomenological model for the reactive sintering of Ni and Al nanoparticles. The model includes energy release from surface energy, bond formation, and viscous dissipation through deformation. Frenkel¹⁰³ has developed a model for the coalescence of two homogeneous nanoparticles, however his model did not account for any phase change, exothermic sintering, or heterogeneous materials. Here we extended Frenkel's model for the coalescence of two liquid drops to consider the coalescence of a liquid and a solid drop with reactive synthesis.

The analytical model is initialized with the Al and Ni nanoparticles in contact at a point. The distance from nanoparticle center to center is equal to the sum of the respective radii, denoted as D in Figure 4.2. The sintering process initially proceeds by the liquid Al nanoparticle coating the solid Ni nanoparticle, as illustrated in Figure 4.1. During this phase of the sintering process, two sources of energy release are oc-

curing; the first of these is related to the decrease in surface area and is proportional to the respective surface tension values. The second source of energy release is from the formation of Ni-Al bonds at the interfacial region.

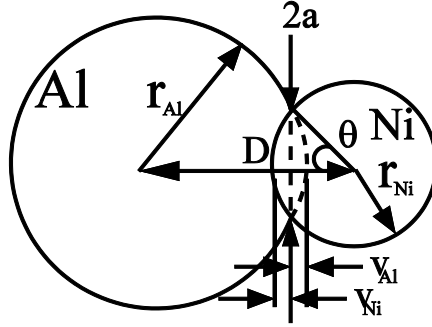


Figure 4.2: Illustration of parameters used in analytical model of reactive coalescence of Ni and Al nanoparticles.

In Figure 4.2, $2a$ is the diameter of a circle circumscribed by the contact circumference of the two nanoparticles. v_{Al} and v_{Ni} are the distance from the Al and Ni nanoparticle surface to the surface of the contact circle, respectively. θ is the contact angle as measured from the center of the Ni nanoparticle and ranges from 0 to π radians. In order to model the change in energy of the coalescing nanoparticle system, three energy change mechanisms must be considered. These mechanisms are energy release due to change in surface area, energy release due to energetic reactions at the interface, and energy loss due to viscous dissipation. The rate of energy change due to all three must balance at all times.

The first energy term considered, namely the surface energy of the nanoparticle system, is simply the surface tension times the total exposed surface area. This energy term is written as a sum of the Al and Ni nanoparticle contributions.

$$E_{surf} = \sigma_{Ni}^s \cdot S_{Ni,exposed} + \sigma_{Al}^l \cdot S_{Al,exposed} \quad 4.6$$

The exposed area of the Ni nanoparticle can be written as

$$S_{Ni,exposed} = S_{Ni} - 2\pi r_{Ni} v_{Ni} = 4\pi r_{Ni}^2 - 2\pi r_{Ni} v_{Ni} \quad 4.7$$

where

$$v_{Ni} = r_{Ni}(1 - \cos(\theta)) \quad 4.8$$

Initially during the sintering process the Ni nanoparticle is assumed to remain in the solid phase thus maintaining a constant radius. This assumption is reasonable because of the higher melting temperature of the Ni nanoparticle.

The exposed surface area of the Al nanoparticle is written as

$$S_{Al,exposed} = S_{Al} - 2\pi r_{Al} v_{Al} = 4\pi r_{Al}^2 - 2\pi r_{Al} v_{Al} \quad 4.9$$

where

$$v_{Al} = r_{Al} - \sqrt{r_{Al}^2 - a^2} \quad 4.10$$

$$a = \sqrt{v_{Ni}(2r_{Ni} - v_{Ni})} \quad 4.11$$

The radius of the Al nanoparticle is computed numerically by using conservation of volume for the Al nanoparticle.

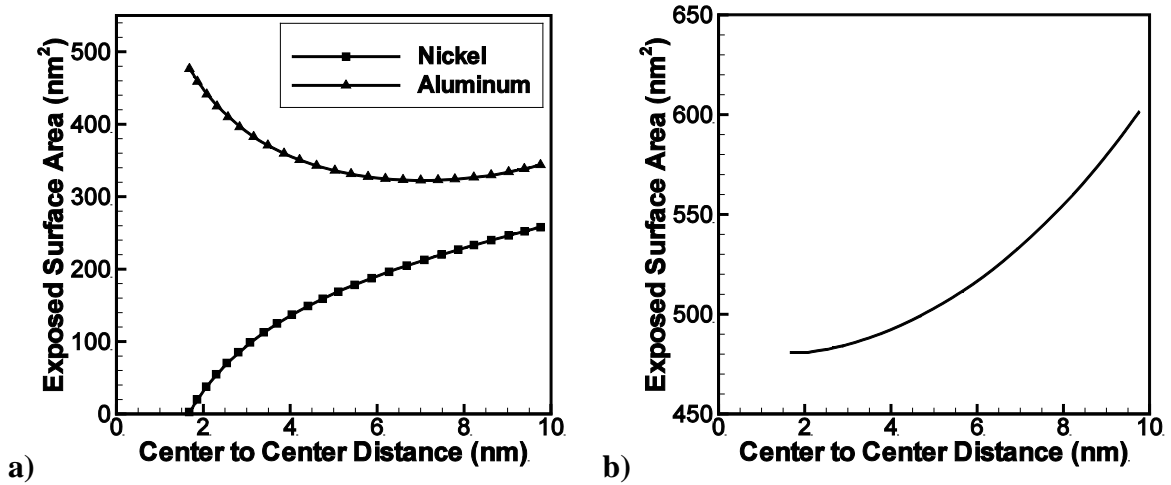


Figure 4.3: a) Plot of exposed Ni and Al nanoparticle surface area as a function of distance between nanoparticle centers. b) Plot of total exposed surface area as a function of distance between nanoparticle centers. These results assume a Ni nanoparticle of radius 4.53 nm and an Al nanoparticle of 5.23 nm. Notice that the total exposed surface area is monotonically decreasing, indicating that the surface energy is also decreasing monotonically

The exposed surface area of each nanoparticle versus the center to center distance is plotted in Figure 4.3a. Notice that although the surface area of the Al nanoparticle increases during most of the coalescence process the combined total surface area of the Ni and Al nanoparticles decreases monotonically throughout the entire coalescence process. In Figure 4.3 the center-to-center distance never reaches zero because the coalescence is considered complete once the Ni nanoparticle is completely enveloped by the Al nanoparticle.

The second source of energy release, namely the reactive synthesis term is considered by assuming a constant surface density of the Ni nanoparticle and the transient contact area of the Ni-Al interface.

$$E_{reactive} = \rho_{Ni,surface} \cdot a_{interface} \cdot V_{bondenergy} \quad 4.12$$

The surface density term, $\rho_{Ni,surface}$, is proportional to the number of Ni-Al bonds at the contact interface. The surface density and bond energy terms, $V_{bondenergy}$, can be combined into a single constant that defines the energy release per unit area of interface.

$$\beta_{density} = \rho_{Ni,surface} \cdot V_{bondenergy} \quad 4.13$$

The interfacial contact area is a function of the distance between nanoparticle centers, Figure 4.4.

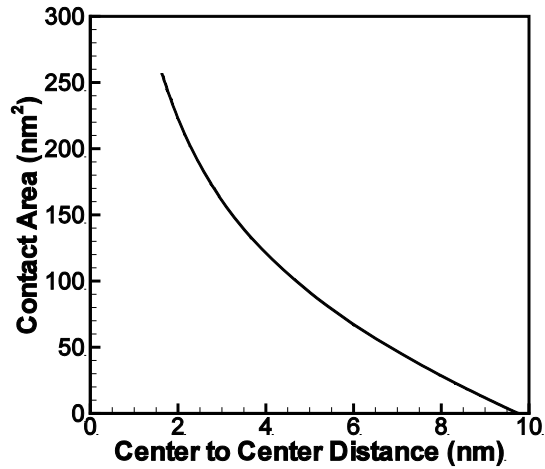


Figure 4.4: Contact or interface area as a function of center-to-center distance. The contact area is increasing as the nanoparticles move closer together (right to left on x-axis).

The interfacial area increases monotonically up until the Ni nanoparticle surface is completely covered. This result is expected since the reactive energy term is negative, or releases energy during the entire process, in addition to the minimization of surface energy that is driven by the surface tension of Ni and Al. The interfacial area is written as

$$a_{interface} = 2\pi v_{Ni} r_{Ni} \quad 4.14$$

where v_{Ni} is a function of θ as given in equation 4.8.

The third energy term represents the viscous dissipation due to deformation of the Al nanoparticle. This viscous dissipation is a function of the viscosity in the liquid Al nanoparticle and the rate of deformation. The extent of the viscous flow can be specified by the decrease in distance between the center of each nanoparticle, and the surface of contact with the Ni nanoparticle. A velocity gradient, γ , can be defined as $(dD/dt)/r_{Al}$. The energy dissipated in the whole body per unit time is therefore approximately

$$\frac{dE_{viscous}}{dt} = 2\eta \int_0^{r_{Al,0}} \gamma^2 (4\pi r^2) dr = \frac{8}{3} \pi r_{Al,0}^3 \eta \left(\frac{dD}{dt} \right)^2 \quad 4.15$$

where η is the viscosity of liquid aluminum and $r_{Al,0}$ is the initial radius of the Al nanoparticle.

By conservation of energy the rate of coalescence can now be computed.

$$\frac{dE_{viscous}}{dt} = \frac{dE_{surf}}{dt} + \frac{dE_{reactive}}{dt} \quad 4.16a$$

$$\frac{8}{3} \pi r_{Al,0}^3 \eta \left(\frac{dD}{dt} \right)^2 = \frac{d}{dt} [\sigma_{Ni}^s \cdot S_{Ni,exposed} + \sigma_{Al}^l \cdot S_{Al,exposed}] + \frac{d}{dt} [2\beta\pi v_{Ni} r_{Ni}] \quad 4.16b$$

After writing equation 4.16b in terms of $d\theta/dt$ and simplifying the right and left hand sides we find that equation 4.16b is only linearly dependent on $d\theta/dt$. Even with this simplification, equation 4.16b, is most easily solved numerically using an iterative solver. In order to solve equation 4.16b we need some physical properties of Al, Ni, and NiAl. The dynamic viscosity of bulk molten Al at the melting temperature is about $\eta = 1.3 \cdot 10^{-3} Pa \cdot s$.¹⁰⁴ Based upon a comparison of the configurational energy in MD simulations of separate nanoparticles and Al-coated Ni nanoparticles the energy

release per unit area, $\beta_{density}$, is estimated to be $20.7 \text{ eV}/\text{nm}^2$. This number is computed by subtracting the system energy of an Al coated Ni nanoparticle system from the energy of a system with separate nanoparticles and dividing by the interfacial surface area. This method results in the net change in energy during coating of the Ni surface with Al since some Al-Al bonds are lost during the coating process while some Ni-Al bonds are formed at the interface. By numerically solving equation 4.16b we are able to compute the contact angle, θ , as a function of time and relate this to total exposed surface area of the coalescing nanoparticles. This model result is presented in Figure 4.5 along with a comparison to the MD simulation results.

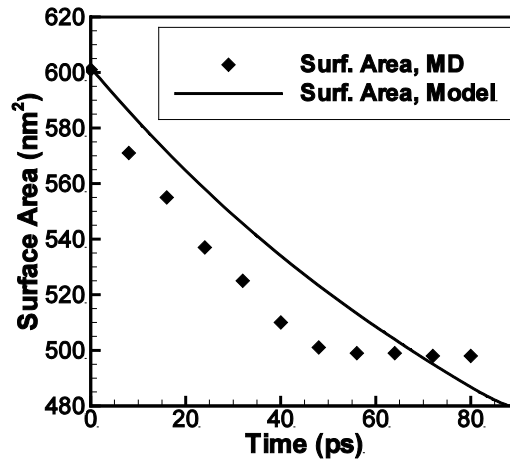


Figure 4.5: Total system surface area versus time from mathematical model and MD simulations for the sintering of 10nm diameter nanoparticles, where the final surface area of the NiAl nanoparticle is approximately 480 nm^2 .

Although qualitatively the results in Figure 4.5 show similar trends the absolute rate of coalescence is slightly under predicted by the model. This difference can be attributed to the obvious simplicity of the model and more specifically to the difficulty in obtaining accurate material parameters. For instance, it is difficult to compare

the viscosity of a nanoparticle to the bulk material⁸⁶ and since the coalescence time is linearly dependent upon the viscosity the modeled coalescence time is directly proportional to the assumed viscosity. Additionally, the energy release per unit area term assumes that the net change in energy due to the addition of Ni-Al bonds at the interface is a constant value. This is likely not completely accurate since fewer Al bonds must be broken to form new Ni-Al bonds during the initial contact of the nanoparticles. However, the deviation in this energy release term is likely to be minimal. The deviation of the model time from the simulation results at about 50 ps is due to the switch from stage 1 to stage 2 in the coalescence. As described by Lewis et al,⁵² during stage 2 or 50ps after contact, surface diffusion is the predominant factor in continued coalescence and is a much slower process than contact area maximization. The actual simulation results, as compared with the illustration in Figure 4.1, of the observed coalescence process are given in Figure 4.6.

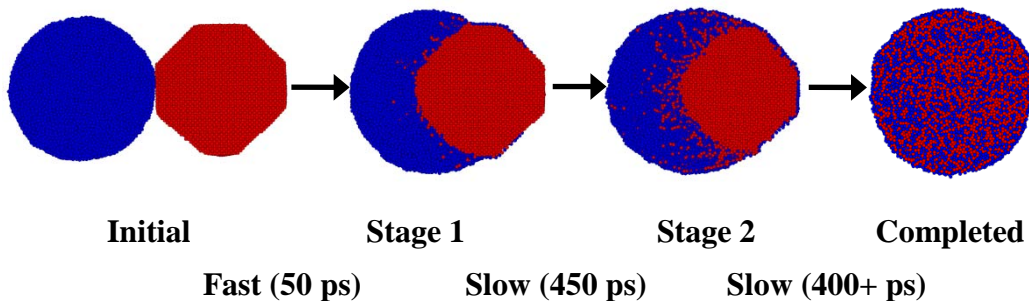


Figure 4.6: Cross sectional view from MD simulations of Ni/Al nanoparticle sintering process showing the start of the second stage of coalescence where diffusion is the driving force as opposed to contact area maximization. Aluminum atoms are blue and nickel atoms are red.

In Figure 4.6 each of the steps in the coalescence process are shown with plots from an MD simulation of the coalescence of 10nm diameter Al and Ni nanoparticles.

The correlation of the sintering stages to the reaction temperature and time is illustrated in Figure 4.7 for the sintering of separate 10nm diameter nanoparticles. In the initial step the liquid Al nanoparticle, blue atoms in Figure 4.6, has melted and is spherical in shape. The solid Ni nanoparticle, red atoms, has large faceted sides and is a single crystal, a typical configuration for a crystalline nanoparticle at low temperatures. During stage 1 the Al nanoparticle is attracted to the Ni surface because of the dual driving forces of surface energy minimization and Ni-Al bond formation. This period lasts about 50 ps in this simulation as noted in Figure 4.6 and Figure 4.7. Between stages 1 and 2 the driving forces associated with the surface energy are counteracted by a resistance to flow in the Al nanoparticle, causing the coalescence process to slow down dramatically. During stage 2, lasting about 450 ps, the surface area is not changing perceptively so that energy release from the surface energy terms has ceased to contribute to the change in system potential energy. The subsequent energy release is entirely attributable to the formation of Ni-Al bonds. This stage lasts a much longer time than the initial nanoparticle coalescence stage and is governed by the material diffusion coefficients. Initially at stage 2 the Ni nanoparticle is still solid and the formation of Ni-Al bonds is only possible by Al diffusing into the Ni core or Ni on the surface of the core melting and diffusing away from the interface. This process proceeds until the Ni core has reached its melting point and mixing of the remaining Ni and Al atoms occurs more rapidly, driven by the enthalpy of formation of NiAl. Following stage 2 until complete alloying has occurred, taking approximately 400 ps, diffusion and mixing of Ni and Al atoms is the primary driving force.

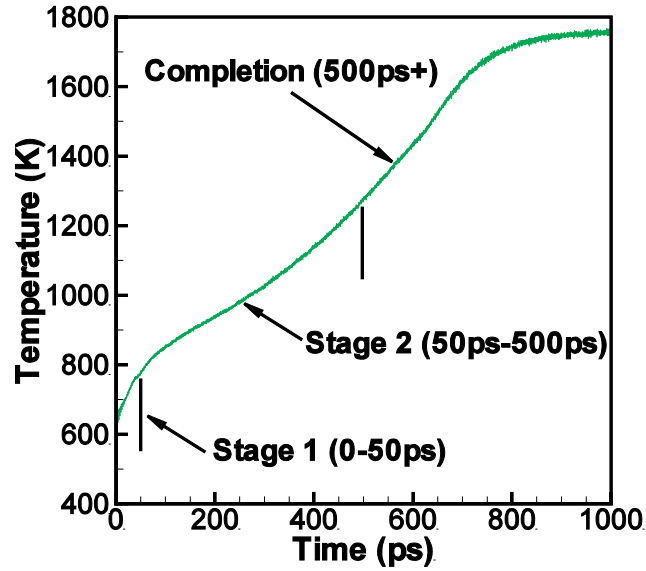


Figure 4.7: Time versus temperature plot for sintering of separate 10nm diameter Al and Ni nanoparticles. The various stages of the coalescence processes are denoted on the curve, including the final completion stage that occurs after the Ni nanoparticle has melted.

4.6 MD Simulation Results of Separate Nanoparticle Reactivity

We have previously predicted the adiabatic temperature and sintering time for the reactive sintering process of separate equimolar nanoparticles of Al and Ni. In Figure 4.8, the MD simulation results for the equimolar nanoparticles are plotted along with the computed adiabatic temperature for each considered particle size.

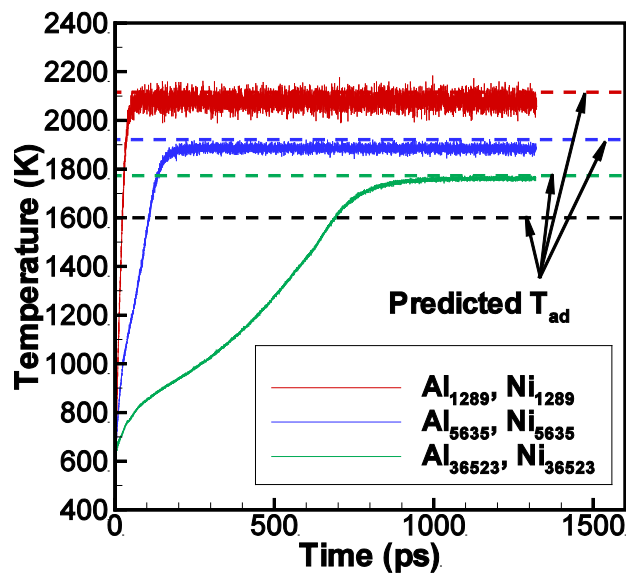


Figure 4.8: Temperature versus time in the sintering of nanoparticles with an Ni:Al ratio of 1:1. The subscripts in the legend refer to the number of atoms of each material and correspond to nanoparticles of diameter approximately 3nm, 5nm, and 10nm. The color coded dashed lines are the computed adiabatic temperature from the thermodynamic analysis. The black dashed line is the predicted temperature for coalescence of bulk Al and Ni.

From Figure 4.8, it is apparent that the predicted adiabatic temperature is in close agreement with the simulated temperature. Variability of the computed temperature likely arises from the wide range of experimental results for the surface tension for liquid Al and solid Ni, the reported enthalpy of formation for NiAl, and the assumed melting temperature for the Ni and NiAl materials at this scale. Each of these experimental data points are used in the thermodynamic analysis and contribute to the small inaccuracies in the predicted temperature.

The reaction time can be evaluated from the characteristic time for reactive synthesis defined by Zhao et al¹⁰⁵ as t when

$$T(t) = T_0 + 0.8(T_1 - T_0) \tag{4.17}$$

where T_0 is the initial temperature, T_1 is the maximum size dependent temperature reached, and $T(t)$ is the transient temperature. The computed reaction times are given in Figure 4.9 and illustrate that the time required for separate nanoparticles to react has a power law relationship that is between nanoparticle volume (radius to power of 3), and surface area (radius to power of 2). This implies that not only will the reaction temperature be higher, but will occur more rapidly with decreases in particle size, to a combined power of about 2.5. This is important because a high rate of energy release is desirable for many applications.

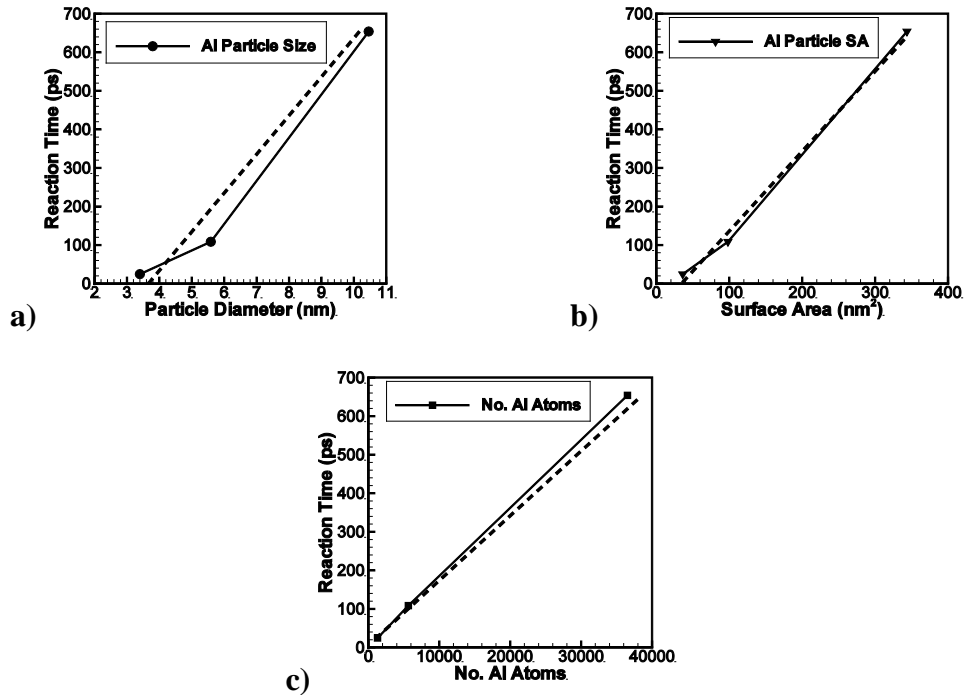


Figure 4.9: Reaction time versus Al nanoparticle diameter (a), Al nanoparticle surface area (b), and number of Al atoms (c). Note the nearly linear relationship (dashed line) of reaction time between number of atoms (volume) and surface area.

By observing the MD simulation results and analyzing the shape of the curves in Figure 4.8 for temperature versus time we have surmised that there are two reaction rates to consider. The first is during the coalescence process (called the growth rate (see 0 to 500 ps for Al_{36523} curve in Figure 4.8)) and Ni nanoparticle melting, and the second is the rapid formation of the NiAl alloy from mixing of liquid Al and Ni (convergence rate (see 500 ps and later for the Al_{36523} curve in Figure 4.8)). The temperature at which the transition between the two reaction rates occurs is size dependent because the melting temperature of the Ni nanoparticle is also size dependent. If the reaction is not perfectly adiabatic, and some heat is lost to the surroundings it is also possible that the first process would not precede far enough for the Ni nanoparticle to melt and thus the reaction would halt. This would only occur with larger nanoparticles that require longer reaction times during which some energy loss to the surroundings is likely. This is an important consideration in real world applications that are not perfectly adiabatic, but when complete alloying is desired. One reason for this observed increase in reaction rate is because the heat generated from the formation of Ni-Al bonds will conduct into the core nanoparticle so that when the reaction front reaches the inner atoms they will have a higher diffusion coefficient, which in turn increases the reaction rate.

4.6.1 Analysis of Alloy Formation

During the sintering of Ni and Al nanoparticles numerous mixtures may be formed from the Ni-Al binary system.^{100,102,103} The most common compounds observed include Al_3Ni , Al_3Ni_2 , NiAl, Ni_5Al_3 , and Ni_3Al corresponding to Ni fractions of 0.25, 0.40, 0.50, 0.625, and 0.75, respectively. A comprehensive analysis of the compounds

formed during sintering of separate nanoparticles is summarized here. Figure 4.10a and b show the normalized amount of each compound by Ni fraction through stage 2 and during stage 3, respectively. The atomic fraction of surrounding atoms are calculated within a radius of 4.0\AA .

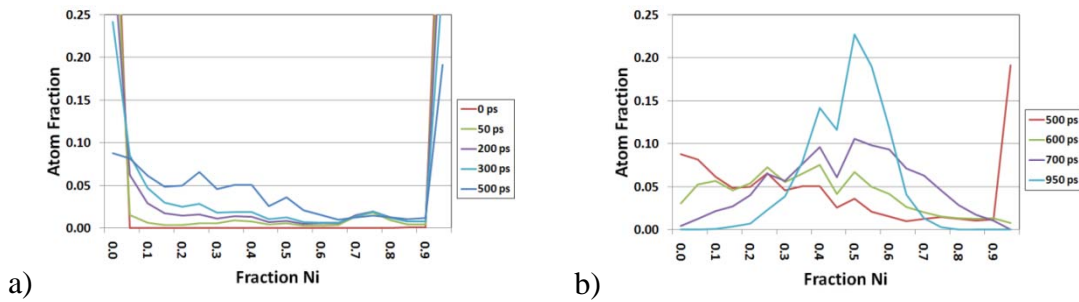


Figure 4.10: Fraction of all atoms in each compound versus fraction of Ni in compound. i.e. a data point at (0.1, 0.25) corresponds to 10% of all atoms in the system belong to the Al_3Ni compound.

During stage 1, from 0 ps to 50 ps for sintering of 10nm diameter particles, most of the atoms remain in the pure metal phase, with only a small fraction forming some Ni rich alloys such as Ni_3Al . This initial peak at about 50ps is likely due to the shorter bond length of Ni-Ni so that near the contact interface each Al atom will bond with multiple Ni atoms. During stage 2, the formation of Al rich alloys occurs at a rapid rate, quickly depleting the amount of pure Al by the end of stage 2 (500 ps). In Figure 4.10a, at 500 ps, a small peak between 0.2 and 0.3 Ni fraction is observed, corresponding to Al_3Ni . The largest fraction of any compound at 500ps is still pure Ni. The initial formation of Al rich alloys is supported by experimental observations.^{100,103}

The reaction process that produces these Al rich alloys is explained by Al atoms moving into the pure Ni region forming regions of Al_3Ni which then separate from the interface and dissolve into the Al phase eventually forming the eutectic mixture. Fig-

Figure 4.11b supports this process because small clusters of Al rich alloys that contain Ni neighbors are clearly evident in the liquid Al.

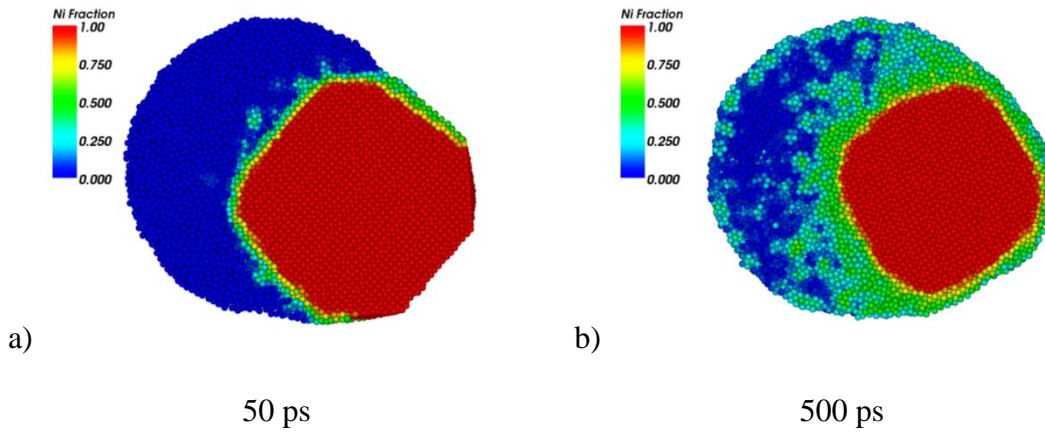


Figure 4.11: Plot showing spatial distribution of Ni fractions during stages 1 and 2 of the sintering process.

The lines in Figure 4.10b for stage 3 indicate a rapid reduction in the amount of pure Ni and the corresponding formation of NiAl. During stages 1 and 2 as observed in Figure 4.8 the temperature of the system is rising monotonically. Subsequently, near the start of stage 3 the system temperature has reached the melting point of Ni. At 700 ps, shortly after the Ni nanoparticle has completely melted, two peaks are present in Figure 4.10b, near 40% Ni and 50% Ni, corresponding to Al_3Ni_2 and NiAl. Near completion of the energetic reaction, at 950 ps, the majority of atoms are in the NiAl eutectic mixture with some temporary formation of other alloys.

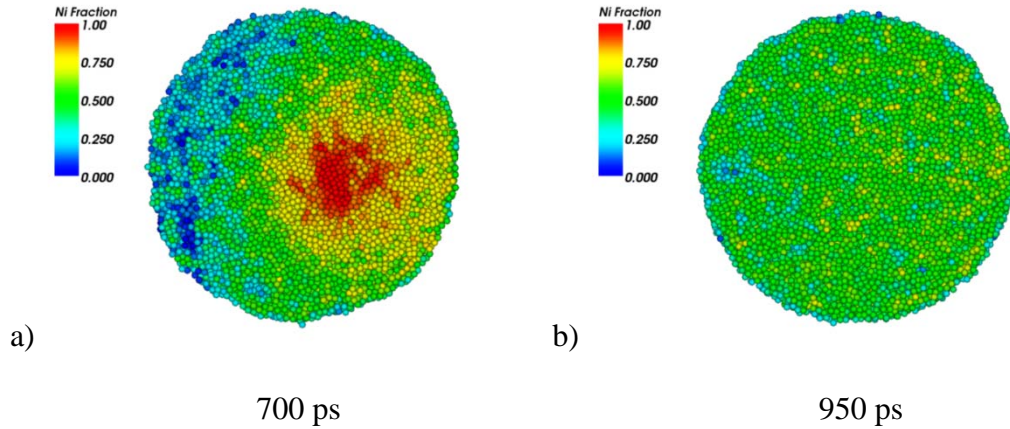


Figure 4.12: Plot showing spatial distribution of Ni fractions during stage 3 of the sintering process.

Near the beginning of stage 3 and just prior to the profile in Figure 4.12a is observed the system temperature has reached the melting point of Ni. In Figure 4.12a, shortly after melting of the Ni nanoparticle, there is a Ni rich region visible. This region rapidly disappears as the SHS reaction proceeds rapidly to form the final eutectic alloy.

4.7 Reactive Sintering of Core-Shell Nanoparticles

4.7.1 Aluminum Coated Nickel

In this section we will discuss the sintering process for an Al-coated Ni nanoparticle followed by a discussion of a Ni-coated Al nanoparticle. Both of these systems can be used as a model for highly compacted Ni and Al nanoparticles or one material serving as a matrix for nanoparticles of the other. In the first model system we assume that a Ni nanoparticle has been coated with Al and equilibrated without the Ni melting, or any further reaction occurring. Results for the reaction time and temperature will be presented and a comparison with the separate nanoparticle case will be given. Here

again we have considered three system sizes with 1289, 5635, and 36523 atoms each of Al and Ni.

An initial estimate is that the coalescence process for the fully coated nanoparticle system will be a truncated version of the separate nanoparticle case. In the coated nanoparticle system we do not have the first stage of coalescence occurring and only observe the second and third stages, namely diffusion of Ni and Al atoms to form Ni-Al bonds. The sintering temperature versus time plot is given in Figure 4.13 and shows an interesting result. Whereas the maximum temperature reached increases with decreasing nanoparticle size for coalescence of separate nanoparticles, the opposite is true here, the temperature decreases with decreasing nanoparticle size.

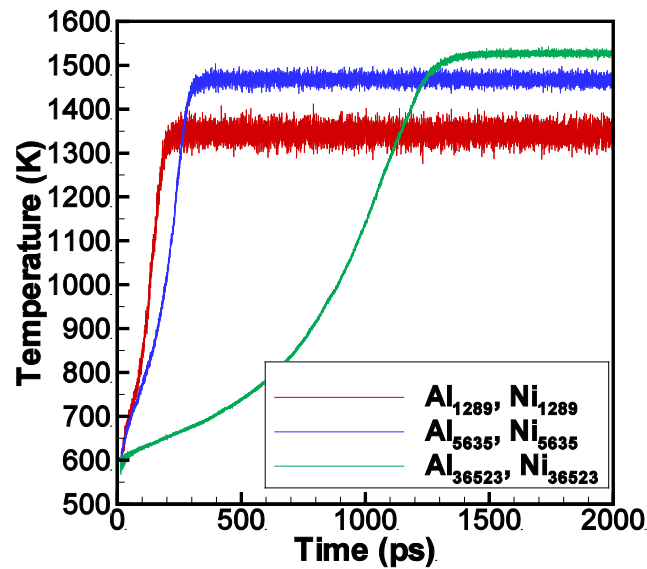


Figure 4.13: Temperature versus time in the sintering of Al-coated Ni nanoparticles with an Ni:Al ratio of 1:1.

In Figure 4.13 the observed decrease in adiabatic temperature is due to the fact that the ratio of atoms near the interfacial region to the atoms in the bulk nanoparticle decreases as the nanoparticle size increases. Atoms in the interfacial region have al-

ready formed Ni-Al bonds and are therefore already at a lower configurational energy than if they were contained in a homogeneous nanoparticle of either pure Al or Ni. If we extend the adiabatic temperature relationship to infinitely large particles we would approach the result obtained from the analysis of separate nanoparticle as they increase in size. The thermodynamic analysis for this case is similar to the previous one except that the surface energy term is zero and the enthalpy of formation is lowered by a factor proportional to the ratio of surface area to volume. The enthalpy of the products, equation 4.5, modified for coated nanoparticles becomes

$$H_{prod} = \left(1 - \frac{t \cdot A_{surface}}{V}\right) H_{form, NiAl} + \int_{298K}^{T_{ad}} C_{p, NiAl}(T) dT + H_{melt, Ni} \quad 4.18$$

In equation 4.18 t is a computed thickness value for the interfacial layer, $A_{surface}$ is the area of the interfacial region, and V is the volume of the Ni core. In order to determine the correct empirical thickness value, t , for equation 4.18 we have used the adiabatic temperature computed in the MD simulation results for the Al-coated Ni nanoparticle. These results indicate that an interface thickness of 0.07nm is able to accurately predict the adiabatic temperature observed in the MD simulations, Figure 4.14.

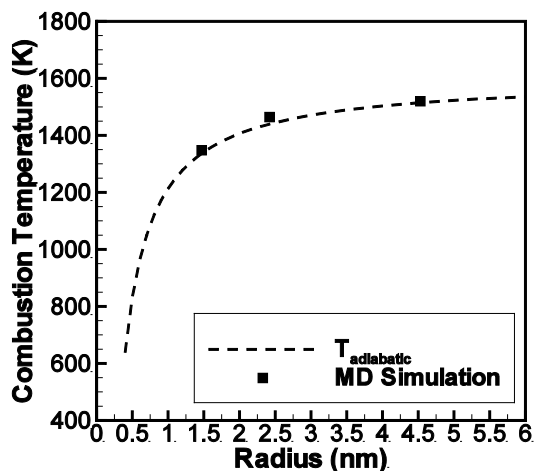


Figure 4.14: Comparison of thermodynamically determined adiabatic temperature for Al-coated Ni nanoparticle and results from MD simulation.

In Figure 4.14 it is apparent that the adiabatic combustion temperature is highly size dependent for nanoparticles of less than 10nm in diameter. For very small nanoparticles, less than 1nm diameter, there is little predicted change in temperature from the initial temperature of 600K since most of the potential Ni-Al bonds have already been formed.

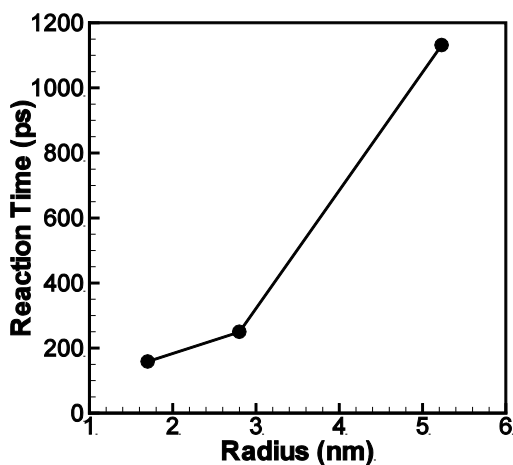


Figure 4.15: Reaction time versus number of Al atoms in the Al-coated Ni nanoparticle system.

The results for the Al-coated Ni nanoparticle indicate the trends that one might expect from a material system that includes an Al matrix with embedded Ni nanoparticles. From the results in Figure 4.14 and 4.15 there are two competing reaction results, namely reaction time and maximum temperature. In Figure 4.15 we see that as the Ni nanoparticle size decreases the reaction time decreases, causing the energy release rate to increase. A second observation that can be made from Figure 4.14 is that the reaction temperature decreases with decreasing Ni nanoparticle size, potentially minimizing the effect of the rapid energy release.

Looking more closely at the reaction time versus number of atoms for the separate nanoparticle and Al-coated Ni nanoparticle cases we observe a similar relationship of reaction time to nanoparticle size as that found in separate nanoparticles. In both cases the reaction time appears to have a power law relationship with radius, with an exponent of 2.5. The accelerated temperature increase in Figure 4.13 after about 900ps for the Al_{36523} curve is the convergence rate discussed previously.

4.7.2 Nickel Coated Aluminum

The Ni-coated Al nanoparticle system has garnered some interest because when Al melts there is an experimentally observed increase in volume of about 12%. This increase in volume creates a large stress in the Ni coating and may result in catastrophic failure and fragmentation of the nanoparticle.⁹¹ In the work by Delogu,⁹¹ the fragmentation is only observed for a specific set of conditions including Ni shell thickness. In this work, even with the appropriate Ni shell thickness, fragmentation of the nanoparticle is not observed. With the empirical potentials and parameters considered here

the SHS reaction is fast and results in a liquid NiAl nanoparticle without fragmentation.

In the first set of analyses the Ni shell contains the same number of atoms as the Al core. This results in an Al core with a radius of 2.8 nm and a Ni shell of about 0.7 nm. Since the bond length of Ni is less than Al the shell is thinner and the contact area is initially greater than observed in similarly sized Al-coated Ni nanoparticles. As with the nanoparticle coalescence simulations, the temperature of the system is raised to 600K at which time a constant energy simulation is used to analyze the energy conversion rate and the adiabatic temperature rise of the system.

In the initial simulations with an atomic ratio of unity there are more Ni-Al bonds in the Ni-coated nanoparticle than the Al-coated nanoparticle. It may therefore be expected that the total system energy would initially be lower in the Ni-coated Al nanoparticle system than the Al-coated Ni system. In fact, the opposite is true, because although there are more Ni-Al bonds in the Ni-coated system there are fewer Ni-Ni bonds than in the Al-coated nanoparticle. Since Ni-Ni bonds are stronger than Al-Al bonds the total initial energy is lower in the Al-coated Ni nanoparticle system. Since the final configuration of both systems is a completely alloyed NiAl nanoparticle, the system energy change for the Ni-coated nanoparticle is greater than the Al-coated system. This greater change in potential energy, results in the computed adiabatic temperature for the Ni-coated Al nanoparticle being higher than the Al-coated nanoparticle, Figure 4.16, although the difference is not large.

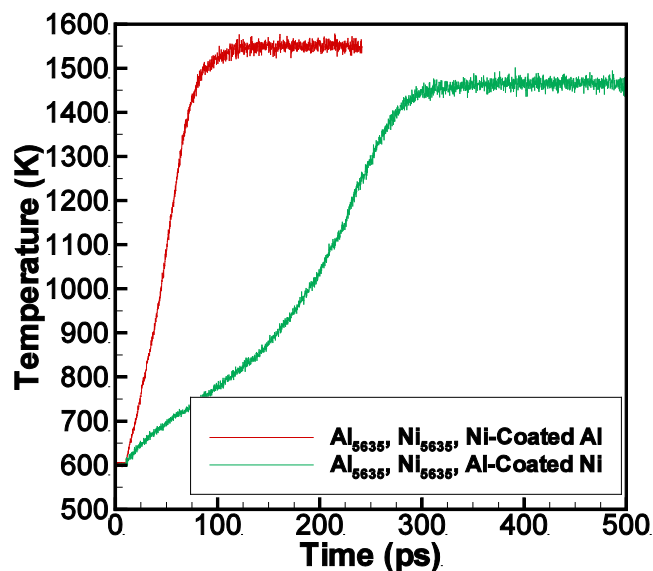


Figure 4.16: Comparison of combustion temperature for Ni-coated Al nanoparticle versus Al-coated Ni nanoparticle.

In the two following simulations we simulated an approximately 5nm diameter Al nanoparticle coated with either a 1 nm or a 2 nm thick Ni coating. For these simulations the temperature was controlled using an NVT ensemble. This temperature control was used in order to rapidly increase the temperature from about 300K to above the melting point of the Al nanoparticle, at a rate of 0.1 K/ps. When the Al nanoparticle melts and expands, a large sudden increase of stress in the Ni coating is expected. For the 2nm thick Ni coating the increase in stress is not high enough to cause failure of the coating. In this case the outer shell expands slightly but does not crack. For the 1nm thick case the stress in the Ni shell is high enough to cause failure. When the shell fails the Al begins to leak out onto the surface of the nanoparticle but no fragmentation is observed. If the nanoparticle were surrounded by oxygen this may initiate the Al oxidation reaction, releasing additional energy as Al oxides are formed.

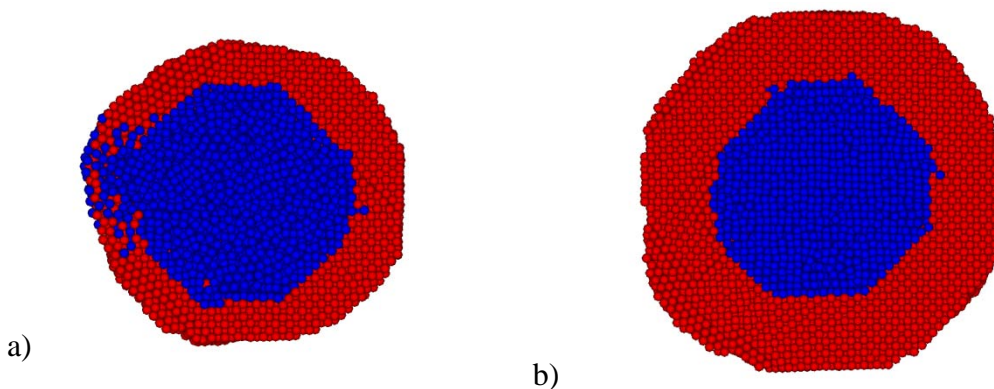


Figure 4.17: Cross sections of the Ni-coated Al nanoparticle simulation model just after melting of the Al core for the 1nm (a) and 2nm (b) thick Ni shells.

The cracking and leaking of Al onto the surface of the Ni shell is very different from the fragmentation observed in Delogu⁹¹ observed using a semi-empirical tight-binding (TB) potential. Another difference from the work by Delogu is the choice of Al core radius. For both of the shell cases here the core has a radius of 2.8nm, this is in comparison to the core radii of 3.0nm and 2.0nm for the 1.0 nm and 2.0 nm shell cases, respectively used by Delogu.⁹¹ Since the 1nm shell case is the most interesting and the radii are very close (2.8nm vs. 3.0nm) the choice of core size is not expected to have had an appreciable effect on the results for this case.

4.8 Conclusions

We have analyzed two model systems for the energetic reaction of Ni and Al. In the first case we considered the coalescence and sintering of separate nanoparticles and found that the energy release from the change in surface area is only significant at small, less than 10 nm diameter, nanoparticles. These separated nanoparticle reaction simulations and thermodynamic analyses show that the reaction time will decrease and the adiabatic reaction temperature will increase with decreasing nanoparticle siz-

es. This may be important for applications where high energy release rates are desired. The simulation data closely match a classical thermodynamic analysis.

In the second part of this work we considered the sintering of Al-coated Ni nanoparticles and Ni-coated Al nanoparticles as a model material system for nanoparticles embedded in a matrix of the other metal. This work revealed that the reaction time is again inversely related to nanoparticle size but the adiabatic temperature decreases with decreasing nanoparticle size. Mechanically the Al-coated Ni nanoparticle system is a model system for a light weight Al matrix with embedded Ni nanoparticles, a system with relatively high strength compared to a loosely bonded powder of Al and Ni nanoparticles. This Al matrix system could be used in systems where mechanical strength is important in addition to energy release from energetic sintering of the Ni and Al atoms. In the Ni-coated Al nanoparticle system we investigated possible rupture and fragmentation of the Ni shell but were unable to observe any fragmentation.

5 On the Role of Built-in Electric Fields on Oxidation of Oxide Coated NanoAluminum: ion mobility versus Fickian Diffusion

5.1 Introduction

Much of the interest in nanoparticles is derived from an appreciation that chemical/physical properties often vary from that of the bulk material. For instance it is known that catalytic activity can be significantly changed from that of the corresponding bulk.^{106,107} It is also well known that metal nanoparticles are pyrophoric and have enhanced energy release rates, which make them attractive in propulsion.⁷⁸

Virtually all metal nanoparticles will nominally have a native oxide shell, which for aluminum is ~ 2-3 nm thick. Thus any oxidative reaction or vigorous combustion must proceed by transport of either the aluminum or oxidizer through the oxide shell. The oxidation reaction of oxide coated aluminum nanoparticles has been observed to occur at a lower temperature and a faster rate than micron sized particles, suggesting to some a different oxidation mechanism than observed in larger particles. In fact, nanoparticles have been experimentally shown to react at or near the melting point of bulk aluminum, 933K,⁷⁸ whereas larger particles react closer to the melting point of the oxide shell, namely 2327K. The closeness of the reaction temperature to the melting point of pure aluminum indicates that the melting of the aluminum core is the possible initiator of this reaction for nanoparticles.

It has previously been assumed that either the sudden decrease in density of the aluminum upon melting^{108,109} or the lower melting temperature of the nanometer

sized oxide shell¹¹⁰ is the key to initiation of the oxidation process. However, in this chapter we explore the possibility that built-in electric fields as opposed to Fickian diffusion drive aluminum cations through the oxide shell to the nanoparticle surface where it is possible for the oxidation process to proceed. Experimentally produced hollow aluminum oxide nanoparticles provide support for this rapid diffusion hypothesis.^{111,112} These observed hollow oxide shells are an indication that the oxidation process is driven by the diffusion of aluminum cations. We will show that field mediated ion-transport is much faster than Fickian diffusion, and will be the dominant transport process in the oxidation of nanoaluminum. Anecdotal support for this mechanism comes from numerous numerical^{113,114} and experimental studies.^{115,116}

5.2 Simulation Approach

In this work we have chosen to use the ReaxFF (Reactive Force Field) empirical potential from van Duin¹¹⁷ implemented within the GRASP (General Reactive Atomistic Simulation Program) MD application. The ReaxFF potential has an advantage over traditional empirical potentials in that it is able to accurately simulate the charge transfer that occurs during metal oxidation. The other empirical potential commonly used for this material system is the Streitz-Mintmire potential,¹¹⁸ however we chose to use the ReaxFF potential because it is available within GRASP which can be executed in parallel. The Al-O potential parameter set used in this work comes from a previous effort that considered the sliding of Al₂O₃ coatings against Al and Al₂O₃.⁴² The computational requirement of this software is high with the largest material system considered here containing nearly 100,000 atoms and is efficiently simulated with 96 Intel Woodcrest processor cores running at 3.0 GHz.

5.3 Model Description

Two core sizes are considered here, the smaller of these consists of a 5.6nm diameter core of aluminum with either a 1nm or 2nm thick shell of Alumina (Al_2O_3) as illustrated by the example systems in Figure 5.1. The second and larger model includes an 8nm aluminum core with a 2nm thick crystalline oxide shell. This model is used to consider scaling effects for the electric field and atomic diffusivity.

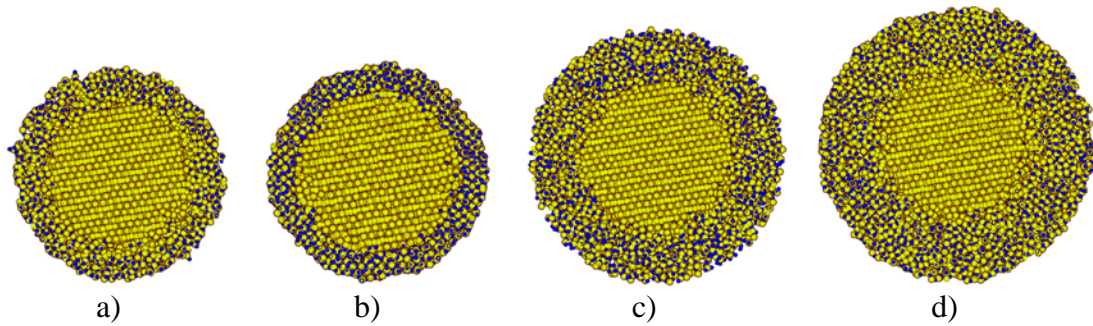


Figure 5.1: Cross sections of some of the oxide coated aluminum nanoparticle models used in this work. a) 1nm thick, dense oxide shell. b) 1nm thick, crystalline oxide shell. c) 2nm thick, amorphous oxide shell. d) 2nm thick, dense oxide shell with 2:2.7 Al:O ratio. Blue spheres represent oxygen atoms and yellow spheres denote aluminum atoms.

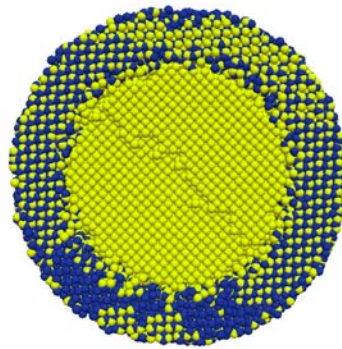


Figure 5.2: Cross section of an 8.2nm Al core with 2nm thick crystalline oxide shell. Yellow denotes Al atoms and oxygen atoms are blue.

There are four shell configurations considered for each oxide shell thickness.

1. A defect free crystalline shell that may result from extremely slow or high temperature formation. This shell is modeled by coating a bare aluminum nanoparticle with a crystalline shell made up of α -Al₂O₃. The alpha form is used as a representative crystalline shell configuration.
2. A dense amorphous shell that has an atomic ratio of 2:3 aluminum to oxygen atoms (i.e. Al₂O₃). This shell is formed in the simulation by heating a crystalline oxide shell above its melting temperature while holding the aluminum core atom positions fixed. In this way the oxide layer melts and is subsequently cooled rapidly and trimmed in order to obtain a slightly amorphous oxide layer with the desired thickness.
3. A dense amorphous shell 10% deficient in oxygen atoms, Al/O = 2:2.7. This shell may form during a faster rate of formation or if the environment during formation was oxygen lean. In the computer simulation this shell is formed by removing 10% of the oxygen from the previous dense oxide shell that is at the stoichiometric ratio of 2:3 aluminum to oxygen atoms.
4. Lastly, a porous amorphous shell with an atomic ratio of 2:3 aluminum to oxygen atoms. This shell has approximately one half of the density of the previously described dense shell with the same atomic ratio. This more porous amorphous shell represents oxide formation that may occur at a very fast rate with a sufficient supply of oxygen. This oxide shell is formed in the computer simulation similarly to the process used for the dense shell except that the shell is repeatedly heated to a high temperature and rapidly cooled until a much more amorphous configuration is achieved.

Following the creation and equilibration of the oxide shell, the model systems were heated at rates of 10^{11} K/s, 10^{12} K/s, and 10^{13} K/s in order to determine any rate dependencies. We found, similarly to Puri and Yang,¹¹⁰ that at rates below 10^{12} K/s the heating rate appears to have little effect on the simulation results. This is an important result, as lower heating rates would increase the number of MD simulation time steps, which for this work was ~ 1 fs to maintain energy conservation, to a level that would be unreasonable with current computing capacities. The temperature of the model systems was raised from 300K to 1000K and eventually up to 3000K, which is much higher than the melting point of the oxide layer. From experimental data available in the literature⁷⁸ it is expected that some reaction should be observed near the melting point of the aluminum core. At the melting point of the core the aluminum density decreases from, 2.7g/cm^3 to 2.4g/cm^3 , resulting in a volumetric expansion of about 12%. Melting of the oxide shell requires heating the nanoparticle to above the melting point of the oxide which is 2327K for the bulk material or somewhat less for a nanoparticle shell because of the size affect. The results of each of these efforts are detailed in the following sections.

5.4 Results of Rapid Heating Simulations

The simulations in this section were carried out in a vacuum so that as Al cations move radially outward towards the oxide surface there are no oxygen molecules available for oxidation reactions. In simulations discussed later we have found the diffusivity of Al through the oxide layer to be more important than oxygen diffusion towards the core. For this reason we are primarily concerned in this work with the

mechanism by which Al cations reach the surface of the nanoparticle. Initially, the nanoparticles were heated from 300K to about 1000K, which is above the core melting point but below the size dependent oxide melting point reported by Puri and Yang.¹¹⁰ At around 900K, or slightly below the bulk melting temperature of the aluminum core, a rapid volumetric expansion of the core is observed indicating that the aluminum core has begun to melt. At 1000K the oxide shell still remains intact, with no cracking, even when maintained at that temperature for 100ps. We do see however, as illustrated in Figure 5.3, the initiation of aluminum cation diffusion to the particle surface.

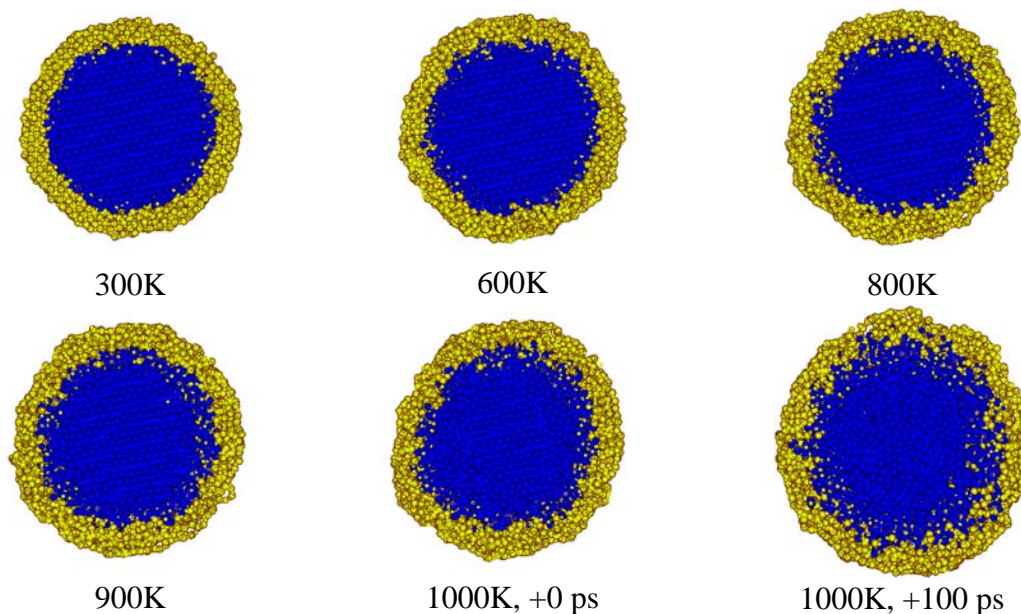


Figure 5.3: Plot showing diffusion of aluminum cations (blue) through the 1nm thick oxide shell (red) as the temperature increases from 300K to 1000K and held for 100 ps.

The results in Figure 5.3 show a slightly inhomogeneous melting of the aluminum core, which is evident in the “1000K, +0ps” plot. Some of the less dense faces of the core begin to melt while the top and bottom remain crystalline, giving the nanoparticle a slightly elongated appearance. The plots in Figure 5.3 also show the me-

chanism by which oxidation will proceed at elevated temperatures. The first observation is that the oxide shell does not crack as one might expect, if diffusion were extremely limited, or the shell were brittle. This suggests that the shell is more elastic at this scale, or the expansion of the aluminum is insufficient to cause failure in the shell, even at these elevated temperatures. One possible reason for the enhanced elasticity is the lower coordination of the atoms in the oxide shell as compared to the bulk material,¹¹⁹ which is incidentally also a contributing factor to the size dependent melting temperature observed in nanoparticles. In addition, we observe significant diffusion of the core atoms through the oxide shell, thus relieving the potentially high internal pressures. The primary mechanism driving this diffusion is discussed in the following sections.

5.5 Aluminum Cation Diffusion through the Oxide Shell

As observed by us and by others,¹¹⁰ at temperatures below the melting point of the oxide shell there is significant diffusion of aluminum cations through the oxide shell. Computation of the diffusivity from the mean square displacement (MSD) of the aluminum cations yields values typically found for liquids. This was unexpected because these measurements were taken at 600K, somewhat below the melting temperature of the relatively small 5.6nm aluminum nanoparticle core. Although the MSD data is somewhat noisy because of the limited simulation time and small nanoparticle sizes, there is an obvious trend of proportionally increasing diffusion rates radially through the shell with increased temperature. To support this observation the effective radial diffusivity is compared to the overall effective diffusivity in table 5.1.

Table 5.1: Effective diffusion coefficients for core aluminum atoms with various oxide shell configurations. The effective diffusion coefficients are for general diffusion (D_{eff}) and radial diffusion (D_{radial}).

Shell Thickness	Type	Temperature	D_{eff} ($\text{cm}^2/\text{s} * 10^{-7}$)	D_{radial} ($\text{cm}^2/\text{s} * 10^{-7}$)
1nm	Amorphous	600K	53	5.9
1nm	Amorphous	1000K	420	300
1nm	Amorphous	2000K	7100	8300
1nm	Dense	600K	11	4.0
1nm	Dense	1000K	340	280
1nm	Dense	2000K	1300	1300
1nm	Dense, $\text{Al}_2\text{O}_{2.7}$	600K	2.6	2.1
1nm	Dense, $\text{Al}_2\text{O}_{2.7}$	1000K	380	190
1nm	Dense, $\text{Al}_2\text{O}_{2.7}$	2000K	6000	6700
1nm	Crystalline	600K	31	6.7
1nm	Crystalline	1000K	330	240
1nm	Crystalline	2000K	1000	1300
2nm	Amorphous	600K	23	4.6
2nm	Amorphous	1000K	400	320
2nm	Amorphous	2000K	770	660
2nm	Dense	600K	8.1	6.9
2nm	Dense	1000K	360	250
2nm	Dense	2000K	490	520
2nm	Dense, $\text{Al}_2\text{O}_{2.7}$	600K	4.2	3.3
2nm	Dense, $\text{Al}_2\text{O}_{2.7}$	1000K	370	180
2nm	Dense, $\text{Al}_2\text{O}_{2.7}$	2000K	270	100
2nm	Crystalline	600K	8.3	7.8
2nm	Crystalline	1000K	330	190
2nm	Crystalline	2000K	490	520
2nm, 8nm Core	Crystalline	600K	6.9	9.9
2nm, 8nm Core	Crystalline	1000K	190	160
2nm, 8nm Core	Crystalline	2000K	1300	920

The diffusion coefficients in Table 5.1 are computed using equation 5.1.

$$\frac{\partial \langle r^2(t) \rangle}{\partial t} = 2dD \quad 5.1$$

In equation 1, the number of dimensions, d , available for atomic diffusion, is 3 for overall diffusion, and 1 for radial diffusion.¹²⁰ The use of the bulk diffusion equation is reasonable since during the time scales considered the movement of only the atoms

initially on the surface are restricted by the particle boundary.¹²¹ For radial diffusion we are only concerned with the MSD directed radially from the center of the nanoparticle. In equation 5.1, t is the elapsed time, and $\langle r^2(t) \rangle$ is the MSD of the atoms being tracked. The diffusion coefficients reported are for all of the core atoms including those near the center of the nanoparticle. This is important since we would expect the mechanical and electrostatic effects to be larger near the core/shell interface, but because of the small sample sizes available, computing a radial distribution of diffusivity is unreliable.

By comparing the radial and overall diffusivities in Table 5.1 an interesting trend is observed. As the temperature increases the radial diffusivity becomes a generally more important portion of the overall diffusivity of aluminum cations. This result indicates that once the aluminum core has melted the diffusion of aluminum cations is preferentially in the radial direction, as compared to the results prior to melting. This is possibly due to a high pressure gradient near the core/shell interface. Another possibility is that once the core has melted the atoms are more mobile so in addition to pressure, any other effects such as an electric field will increase diffusion. The radial diffusion data that does not correlate with this observation at 600K is for the 2nm thick crystalline oxide shells for both the 5.6nm and 8.2nm aluminum cores. These configurations show diffusion rates that are on par with the overall diffusivity, possibly indicating that one of the drivers of radial diffusion is proportionally stronger for these shell configurations at 600K. We will show in the following sections that the electric field is indeed strongest in the 2nm thick crystalline shells.

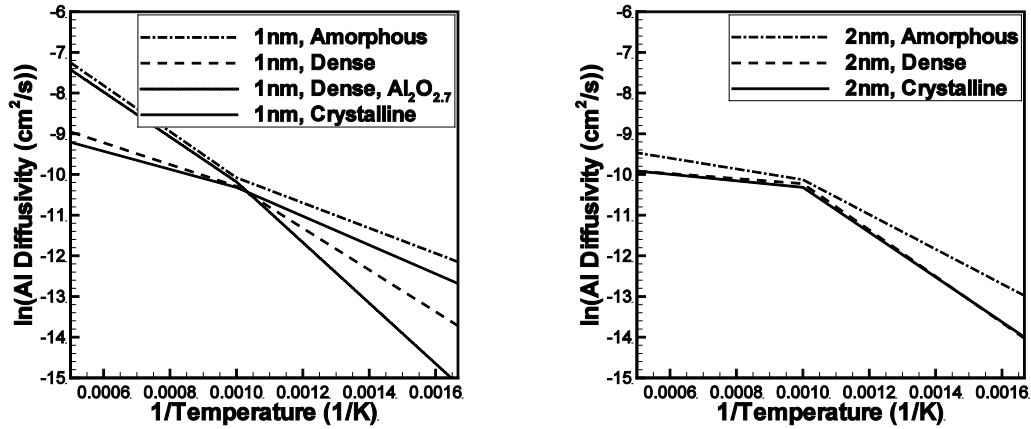


Figure 5.4: Arrhenius plot of $\ln(D)$ versus $1/T$, where D is the diffusivity of the core aluminum atoms. The slope of this plot is the activation energy required for diffusion of aluminum cations and shows an expected decrease above the melting point of the core, at approximately $0.001/K$.

In Figure 5.4 an Arrhenius plot of the diffusivity versus temperature is given for each of the oxide shell configurations used with the 5.6nm aluminum core in this work. From Figure 5.4 we observe that a change in slope occurs near the melting point of the aluminum core, namely 1000K. This indicates that for temperatures above 1000K the activation energy required for cation diffusion is lower than for temperatures below 1000K. The increase in activation energy for the 1nm amorphous and dense oxygen poor shells in Figure 5.4, is likely due to a lower melting point for these oxide shells. This is not the case, for thicker or more crystalline shells where the oxide remains in the solid phase, and does not undergo any phase transformation. In the remaining model systems the activation energy drops once the melting temperature is reached, indicating a change in diffusion mechanism. The primary change that occurs at around 1000K is the melting of the aluminum core, the associated volumetric expansion, and increased mobility of the aluminum atoms. This expansion is expected to greatly increase the pressure inside of the core, and enhance the diffusion of aluminum cations radially outward through the oxide shell.

5.6 Induced Electric Field in Oxide Shell

One possible explanation for the computed rapid diffusion of aluminum atoms through the oxide layer is that they are driven by an induced electric field near the core/shell interface. The theory that oxidation growth proceeds via migration of charged particles is not a new one. In fact Carl Wagner proposed this theory in 1933.¹¹⁵ In a 1948 paper by Cabrera and Mott¹¹³ the authors developed a theory focused on the growth of a thin oxide film on metal surfaces that is driven by an induced electric field. This electric field causes metal ions to migrate to the surface, increasing the oxide thickness until the induced field is prevented by the thickening surface to cause further diffusion of metal cations. The maximum thickness of the oxide layer that is formed with this process increases with temperature, up to a critical temperature above which growth of the oxide layer will continue indefinitely.

Recent theoretical and experimental evidence points to the importance of the induced electric field described by Cabrera and Mott in the oxidation of oxide coated metal nanoparticles. Zhdanov and Kasemo¹²² recently performed an analysis of the induced electric field in oxide coated nanoparticles. They found that by considering the size and geometry effect of nanoparticles coated with oxide shells that the induced electric field will be much stronger than observed in a flat surface, thus increasing the associated oxidation rate exponentially in oxide coated nanoparticles. We have also observed the formation of hollow particles [111, Figure 2] during the oxidation of oxide coated aluminum, which we attributed to the faster diffusion of Al cations. Subsequently Nakamura et al¹¹² also observed formation of hollow metal oxide nanoparticles from the oxidation of metals and attributed the rapid diffusion of metal ca-

tions through the oxide shell to the induced electric field. In the following sections we investigate the magnitude and effect of the induced electric field on the oxide coated aluminum nanoparticle system.

In the current simulation effort, rapid diffusion of aluminum cations through the oxide layer is observed. An indicator of the strength of the electric field is the radial charge density. The radial charge density is computed through the nanoparticle at 2Å radial intervals. The computed charge density is averaged over 100ps of simulation time. Although noisy, which is partially caused by atomic diffusion, it is apparent that there is a negative charge gradient throughout the oxide shell. This charge gradient contributes to the out flow of positive charges, and the mass flux of aluminum cations at the core/shell interface.

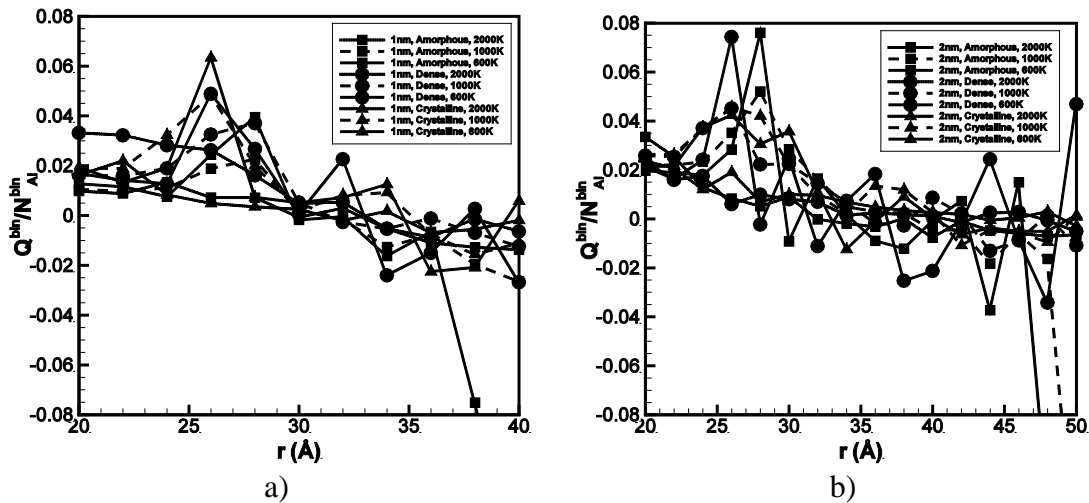


Figure 5.5: Radial charge distribution through the oxide shell for a 1nm (a) thick shell and a 2nm (b) thick shell.

The difference in charge density between the inner and outer surfaces of the oxide shell indicates that an electric field is induced which will drive aluminum cations near the core/shell interface to the outer surface where they will be exposed to oxygen and oxidize. An approximate interaction between an aluminum cation, with the core and

shell can be computed using Gauss's Law. By assuming the atomic charges to be distributed approximately homogeneously in the shell and the core, the electric field on the surface of the core can be estimated as the field from a single point charge at the center of the core, through equation 2. If we assume the charge to be evenly distributed in the oxide shell then the electric field inside of the shell from the atoms in the oxide shell is zero.

$$E = \frac{Q_{core}}{4\pi\epsilon_0 r^2} \quad 5.2$$

In equation 5.2, Q_{core} is the total charge of the core, r is the radial position of the interfacial aluminum atom of interest, and ϵ_0 is the permittivity of a vacuum. Using equation 5.2 the electric fields from the various oxide coated models are computed in Table 5.2.

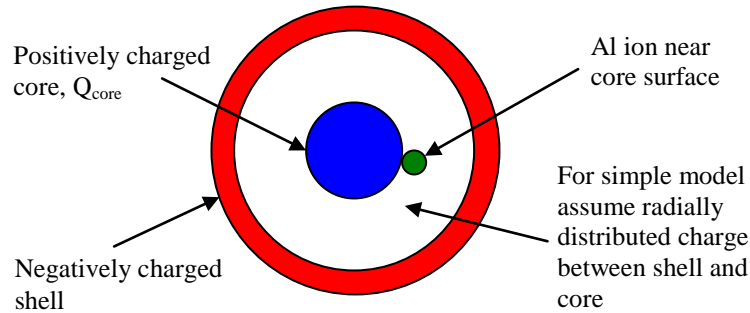


Figure 5.6: Schematic of assumed charge distributions affecting electric field around core surface aluminum atoms.

In Figure 5.6 the volume between the core surface and outer surface of the oxide shell is assumed to be a vacuum. For the purpose of computing the electric field, this assumption is valid so long as the charges in the oxide shell are distributed radially on-

ly. With a radially distributed charge the electric field due to the oxide shell is zero everywhere for atoms at the core/shell interface or inside of the aluminum core.

Table 5.2: Total charge of aluminum core and associated electric field are given here for all of the core/shell configurations considered. Note on electric field units, N/C = 0.01 V/m.

Shell Thickness	Type	Temperature	$Q_{\text{core}} (\text{C} \cdot 10^{-18})$	$E (\text{N/C} \cdot 10^{10})$
1nm	Amorphous	600K	8.28	1.10
1nm	Amorphous	1000K	5.67	0.75
1nm	Amorphous	2000K	1.47	0.20
1nm	Dense	600K	11.4	1.52
1nm	Dense	1000K	8.86	1.18
1nm	Dense	2000K	4.01	0.53
1nm	Dense, Al ₂ O _{2.7}	600K	7.91	1.05
1nm	Dense, Al ₂ O _{2.7}	1000K	6.38	0.85
1nm	Dense, Al ₂ O _{2.7}	2000K	1.09	0.14
1nm	Crystalline	600K	12.7	1.69
1nm	Crystalline	1000K	10.8	1.44
1nm	Crystalline	2000K	3.04	0.40
2nm	Amorphous	600K	13.3	1.77
2nm	Amorphous	1000K	11.9	1.58
2nm	Amorphous	2000K	4.61	0.61
2nm	Dense	600K	13.8	1.83
2nm	Dense	1000K	12.7	1.69
2nm	Dense	2000K	4.21	0.56
2nm	Dense, Al ₂ O _{2.7}	600K	11.6	1.54
2nm	Dense, Al ₂ O _{2.7}	1000K	11.1	1.47
2nm	Dense, Al ₂ O _{2.7}	2000K	7.80	1.04
2nm	Crystalline	600K	15.6	2.08
2nm	Crystalline	1000K	13.9	1.85
2nm	Crystalline	2000K	4.39	0.58
2nm, 8nm Core	Crystalline	600K	43.9	2.47
2nm, 8nm Core	Crystalline	1000K	42.6	2.40
2nm, 8nm Core	Crystalline	2000K	30.4	1.71

The most obvious trend observed in Table 5.2 is that of the decreasing core charge and electric field strength with increasing temperature. This is likely due to the fact that as shown in Table 5.1, diffusivity increases as temperature increases, and smears the boundary between the core and shell. Another observed trend, albeit weaker, is an increase in the electric field as the shell becomes thicker, and more organized. So in

going from an amorphous 1nm thick shell to a 2nm thick crystalline shell we observe a 100% increase in the electric field strength. This observation is supported by the analysis of Zhdanov and Kasemo.¹²²

A more accurate method of computing the electric field at each ion in the core and shell is to use Coulomb's Law and to sum the discrete contribution from all the neighboring charges. Using this method is straight forward since there are a finite number of discrete charge carrying atoms. In Figure 5.7 the computed electric field, using equation 5.3, is plotted at each of the core aluminum atoms.

$$E = \frac{q}{4\pi\epsilon_0 r^2} \hat{e}_r \quad 5.3$$

In equation 5.3 \hat{e}_r is the radial unit vector coming from the neighboring atom and q is the charge associated with the neighboring atom. Summing each of these vectors for all of the core atoms gives the results as shown in Figure 5.7 for 600K, 1000K, and 2000K.

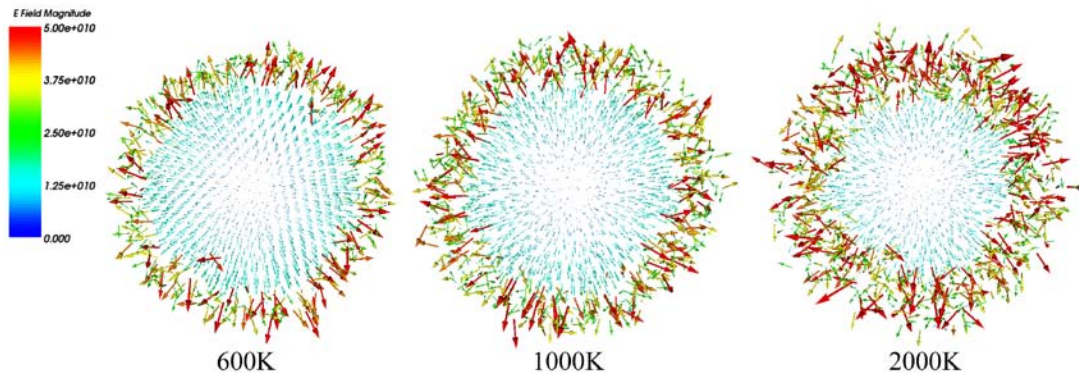


Figure 5.7: Electric field (N/C) at each of the core Al atoms in the nanoparticle core computed using Coulomb's Law. These results are for the 5.6nm core with a 2nm thick crystalline shell. Note the generally radial direction of the field.

The electric field plotted in Figure 5.7 is within an order of magnitude of the simple model results, tabulated in Table 5.2, which assumes a homogeneous charge distribution in the core and oxide shell. The direction of the computed electric field indicates that the mass flux due to the electric field is directed out through the oxide shell rather than acting to randomly rearrange the atoms. The positively charged core aluminum atoms will therefore be preferentially directed towards the outer surface of the oxide shell, where they will come into contact with oxygen ions and oxidize.

With the diffusion coefficients previously computed and the electric field results computed here it is possible to analyze the mass flux due to concentration gradients (J_d), the electric field (J_e), and the internal pressure (J_c). The relative magnitude of the effect of the electric field on Al ion diffusion can be computed using the Nernst-Planck equation. The Nernst-Planck equation is given in equation 5.4.¹²³

$$J = -D \frac{dC}{dx} - \frac{zFDC}{RT} \frac{d\phi}{dx} + C v \quad 5.4a$$

$$J = J_d + J_e + J_c \quad 5.4b$$

If we assume a zero molar concentration of Al cations in the shell and the bulk concentration at the core/shell interface then the parameters for equation 5.4a are given as the following.

$$C = 0.1 \text{ mol/cm}^3$$

$$\frac{dC_{1nm}}{dx} = 1.0 \cdot 10^6 \text{ mol/cm}^4$$

$$R = 8.314 \text{ C}\cdot\text{V/mol}\cdot\text{K}$$

$$F = 96485 \text{ C/mol} \quad 5.5$$

The electric field computed in Table 5.2 is the negative of the charge gradient, $d\phi/dx$.

The convective flux, J_c in equation 5.4 is the drift velocity of metal ions through the core/shell interface due to constant force acting on the ions. The force on these ions comes from the pressure gradient which is due to the expanding aluminum melt. When computing the radial drift velocity, and therefore the radial pressure gradient, J_c in equation 5.4a can be rewritten as $C (Df_r/k_B T)$, where f_r is defined as

$$f_r = -\frac{\partial V}{\partial r} = -\nabla p v_{Al} \quad 5.6$$

In equation 5.6, ∇p is the pressure gradient in the radial direction and v_{Al} is the solubility of Al in the Al_2O_3 network.¹²⁴ The maximum pressure gradients observed in these simulations range from less than 1GPa/nm at 600K to 2GPa/nm at 1000K and above. For the solubility of Al in Al_2O_3 we have assumed a value that comes from previous analysis of oxygen and aluminum diffusion through Al_2O_3 and should therefore be a reasonable value. Assuming a value of about $0.02nm^3$ for the solubility of Al (v_{Al}) it is possible to estimate the mass flux due to each term in equation 5.4. The diffusivity due to the drift velocity is directly proportional to v_{Al} but variations here by less than one order of magnitude would have little effect on the results in Table 5.3.

Table 5.3: Diffusion coefficient and mass flux computed at 600K, 1000K, and 2000K for all shell configurations with the 5.6nm core unless noted. The last column labeled Ratio J_e to J , is the fraction of the total mass flux due to the induced electric field, with the balance due to the concentration gradient and drift velocities.

Shell Thickness	Configuration	Temperature	J (mol/cm ² ·s)	D (cm ² /s *10 ⁻⁸)	Ratio J_e to J
1nm	Amorphous	600K	4.20	1.97	0.98
1nm	Amorphous	1000K	11.97	13.6	0.96
1nm	Amorphous	2000K	53.45	424.0	0.83
1nm	Dense	600K	3.03	1.03	0.99
1nm	Dense	1000K	11.49	8.33	0.97
1nm	Dense	2000K	35.18	110.8	0.93
1nm	Dense, Al ₂ O _{2.7}	600K	2.13	1.03	0.98
1nm	Dense, Al ₂ O _{2.7}	1000K	8.06	7.88	0.96
1nm	Dense, Al ₂ O _{2.7}	2000K	46.27	426.0	0.78
1nm	Crystalline	600K	5.08	1.55	0.99
1nm	Crystalline	1000K	14.72	8.75	0.98
1nm	Crystalline	2000K	35.58	147.0	0.91
2nm	Amorphous	600K	3.31	0.97	0.99
2nm	Amorphous	1000K	18.49	10.0	0.98
2nm	Amorphous	2000K	23.73	65.2	0.94
2nm	Dense	600K	1.26	0.35	0.99
2nm	Dense	1000K	6.13	3.11	0.98
2nm	Dense	2000K	11.34	33.8	0.93
2nm	Dense, Al ₂ O _{2.7}	600K	3.69	1.23	0.99
2nm	Dense, Al ₂ O _{2.7}	1000K	7.99	4.58	0.98
2nm	Dense, Al ₂ O _{2.7}	2000K	5.27	8.38	0.96
2nm	Crystalline	600K	7.83	1.94	0.99
2nm	Crystalline	1000K	15.06	6.98	0.98
2nm	Crystalline	2000K	6.81	19.6	0.93
2nm, 8nm Core	Crystalline	600K	17.27	3.59	0.99
2nm, 8nm Core	Crystalline	1000K	24.31	8.61	0.99
2nm, 8nm Core	Crystalline	2000K	31.27	30.8	0.98

From the final column in Table 5.3, listing the ratio of J_e to J , it is apparent that in all cases except for two, over 90% of the mass flux through the oxide shell is due to the induced electric field present at the core/shell interface. The exceptions to this 90% observation are the 1nm amorphous and 1nm dense Al₂O_{2.7} shells at 2000K, which from previous analysis appear to have undergone a phase change at this tem-

perature. This result illustrates the importance of considering the electric field in the nanoparticle for any oxidation analysis of the oxide coated aluminum nanoparticle system. Another interesting trend is that the importance of the electric field in diffusion increases, as both the shell thickens and the temperature decreases. The trend associated with temperature is expected since diffusion without an electric field is strongly temperature and pressure dependent, and at low temperatures diffusion would be very slow without an electric field. The trend associated with shell thickness requires some more thoughtful analysis. By considering the computed electric fields in Table 5.2, we observe that the magnitude does indeed increase with shell thickness while the overall mass flux decreases, Table 5.2 and Figure 5.8.

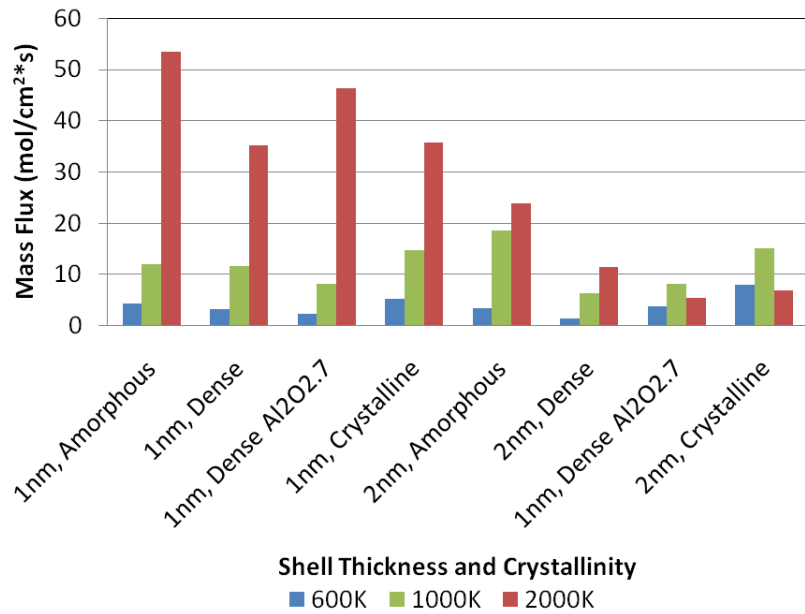


Figure 5.8: Plot of mass flux versus temperature and shell configuration.

Figure 5.4 is a plot of the mass flux versus oxide shell configuration and temperature. In Figure 5.8 we observe some interesting trends not necessarily apparent in Table 5.3. For nanoparticle systems at 600K and 1000K the degree of crystallinity in

the oxide shell does not appear to have a noticeable effect on the mass flux of the aluminum cations through the oxide shell. This result is interesting because we can conclude that the reaction rate for oxide coated aluminum nanoparticles in this size range will not be dependent on how the coating was formed or upon its thickness, up to 2nm.

The most apparent trend in Figure 5.8 is that the mass flux of aluminum atoms through the shell at 2000K decreases with increasing shell crystallinity and thickness. This result is likely due to the increased dependence of total mass flux on the concentration gradient and drift velocity terms in equation 5.4 as opposed to being solely due to the electric field. This is observed as lower values in the last column in Table 3 for 2000K versus 600K and 1000K for more crystalline and thicker oxide shells. Since the heating rate required to reach 2000K before an appreciable amount of the core has diffused into the shell is so high, greater than 10^{12} K/s, we would not expect this to be an experimentally observable result without some sort of very rapid heating method.

5.7 Formation of Hollow Aluminum Oxide Shells

Recent experimental efforts by Rai et al¹¹¹ and Nakamura et al¹¹² have both observed the formation of hollow aluminum oxide nanoparticles as a result of the oxidation of oxide coated aluminum nanoparticles. In the work by Rai et al¹¹¹ we observed the formation of hollow spheres of aluminum oxide subsequent to the oxidation of aluminum nanoparticles at about 727K. We expected that these hollow oxide shells are produced by the outward diffusion of aluminum through the oxide shell as opposed to inward diffusion of oxygen. This observation is supported here by the high measured

diffusion coefficients for aluminum cations and mass flux due to the electric field in the nanoparticle.

In order to better compare the inward diffusion of oxygen versus the outward diffusion of aluminum we have simulated a 5.6nm aluminum core with a 2nm crystalline oxide shell in a high density oxygen gas as shown in Figure 5.9. The diffusion of oxygen ions through the shell has the potential to limit the mass flux of aluminum cations emanating from the core, resulting in reactions inside of the oxide shell and at the core/shell interface as opposed to on the nanoparticle surface. Oxidation in the core would potentially increase the internal pressure of the nanoparticle from volumetric expansion resulting in mechanical failure of the oxide shell, but be unlikely to result in the hollow shells observed by Rai et al.¹¹¹

In Figure 5.9 it is apparent that the diffusivity of aluminum cations through the oxide shell is observably higher than the diffusion rate of oxygen anions towards the core. This result indicates that oxidation will occur on or near the outer surface of the oxide shell rather than at or near the core/shell interface. By the oxidation reaction occurring on the outer shell surface, an outward growth of the oxide shell is observed which ultimately results in a hollow aluminum oxide shell as observed experimentally.^{111,112} One effect that may limit the mass flux of oxygen atoms into the oxide shell is that at higher temperatures the sticking probability of the gas molecules is lower than for temperatures $<623\text{K}$.¹²⁵

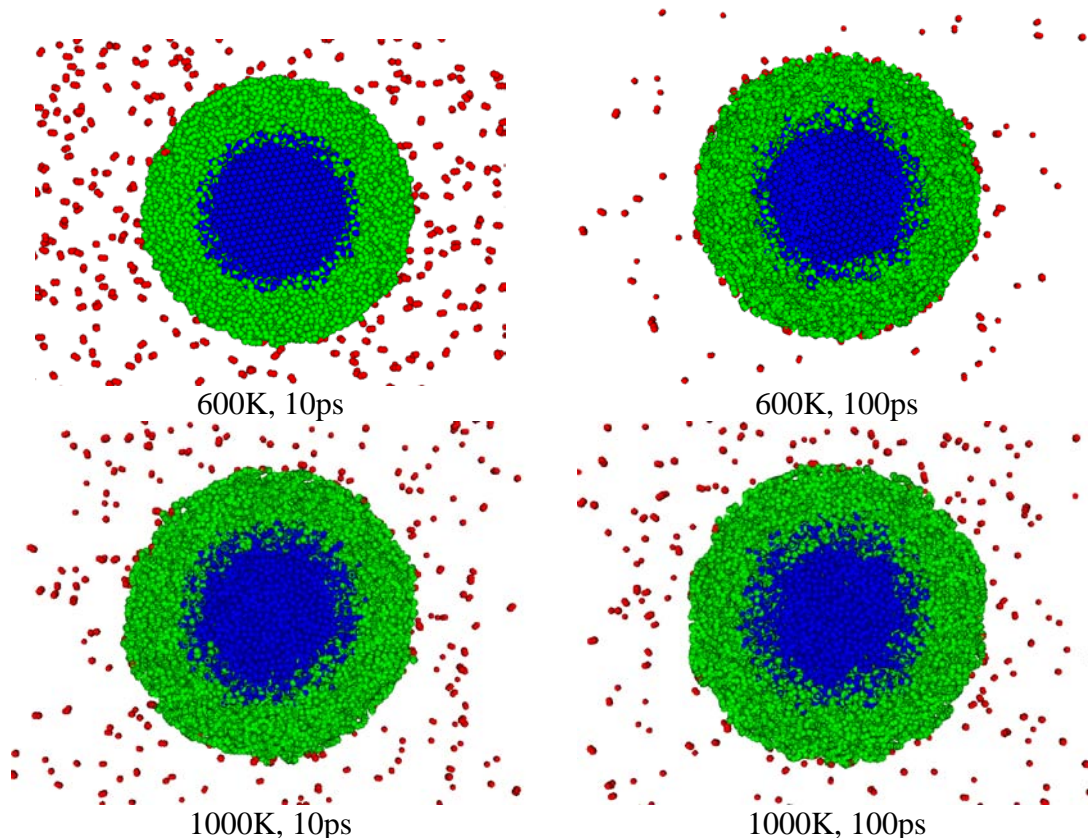


Figure 5.9: Cross section of oxide (green) coated aluminum core (blue) showing surrounding oxygen (red) atoms. Higher rates of diffusion for aluminum cations is observed by aluminum atoms moving radially outward into the oxide shell atoms while adsorbed oxygen atoms remain on the outer surface or desorb from the shell. Figures a and b are at 600K and represent 10ps and 100ps of simulation time, respectively. Figures c and d are at 1000K, after 10ps and 100ps, respectively.

5.8 Conclusions

For small oxide coated aluminum nanoparticles we have found that the oxidation process is likely to occur by rapid diffusion of aluminum cations through the oxide shell as opposed to mechanical failure or melting of the shell, for heating rates as high as 10^{12} K/s. The high level of measured aluminum cation diffusivity is driven not only by the volumetric expansion of the aluminum core, but primarily by the induced electric field in the oxide shell. This enhanced diffusivity due to the induced

electric field is supported by theoretical analysis of the Cabrera-Mott effect for oxide coated nanoparticles.¹²² Oxidation by rapid diffusion of aluminum ions to the nanoparticle surface is also in agreement with published experimental efforts that have observed the formation of hollow aluminum oxide nanoparticles.^{111,112} Diffusion of oxygen ions into the shell has also been considered but does not contribute appreciably when compared to the flux of aluminum to the nanoparticle surface.

6 Computer Simulation of the Mechano-Chemical Behaviour of Oxide Coated Aluminum Nanoparticles

6.1 Introduction

In this chapter I investigate the chemical and mechanical response of oxide coated aluminum nanoparticles to heating via homogeneous flame and heterogeneous laser methods. The current body of literature for oxidation of oxide coated aluminum nanoparticles focuses on melting or mechanical failure (cracking) of the oxide shell as the initiator of the reaction mechanism. Examples of this theory are the melt dispersion mechanism presented by Levitas et al,^{108,109} and the cracking and reduced temperature melting of the oxide shell by Puri and Yang.¹¹⁰

In the reaction described by Levitas et al the oxide shell ruptures violently from the internal pressure exerted on it due to the expansion of the aluminum core upon melting. This scenario, the so-called melt dispersion mechanism, makes some assumptions about mechanical properties which may have temperature or size dependencies and that the diffusion coefficient of the aluminum cations must be below 10^{-5} cm^2/s ¹⁰⁹ or more specifically around 10^{-18} cm^2/s for the melt dispersion mechanism to occur. In Levitas et al^{108,109} the authors also state that for rupture to occur the ratio of the oxide shell thickness to the nanoparticle radius must be larger than 5 for an assumed shell strength of about $1/2$ to $1/3$ of the theoretical strength for Al_2O_3 or a ratio of over 20 for shells approaching the theoretical strength of Al_2O_3 . This maximum nanoparticle size falls outside of the range of nanoparticles analyzed in this work and

will be considered in a future effort. In this work we have investigated core radius to shell thickness ratios of between 1.3 and 5.3, and comment on the trends observed. In addition to the so-called melt dispersion mechanism Puri and Yang¹¹⁰ have theorized that the oxidation process does not proceed until the oxide shell has melted. The melting temperature of the oxide shell is lower than the bulk melting temperature and is predicted to melt at around 1100K,¹¹⁰ a much lower temperature than that observed in bulk Al₂O₃, namely 2327K, and is relatively close to the melting temperature of bulk aluminum.

Molecular dynamics (MD) simulations performed here show another possible mechanism for oxidation of oxide coated aluminum nanoparticles, namely rapid diffusion driven by an induced electric field. The flux of aluminum cations driven by this electric field through the oxide shell limits the internal pressure buildup during melting of the aluminum core by removing atoms from the core. Experimentally produced hollow aluminum oxide nanoparticles provide support for this rapid diffusion hypothesis^{111,112} by demonstrating that undamaged hollow oxide shells are observed under laboratory conditions. The primary discrepancy between this experimental work and the computer simulations performed here is that the temperatures considered in the experiments were held below the melting point of the aluminum core. We will show here that field mediated ion-transport is much faster than Fickian diffusion and will be the dominant transport process in the oxidation of nanoaluminum. Additional support for this transport mechanism comes from numerous numerical^{113,114} and experimental studies.^{115,116}

In this work we explore the pressure generated in the core and oxide shell during melting of the aluminum core and compare results for three sizes of aluminum cores, namely 5.6nm, 8.2nm, and 21nm. The oxide shell thicknesses considered are 1nm and 2nm, with various configurations from amorphous to crystalline. The results of these simulations are used to compare with the oxidation mechanisms reported elsewhere.¹⁰⁸⁻¹¹⁰ We will also provide comment on expected size dependent trends, providing clues as to the mechanisms expected in nanoparticles larger than those explicitly considered here.

6.2 Simulation Approach

For this effort we have again chosen to use the ReaxFF empirical potential from van Duin¹¹⁷ implemented within the GRASP MD application. The computational requirement of this software is high with the largest system here containing nearly 600k atoms and is simulated efficiently with 2048 AMD processor cores running at 2.3 GHz.

6.3 Model Description

The first model system considered here consists of a 5.6nm diameter core of aluminum with either a 1nm or 2nm thick shell of Alumina (Al_2O_3) as illustrated with the example systems in Figure 6.1. The larger models used in this effort include an 8.2nm aluminum core and a 21nm aluminum core with a 2nm thick crystalline oxide shell as shown in Figure 6.2.

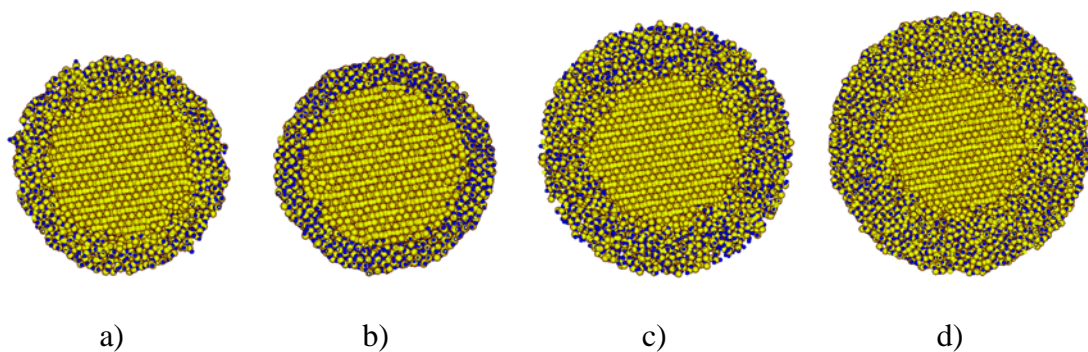


Figure 6.1: Cross sections of some of the oxide coated aluminum nanoparticle models used in this work. a) 1nm thick, dense oxide shell. b) 1nm thick, crystalline oxide shell. c) 2nm thick, amorphous oxide shell. d) 2nm thick, dense oxide shell with 2:2.7 Al:O ratio. Blue spheres represent oxygen atoms and yellow spheres denote aluminum atoms.

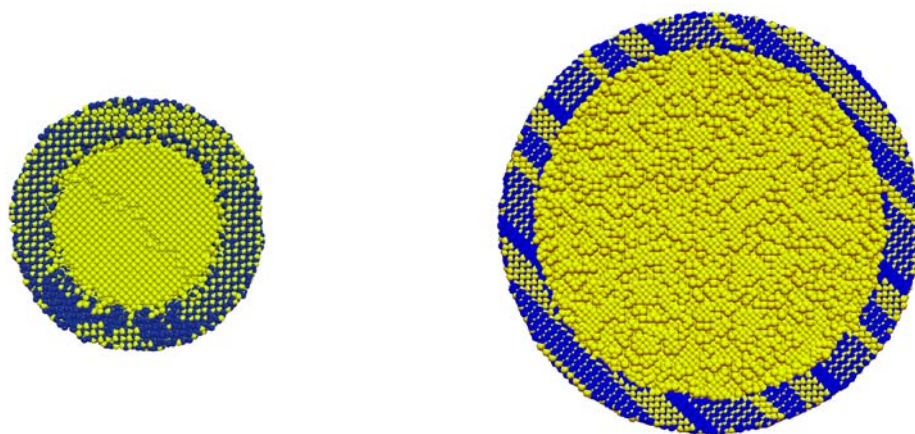


Figure 6.2: Configuration of atoms for larger (8.2nm, left) and (21.0nm, right) nanoparticle cores. Yellow denotes aluminum atoms and oxygen atoms are blue.

The same four shell configurations are considered here for the 5.6nm core as are used in the previous chapter.

After formation and equilibration of the oxide shells, the model systems were heated at rates of 10^{11} K/s, 10^{12} K/s, and 10^{13} K/s in order to determine any rate dependencies. We found, similarly to Puri and Yang,¹¹⁰ that at rates below 10^{12} K/s the heat-

ing rate appears to have little effect on the simulation results. Using a heating rate of $3.5 \cdot 10^{12} \text{K/s}$ the temperature of the model systems was raised from 300K to 1000K and eventually up to 3000K. This maximum temperature is used to simulate the laser heating process which rapidly heats the nanoparticle core to temperatures up to and above 3000K.

6.4 Results of Homogeneous Heating Simulation

The initial simulations in this work were carried out in a vacuum so that as Al ions reach the outer surface of the oxide shell they will not be exposed to oxygen molecules for further oxidation reactions. This assumption is made to limit the size of the simulations and increase the time and nanoparticle sizes that can be simulated. Simulations performed elsewhere indicate that this approximation is valid because the diffusivity of the aluminum cations through the oxide layer is much higher than the diffusivity of the oxygen anions towards the core.¹²⁶ Therefore we are primarily concerned with the mechanism by which Al cations reach the surface of the nanoparticle.

In order to compare the proposed oxidation mechanism, namely electric field driven diffusion of aluminum ions, with published theories the nanoparticle models were heated from 300K to about 1000K, which is above the core melting point but below the size dependent oxide shell melting temperature reported by Puri and Yang.¹¹⁰ Beginning at about 900K, or slightly below the bulk melting temperature of the aluminum core, a rapid volumetric expansion of the core is observed, indicating that the aluminum core has melted. After reaching 1000K the oxide shell is still intact, even after holding at this temperature for up to 100ps we do not observe cracking

of the shell. Instead we observe a large number of the aluminum cations from the core beginning to diffuse to the surface of the nanoparticle, Figure 6.3.

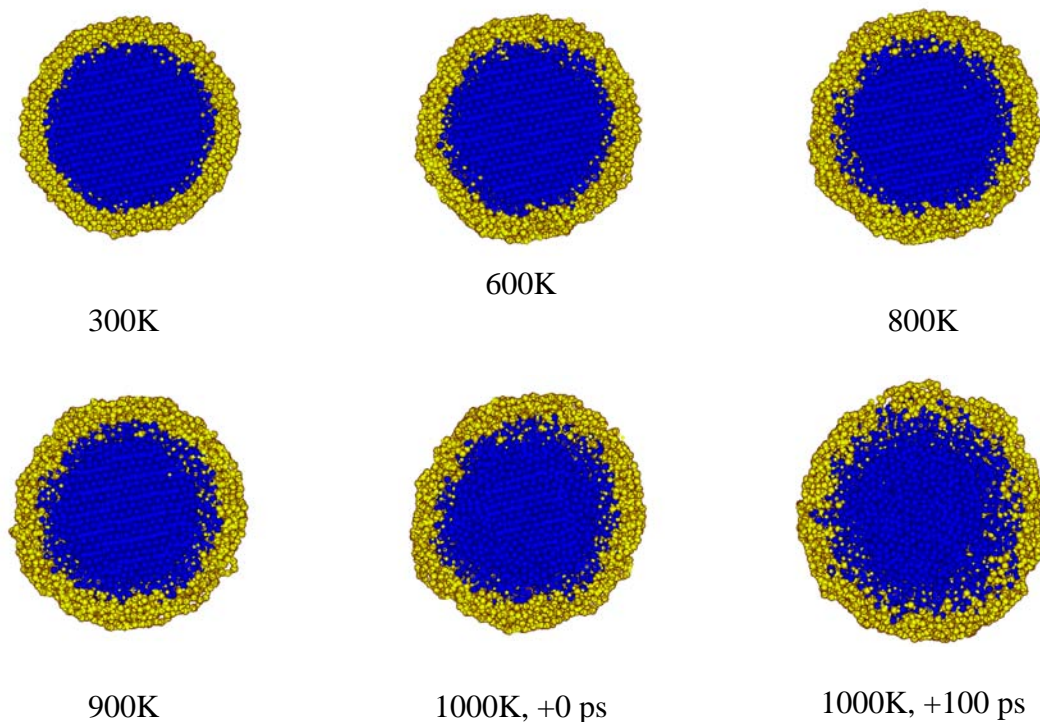


Figure 6.3: Plot showing diffusion of aluminum cations (blue) through the oxide shell (yellow) as the temperature increases from 300K to 1000K and held for 100 ps.

These simulation results in Figure 6.3 offer some insight into the mechanism by which oxidation proceeds at elevated temperatures for homogeneously heated nanoparticles. The first observation is that the oxide shell does not crack as one might expect if diffusion were extremely limited or the shell were brittle and stress in the oxide shell due to core expansion was high. This suggests that the shell is more elastic at this scale than observed in the bulk material, the expansion of the aluminum is insufficient to cause failure in the shell, or diffusion of aluminum ions through the oxide shell mitigates the pressure build up in the core. One possible reason for the lack of mechanical failure is an increased elasticity due the lower configuration of the

atoms in the oxide shell as compared to the bulk material. This same mechanism also contributes to the size dependent melting temperature observed in nanoparticles. The high diffusivity of aluminum cations is primarily driven by an induced electric field at the interface of the aluminum core and oxide shell. The source and magnitude of this electric field has been discussed previously.¹²⁶

6.5 Heterogeneous Laser Heating

As a comparison to experimental efforts^{127,128} we consider the heterogeneous heating that occurs during single particle mass spectrometry analysis. Particle heating in this experimental process is achieved by using a laser to rapidly heat the nanoparticle, eventually ionizing the atoms thus allowing for an analysis of particle mass and composition. However, when a laser is used to heat an oxide coated aluminum nanoparticle a heterogeneous heating of the various materials is observed. Heating is achieved through adsorption of energy from the laser but the amount of energy absorbed by each material depends upon the characteristics of the material. In the case of an aluminum oxide (Al_2O_3) coated aluminum nanoparticle the oxide coating adsorbs much less energy than the aluminum core. This causes the bulk of the laser's energy to be absorbed by the aluminum core resulting in a hot core with a cool oxide shell. When the core reaches its melting temperature the expected volumetric expansion is observed, possibly generating large stresses in the oxide shell which is still at a relatively low temperature. This differs from the previous simulations where homogeneous flame heating was assumed and the core and shell were at the same temperature throughout. This temperature difference in laser heating has the potential of resulting in a more brittle and highly structured oxide shell than when the higher homogeneous

temperature is assumed for the oxide shell and core. It is anticipated that if failure of the oxide shell is observed that it will occur under these conditions.

In the experimental work of Zhou et al^{127,128} the heating rate by laser is estimated to be around 10^{13} K/s, or close to the rate used in much of this work, namely 10^{13} K/s for laser heating simulations and $3.5 \cdot 10^{12}$ K/s for flame heating. The final temperature observed prior to ionization is approximately 3000K. In the following simulations the shell has been held at a constant temperature of around 440K while the core is heated from 440K up to a final temperature of 3000K.

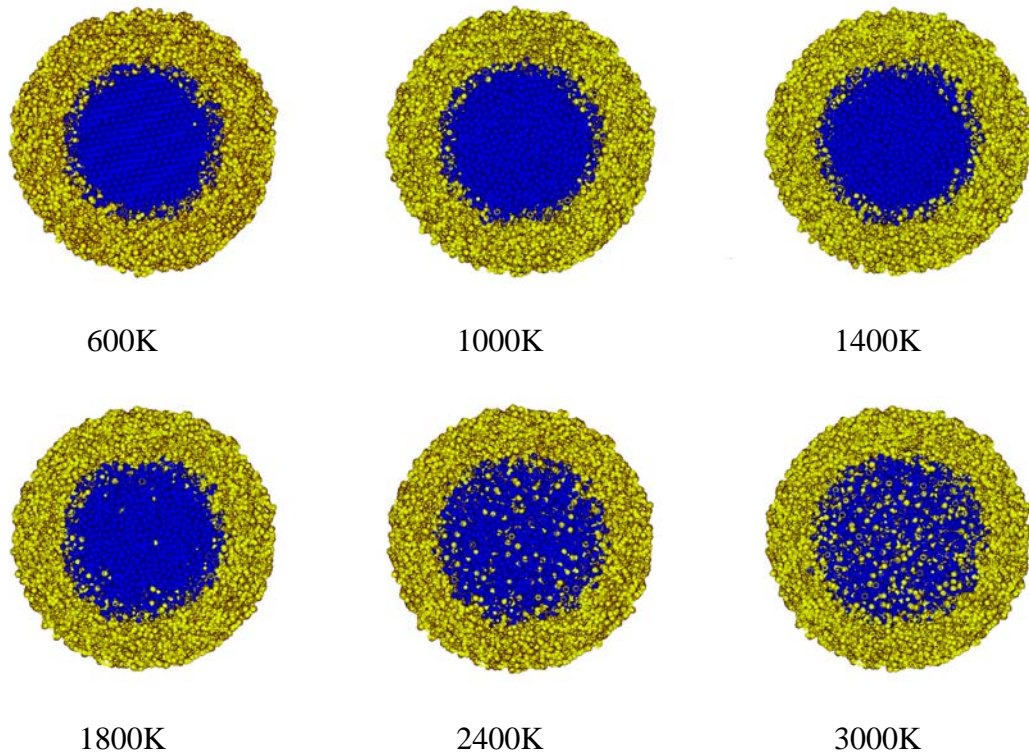


Figure 6.4: Time elapsed simulation results of laser heating experiments with the 2nm thick crystalline shell at 440K and the 5.6nm core heated from 440K to 3000K.

In Figure 6.4 we have plotted a cross section of the laser heated 5.6nm nanoparticle at core temperatures from 440K to 3000K. From these plotted results it is apparent that for nanoparticles of this size, i.e. core diameter of 5.6nm, the stress induced within the oxide shell is not sufficient to cause mechanical failure. Even though in contrast to the flame heated nanoparticles where the diffusivity of aluminum ions through the oxide shell was high, diffusion is severely restricted here. This restriction of aluminum cation diffusion can be observed by the lack of core aluminum ions in the oxide shell even for a core temperature of 3000K.

In addition to volumetric expansion, the ratio of the size of the aluminum core to the thickness of the oxide shell is expected to affect core pressure and failure of the oxide shell. An analysis of the required core size for a 2nm thick oxide shell is performed by considering 5.6nm, 8.2nm, and 21nm core sizes with homogeneous flame heating.

6.6 Aluminum Ion Diffusion through the Oxide Shell

As observed and discussed elsewhere,^{110,126} at temperatures below the melting point of the oxide shell there is noticeable diffusion of aluminum cations through the oxide shell. In addition, during this simulation effort we have observed increasing radial diffusion rates through the shell with increases in temperature. To support this observation the ratio of the effective radial diffusivity is compared to the overall effective diffusivity in Figure 6.5.

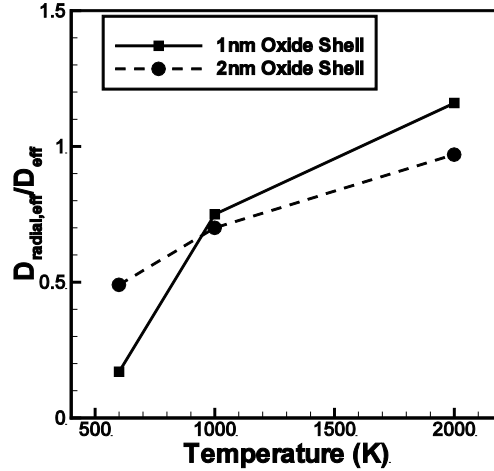


Figure 6.5: Ratio of effective radial diffusivity to the overall effective diffusivity.

In Figure 6.5 the ratio of effective radial diffusivity to effective total diffusivity increases with temperature. This is interpreted as an indication that as the aluminum core melts and heats up the diffusion of aluminum ions through the oxide shell towards the exposed surface is increasing more rapidly than the overall diffusion rate. Note that if all of the diffusion were in the radial direction, a maximum ratio of 3 would be reached¹²⁰ in Figure 6.5.

With the diffusion coefficients and the induced electric field results computed elsewhere¹²⁶ it is possible to compare the mass flux due to concentration gradients (J_d), the electric field (J_e), and the internal pressure (J_c). The relative magnitude of the effect of the electric field on Al ion diffusion can be computed using the Nernst-Planck equation. The Nernst-Planck equation is given in equation 6.1.¹²³

$$J = -D \frac{dC}{dx} - \frac{zFDC}{RT} \frac{d\phi}{dx} + Cv \quad (6.1a)$$

$$J = J_d + J_e + J_c \quad (6.1b)$$

A comprehensive explanation of the Nernst-Planck equation with the parameters used here is given elsewhere.¹²⁶

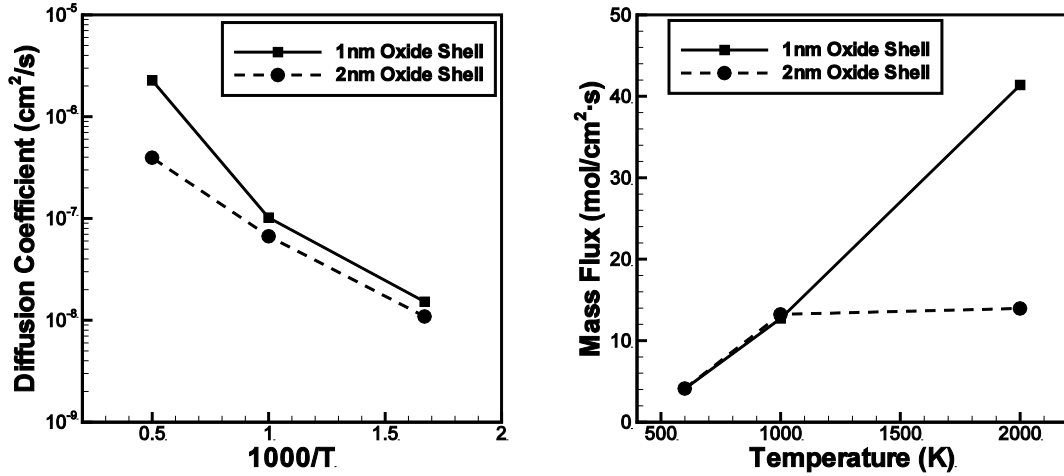


Figure 6.6: In (a) we have plotted the diffusion coefficient for aluminum cations versus $1000 \cdot T^{-1}$ and in (b) the computed mass flux of aluminum cations through the core/shell interface is plotted versus temperature. This data is from the 5.6nm core model system and averaged over all shell configurations for a specific thickness.

In Figure 6.6a an Arrhenius plot of $\ln(D)$ versus $1000/T$ is plotted using the diffusion coefficient from the Nernst-Planck equation, equation 6.1a. The data in Figure 6.6 is averaged across all shell configurations since we did not observe a large difference between the amorphous, dense, and crystalline structures for each shell thickness simulated. Previous analysis¹²⁶ shows that the relative magnitude of the mass flux due to the induced electric field is much greater than either pressure driven diffusion or Fickian diffusion. This result in combination with the experimental observations elsewhere,^{111,112} showing the intact oxide shell after oxidation of the aluminum core, indicates that initiation of the oxidation process for oxide coated aluminum nanoparticles is primarily diffusion driven from the induced electric field.

6.7 Computed Stress in Oxide Shell

When aluminum undergoes a phase change from solid to liquid it experiences a volumetric expansion of about 12%, i.e. the density decreases from 2.7g/cm^3 to 2.4g/cm^3 . Due to this volumetric expansion of the aluminum in the nanoparticle core it is expected that large tensile stresses (negative pressure) in the oxide shell will be observed. Other factors that will affect the stress in the shell include compression of the core due to surface tension, the bulk modulus of the liquid aluminum, differences in thermal expansion coefficients between the core and shell, and any plastic deformation of the shell that may occur prior to rupture.

A parametric analysis of the pressure and fraction of melt in the aluminum core was performed previously by Levitas et al.¹⁰⁹ From the authors' analysis, fracture of the shell is not expected to occur for ratios of core radius to shell thickness below 5, even for shell strengths approaching 50% of ideal. Using the thinnest shell considered by Levitas et al,¹⁰⁹ i.e. 2nm, requires a core of radius 10nm and result in a model with on the order of 10^6 atoms. When considering charge equilibration, such as in the ReaxFF empirical potential, this becomes a very expensive computation. For a direct comparison with this analysis we have simulated a 21nm diameter aluminum core coated by a crystalline 2nm thick oxide shell with over 600,000 atoms.

In order to compute the pressure in the nanoparticle core and shell model the virial stress^{44,45} formulation is required because of the numerous multibody terms in the ReaxFF empirical potential. When computing the virial stress formulation a stress tensor and pressure value at each of the atoms in the nanoparticle core and shell is evaluated. The result of the virial stress formulation in GRASP is a complete stress

tensor at each atom multiplied by the atomic volume. By computing the trace of each of these tensors it is possible to obtain a pressure value at each atom. This pressure is then averaged over a period of 1ps-10ps. In Figure 6.7 the pressure is computed for the 5.6nm nanoparticle core model with a 2nm thick, dense oxide shell. The pressure values are averaged within 0.4nm shells and over 10ps time periods.

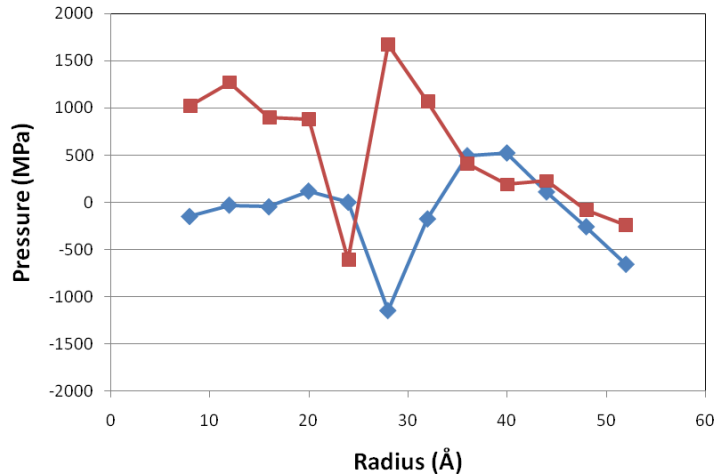


Figure 6.7: Radial pressure distribution for 5.6nm diameter aluminum core at 600K and at 1000K with 2nm thick dense oxide shell and a non-stoichiometric ratio of aluminum to oxygen.

In Figure 6.7 a positive pressure value for a core temperature of 1000K is observed inside of the nanoparticle core, up to a radius of about 2nm (20Å). At the nanoparticle core/shell interface there is a rapid fluctuation in the pressure profile with a negative pressure in the remainder of the shell, indicating a tensile stress. Reasons for some of the noise observed in the pressure data include diffusion of atoms, particularly near the core/shell interface, lattice mismatch between core and shell, and a relatively small sampling size due to the number of simulated atoms. At the core/shell interface there is also the possibility of residual stresses due to mismatches in coefficients of thermal expansion. However, the overall trend is obvious, that there is a

compressive stress in the aluminum core and a tensile stress in the shell. Additionally, the pressure in the core increases appreciably when the system temperature is above the melting point of aluminum.

The question then becomes; is the tensile stress in the shell high enough to cause failure, even cracking as some researchers have suggested may occur?^{108,109} From these simulations and the mechanical analysis performed by Levitas et al¹⁰⁹ the shell is not expected to rupture at these nanoparticle sizes. Furthermore we observe that the oxide shell does not crack but rather aluminum ions diffuse through the shell to the oxide surface prior to oxidizing. For small nanoparticles Puri and Yang¹¹⁰ suggest that complete oxidation occurs after the shell has melted, but from this effort and experimental observations^{111,112} it appears clear that the induced electric field generates a diffusion rate sufficient to cause complete oxidation before melting of the shell if the temperature is controlled. This process is expected to proceed with a high pressure gradient and electric field driving forces until enough of the core atoms have diffused out through the shell to lower the pressure gradient sufficiently at which time only the electric field will drive diffusion. Once the induced electric field of the core and shell is too weak to contribute significantly to diffusion the process halts and will result in the hollow shells observed experimentally by Rai et al.¹¹¹ With the electric field driven diffusion and higher predicted elasticity of the oxide shell at these small sizes it is probable that the nanoparticle size at which mechanical failure of the oxide shell occurs is larger than suggested by previous efforts.^{108,109}

The pressure profile in Figure 6.8 is a result of the homogeneous flame heating of the 8.2nm core model. In Figure 6.8 the pressure in the core and shell do not

rise above approximately 1GPa, indicating that a homogeneously heated nanoparticle will not experience the high pressures necessary for rupture of the oxide shell. The low pressures observed in both model sizes, Figure 6.7 and Figure 6.8, indicates that homogeneous heating is unlikely to produce the high pressure melt dispersion mechanism discussed elsewhere.^{108,109}

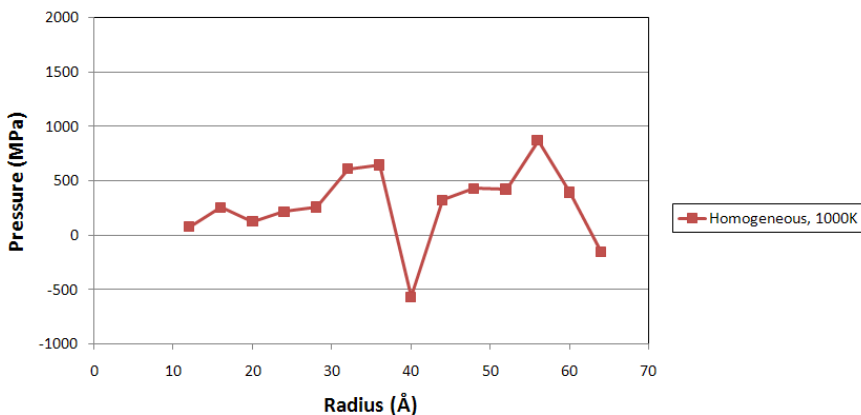


Figure 6.8: Radial pressure distribution for 8.2nm diameter aluminum core at 1000K with a 2nm crystalline oxide shell.

In the next section the same nanoparticle systems have been heated by laser heating in order to provide a heterogeneous radial temperature profile. It is expected that since the oxide shell will be at a lower temperature than in the homogeneous flame heating simulations that the mobility of the Al ions through the shell will be affected, resulting in a higher pressure gradient at the core/shell interface.

6.8 Laser Heating Simulations

Laser heating is used in mass spectrometry analysis to rapidly heat a material sample until the atoms are ionized. This heating process is considered here for oxide coated aluminum nanoparticles. We are interested in determining if the laser heating me-

chanism will cause a different failure mechanism than the diffusion driven oxidation observed with homogeneous flame heating of the nanoparticle core and shell. The laser heating method causes marginal heating in the oxide shell because the oxide shell absorbs energy inefficiently from the laser resulting in a slow heating rate whereas the Al core is more efficient at absorbing the laser energy and is conversely heated very rapidly. The expected result of this heating method is a more brittle shell compared to what is observed in the previous section where homogeneous heating of the oxide coated aluminum nanoparticle is considered. It is anticipated that this heterogeneous heating process is more likely to result in mechanical failure of the oxide shell, or at least a higher internal pressure.

In Figure 6.9 we have plotted cross sections for a homogeneously and heterogeneously heated nanoparticle with a 8.2nm core and a 2nm thick crystalline shell after 100ps at 1000K. The cross section shown in Figure 6.9a is for the homogeneous heating process whereas Figure 6.9b is for the heterogeneous laser heating process with the oxide shell held at 440K as assumed in the complete laser heating simulation.

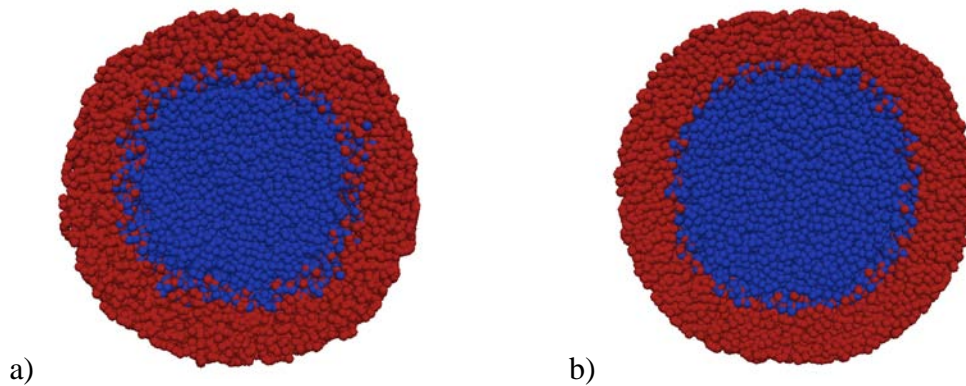


Figure 6.9: Plot of an 8.2nm aluminum core with a oxide shell at 1000K after 100ps (a), and the same nanoparticle heated using a laser resulting in a 1000K core and a 440K oxide shell after 100ps (b).

In Figure 6.9 we observe that for the laser heated nanoparticle the amount of aluminum that has begun to diffuse through the oxide shell at 100ps is visibly lower than for the homogeneously heated nanoparticle. This comparison illustrates that the diffusivity of Al ions is lower with the heterogeneous laser heating process than when using the homogeneous heating process and is therefore more dependent upon the pressure gradient for diffusion, equation 4.¹²⁶ The lower observed diffusivity is also expected to increase the pressure values computed in the core and oxide shell. Higher pressure values are more likely to result in rupture of the oxide shell. In Figure 6.10 the pressure profiles for the laser heating and homogeneous heating process are compared.

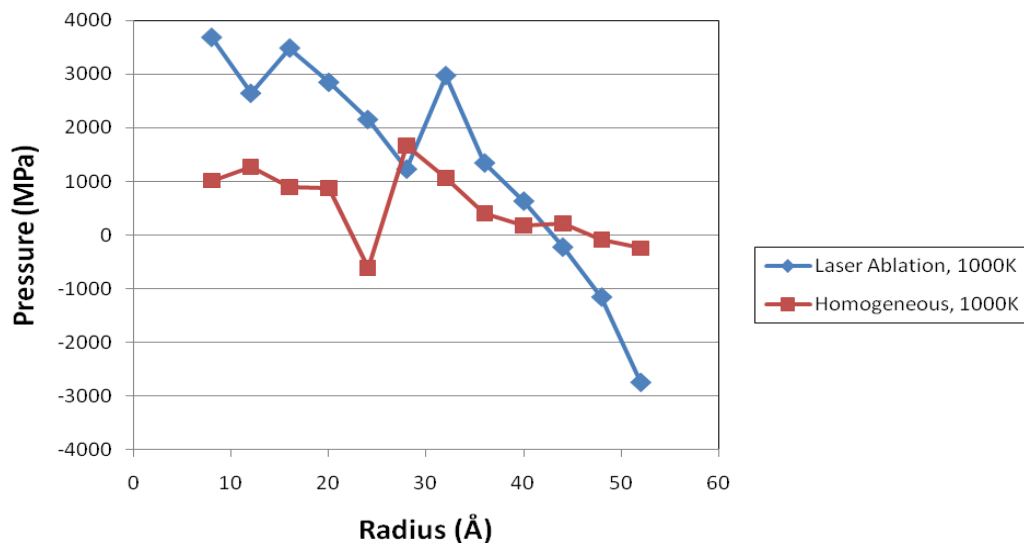


Figure 6.10: Pressure profile averaged over 8ps at 1000K for ambient heating and laser heating of 5.6nm core with 2nm crystalline oxide shell.

In Figure 6.10 a comparison of the radial pressure profiles for a homogeneously and heterogeneously heated oxide coated nanoparticle reveals a dramatic increase in the pressure magnitudes in the nanoparticle when laser heating is used to heat the nanoparticle. A compressive pressure in the nanoparticle core of about 3GPa is three times higher than that observed in the homogeneously heated core, likely due to the limited diffusion of core atoms and lower elasticity of the low temperature shell. The higher tensile stress, or negative pressure, in the oxide shell combined with the lower aluminum ion diffusivity discussed previously gives a clear indication that mechanical failure during the laser heating process is more likely than in the homogeneous heating process.

In order to investigate how the core and shell pressure results scale with core size we have computed the radial pressure distribution in the 8.2nm core model heated homogeneously and by laser heating, Figure 6.11, as was previously done with

the 5.6nm core. Most notable in these pressure results is the difference in pressure between the two systems. As the core size increases for the laser heating simulations the pressure also increases noticeably. For the homogeneously heated nanoparticle case we do not observe the same high pressures present in the laser heating heated particle. In addition, for the homogeneously heated nanoparticle there is not an apparent trend of higher pressures with increased core size as is observed in Figure 6.13.

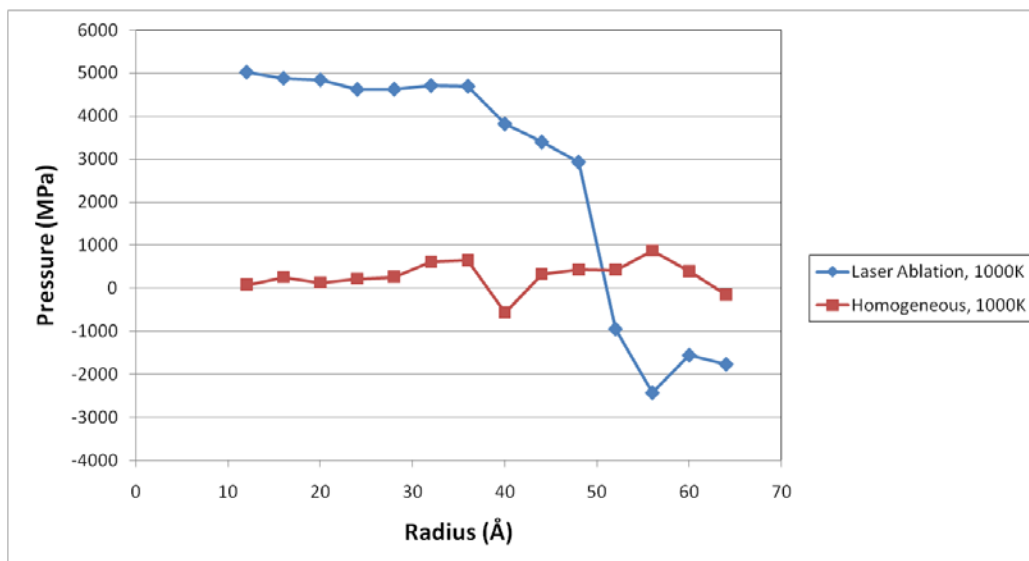


Figure 6.11: Pressure profile averaged over 8ps at 1000K for ambient heating and laser heating of 8.2nm core with 2nm crystalline oxide shell.

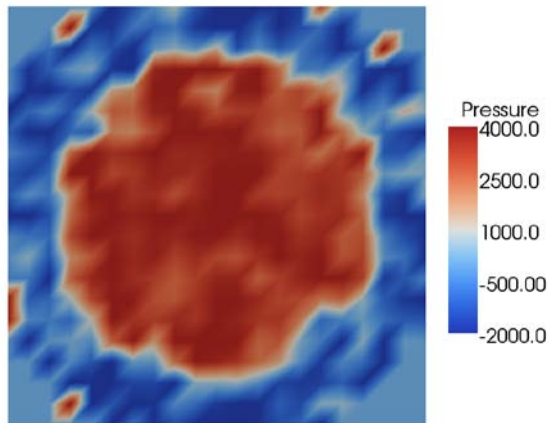


Figure 6.12: Cross section of 8.2nm core and oxide shell heated to 1000K by laser heating. Pressure units are MPa.

In order to visualize the steep pressure gradient at the core/shell interface we have computed the virial stress within 0.6nm voxels over 2ps intervals¹²⁹ for the 8.2nm core model. In Figure 6.12 a cross section of the 8.2nm core heated to 1000K by laser heating with a 2nm crystalline shell is shown. The abrupt change in pressure at the core/shell interface reflects the large pressure gradient observed in Figure 6.11. The core is experiencing high pressures because of the volumetric expansion upon melting while the oxide shell is under high negative pressure (tensile stress).

6.9 Analysis of the Size Dependency of Core Pressure

Here we have simulated the homogeneous flame heating of 5.6nm, 8.2nm, and 21nm aluminum cores with 2nm thick crystalline oxide shells. In Figure 6.13 the radial pressure results for these simulations are plotted.

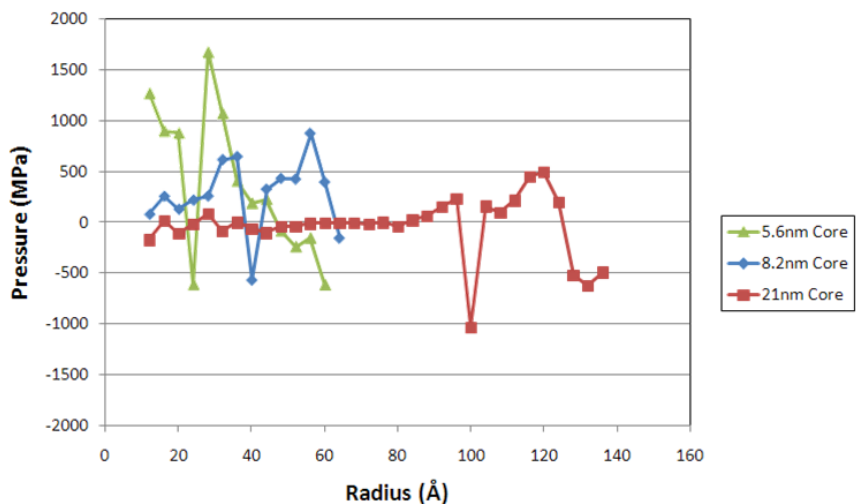


Figure 6.13: Plot of radial pressure for aluminum core sizes of 5.6nm, 8.2nm, and 21nm with 2nm crystalline aluminum oxide shells.

In Figure 6.13 a trend of either increasing or decreasing pressure is not apparent but in all cases the pressure values are much lower than those computed with the heterogeneous heating simulations, additionally mechanical failure is not observed.

6.10 Conclusions

For oxide coated aluminum nanoparticles with core radius to shell thickness ratios of up to 5 we have found that the oxidation process occurs by rapid diffusion of aluminum cations through the oxide shell as opposed to mechanical failure or melting of the oxide. For the range of nanoparticle sizes investigated here the results agree well with Levitas's mechanical analysis, i.e. shell failure does not occur for very small nanoparticles. Although the size at which diffusion is an important factor is not explicitly determined here the core size to shell thickness ratio required before mechanical failure of the oxide shell is determined to be over 5. The high computed diffusion

rates are not driven primarily by the volumetric expansion of the aluminum core but rather by the induced electric field in the oxide shell.¹²⁶

From the data collected here for core to shell ratios ($R_{\text{core}}/d_{\text{shell}}$) of 1.3 to 5.3 it is possible to make some observations. First, for homogeneously heated nanoparticles an extrapolation of the core size results would suggest that mechanical failure of the oxide is mitigated by fast diffusion of aluminum ions for core size larger than predicted by Levitas et al.^{108,109} Secondly, heterogeneous laser heating of oxide coated aluminum nanoparticles produces much higher pressures than observed by homogeneous flame heating of the oxide coated metal nanoparticle system. Finally, for thin shell oxide coated aluminum nanoparticles initial oxidation of the aluminum will likely occur by diffusion driven by an induced electric field as opposed to high pressures associated with the expansion of the aluminum melt and associated resulting mechanical failure of the oxide shell.

7 Conclusions and Future Work

7.1 Conclusions

The goal of this work was to investigate various metallic nanoparticle systems using computer simulation methods. Many interesting results were revealed including the effect of self-assembled monolayers on gold nanoparticles, quantification of the surface energy effect on sintering temperature for aluminum and nickel nanoparticles, and the magnitude of the induced electric field in oxide coated aluminum nanoparticles. Each of these findings resulted in a published contribution in their specific arenas.

In chapter 3 we found that the alkanethiolate coated gold nanoparticle system is metastable due to the negative surface tension at the gold/thiol interface. Even with the simulation limitations of short times and small particle sizes this result is important because we observed that the stability of the gold nanoparticle was more dependent upon the strength of the chain-chain interactions than the chain-gold interactions. This qualitative result may be used by experimentalists in planning experiments by helping to explain observations.

In chapter 4 the SHS reaction of Ni and Al nanoparticles was investigated and although the size of the reacting particles was determined to have some affect on the adiabatic combustion temperature. Although the nanoparticle size must be less than 10nm in order to increase the energy release from mixing alone by more than 10%. Reaction time was found to be exponentially dependent upon nanoparticle size with smaller nanoparticles whether initially separated or coated to react much faster than

larger nanoparticles. Another important observation during this investigation is the slow heating that occurs during stage two prior to melting of the nickel nanoparticle that is dependent upon particle size and gives way to rapid heating once the system temperature is high enough to melt the nickel core.

In chapters 5 and 6 we have determined that it is the self-induced electric field in oxide coated aluminum nanoparticles which explains why hollow aluminum oxide shells are formed during the controlled temperature oxidation of aluminum nanoparticles. This electric field and aluminum ion diffusion through the oxide shell is also predicted to limit the maximum stress in the oxide shell upon melting, therefore preventing mechanical failure of the oxide shell.

More generally I was able to make some conclusions about the use of MD simulations to study metallic nanoparticle systems undergoing environmental changes and chemical reactions. MD simulations allow users to investigate systems containing hundreds of thousands to millions of atoms with currently available commodity computer hardware, whereas more accurate methods such as *ab initio* can only support hundreds of atoms over even shorter time intervals. One of the greatest difficulties in applying MD simulations to metallic nanoparticle systems is determining the empirical potential forms to be used such as EAM, FS EAM, or ReaxFF. In addition, the parameter set used for a particular potential can affect the accuracy of the simulation results. The empirical potential parameters are fit to data sets obtained from experimental or *ab initio* simulation results. A researcher must be mindful of these limitations when considering the model and data to use for a simulation and in interpreting the simulation results.

7.2 Future Work

Each of the systems investigated in this dissertation have resulted in providing some answers while other questions were left unanswered due to computational limitations or because of time constraints. The first of these unanswered questions is the issue of the interaction of multiple alkanethiolate coated gold nanoparticles. It is conceivable that by using a more coarse-grained model of the gold core we could simulate many more nanoparticles in a single simulation but as we have shown, for small nanoparticles the gold core is appreciably affected by the coating itself, therefore a more accurate all atom model of the gold core is warranted. In addition, simulating a solvent such as water surrounding the gold nanoparticles would provide useful data on dispersion of gold nanoparticles coated with hydrophilic and hydrophobic coatings. The primary computational problem here is that accurately simulating water molecules would require much larger numbers of particles and more expensive empirical potentials possibly involving long range forces such as columbic interactions. I am currently investigating using an implicit solvent to solve this problem scale problem but the addition of Coulombic interactions would still increase the computational complexity of the problem considerably.

In the SHS reaction of aluminum and nickel, ambient oxygen was ignored because of model limitations. Currently, there is not an accurate empirical potential, such as ReaxFF, for the complete material system of nickel, aluminum, and oxygen. Even once this empirical potential is available the computational complexity will be much higher than the simple Ni/Al system because of the charge transfer involved during the oxidation reaction of Ni and Al. Reaching this goal is an important future

effort because SHS reactions typically occur under ambient conditions which includes atmospheric oxygen and even more likely oxide coated particles. The oxidation reaction is also expected to have a very large affect on the reaction rate and temperature due to the high enthalpy of oxidation for nickel and aluminum compared to the enthalpy of formation for NiAl.

Of immediate interest in the oxide coated aluminum arena is how the effect of the induced electric field scales with particle size. For instance, we do not know for certain how important the mass flux due to the electric field compared with the mass flux due to the internal pressures developed from melting of the aluminum core are. In order to make a direct comparison of our results with the melt dispersion mechanism^{108,109} would require simulating much larger nanoparticles. This direct comparison would require simulating nanoparticles of at least 10nm to 20nm in diameter with a 2nm or more thick oxide shell. Since the number of atoms scales with volume we would quickly reach over 10^6 atoms in a single model. This investigation is ongoing at this time.

In order to increase the applicability of MD simulations to ever increasing numbers of atoms I am currently investigating methods that hold the promise of higher computational capabilities beyond those provided by Moore's Law.¹³⁰ These methods include code optimizations and porting to nontraditional hardware such as GPGPUs (General Purpose Graphical Processing Units) and the Cell processor. From preliminary efforts, GPGPUs appear to hold the most promise of improved performance. Simply by porting the empirical potential computation in MD simulations such as the Lennard-Jones calculation to the GPGPU the overall simulation time was

cut by a factor of almost 5. Code optimizations have also been able to improve performance by 30%.¹³¹ A combination of these performance enhancing methods should give us the capabilities to achieve the simulation goals listed here.

8 References

1. Manna, A.; Imae, T.; Aoi, K.; Okazaki, M. *Mol. Sim.* **2003**, 29(10–11), 661–665.
2. Hong, R.; Han, G.; Fernández, J. M.; Kim, B.–J.; Forbes, N. S.; Rotello, V. M. *J. Am. Chem. Soc.* **2006**, 128, 1078–1079.
3. Frenkel, D.; Smit, B. *Understanding Molecular Simulations: From Algorithms to Applications*. Academic Press, San Diego, CA, 2002.
4. Allen, M. P.; Tildesley, D. J. *Computer Simulation of Liquids*. Oxford University Press Inc., New York, NY, 1987.
5. Haile, J.M. *Molecular Dynamics Simulations: Elementary Methods*. Wiley, New York, 1986.
6. Vipin Kumar, Ananth Grama, Anshul Gupta, and George Karypis. *Introduction to Parallel Computing: Design and Analysis of Algorithms*. Benjamin/Cummings, Reading, MA, 1994.
7. Ted G. Lewis and Hesham El-Rewini. *Introduction to Parallel Computing*. Prentice Hall, 1992.
8. Gene Golub and James M. Ortega. *Scientific Computing: An Introduction with Parallel Computing*. Academic Press, Inc., San Diego, CA, 1993
9. S. J. Plimpton. *J. of Comp. Phys.*, **117**:1–19, 1995.
10. J. A. Clarke and R. R. Namburu. *Concurrency Computat.: Pract. Exper.*, 14:1–14, 2002.
11. A. Henderson, J. Ahrens, C. Law, B. Geveci, and B. King. *The ParaView Guide: A Parallel Visualization Application*. Kitware, Inc., Clifton Park, NY, 2004.

12. E. Cuthill and J. McKee. Reducing the Bandwidth of Sparse Symmetric Matrices. In *Proceedings of the 24th National Conference*, pages 157–172. Association for Computing Machinery, 1969.
13. M. S. Daw and M. I. Baskes. *Phys. Rev. B*, **29**(12):6443–6453, 1984.
14. S. M. Foiles, M. I. Baskes, and M. S. Daw. *Phys. Rev. B*, **33**(12):7983–7991, 1986.
15. J. Mei, J.W. Davenport, and G.W. Fernando. *Phys. Rev. B*, **43**(6):4653–4658, 1991.
16. J. Mei, J.W. Davenport, and G.W. Fernando. *Phys. Rev. B*, **43**(6):4653–4658, 1991.
17. M. S. Stave, D. E. Sanders, T. J. Raeker, and A. E. DePristo. *J. of Chem. Phys.*, **93**(6):4413–4426, 1990.
18. T. J. Raeker and A. E. DePristo. *Int. Rev. Phys. Chem.*, **10**(1):1–54, 1991.
19. Zhang, L.; Goddard III, W. A.; Jiang, S. *Computers in Chem. Eng.* **2002**, 22(10), 1381–1385.
20. Landman, U.; Luedtke, W. D. *Faraday Discussions* **2004**, 125,1–22.
21. Luedtke, W. D.; Landman, U. *J. Phys. Chem.* **1996**, 100(32), 13323–13329.
22. Grönbeck, H.; Curioni, A.; Andreoni, W. *J. Am. Chem. Soc.* **2000**, 122, 3839–3842.
23. Mahaffy, R.; Bhatia, R.; Garrison, B. J. *J. Phys. Chem. B* **1997**, 101, 771–773.
24. Beardmore, K. M.; Kress, J. D.; Gronbeck-Jensen, N.; Bishop, A. R. *Chem. Phys. Lett.* **1998**, 286, 40–45.
25. Hautman, J.; Klein, M. L. *J. Chem. Phys.* **1989**, 91(8), 4944–5001.

26. Shevade, A. V.; Zhou, J.; Zin, M. T.; Jiang, S. *Langmuir* **2001**, *17*, 7566–7572.
27. Jiang, S. *Mol. Phys.* **2002**, *100*(14), 2261–2275.
28. K. S. S. Liu, C. W. Yong, B. J. Garrison, and J. C. Vickerman. *J. Phys. Chem. B*, **103**:3195–3205, 1999.
29. D. G. Castner, K. Hinds, and D. W. Grainger. *Langmuir*, **12**:5083–5086, 1996.
30. T. Ishida, N. Choi, W. Mizutani, H. Tokumoto, I. Kojima, H. Azebara, H. Hokari, U. Akiba, and M. Fujihira. *Langmuir*, **15**:6799–6806, 1999.
31. R. G. Nuzzo, B. R. Zegarski, and L. H. Dubois. *J. Am. Chem. Soc.*, **109**:733–740, 1987.
32. L. Strong and G. M. Whitesides. *Langmuir*, **4**:546–558, 1988.
33. B. Rai, P. Sathish, C. P. Malhotra, Pradip, and K. G. Ayappa. *Langmuir*, **20**:3138–3144, 2004.
34. F. Schreiber. *Prog. Surf. Sci.*, **65**:151–256, 2000.
35. W. L. Jorgensen, J. D. Madura, and C. J. Swenson. *J. Am. Chem. Soc.*, **106**:6638–6646, 1984.
36. H. Fukunaga, J. I. Takimoto, and M. Doi. *J. Chem. Phys.*, **116**(18):8183–8190, 2002.
37. V. Tries, W. Paul, J. Baschnagel, and K. Binder. *J. Chem. Phys.*, **106**(2):738–748, 1997.
38. P. K. Maiti, Y. Lansac, M. A. Glaser, and N. A. Clark. *Langmuir*, **18**:1908–1918, 2002.
39. H. C. Andersen. *J. Comp. Phys.*, **52**:24–34, 1983.

40. J. E. Angelo, N. R. Moody, and M. I. Baskes. *Model. Sim. Mater. Sci. Eng.*, **3**, 289–307, (1995).
41. Y. Mishin, M. J. Mehl, and D. A. Papaconstantopoulos. *Phys. Rev. B*, **65**, 224114, (2002).
42. Q. Zhang, T. Çağın, A. van Duin, W. A. Goddard III, Y. Qi, and L.G. Hector. *Phys. Rev. B*, **69**, 045423, 2004.
43. S. M. Thompson, K. E. Gubbins, J. P. R. B. Walton, R. A. R. Chantry, and J. S. Rowlinson. *J. Chem. Phys.* **81**, 530–542, 1984.
44. Cormier, J., Rickman, J. M. & Delph, T. J. *J. Appl. Phys.* **89**, 99-104, 2001.
45. Clausius, R. *Philos. Mag.* **40**, 122-127, 1870.
46. M. H. Magnusson, K. Deppert, J.-O. Malm, J.-O. Bovin, and L. Samuelson. *NanoStructured Materials*, **12**,45–48, 1999.
47. C.-L. Chiang. *J. Coll. Inter. Sci.*, **230**, 60–66, 2000.
48. Kim, J.-U.; Cha, S.-H.; Shin, K; Jho, J. Y.; and Lee, J.-C. *J. Am. Chem. Soc.* **127**(28):9962-9963, 2005.
49. J. R. Greer and W. D. Nix. *Appl. Phys. A*, **80**:1625–1629, 2005.
50. C. L. Cleveland, U. Landman, T. G. Schaaff, M. R. Shafiqullin, P. W. Stephens, and R. L. Whetten. *Phys. Rev. Lett.*, **79**(10): 1873–1876, 1997.
51. M. I. Baskes. *Phys. Rev. B*, **46**(5):2727–2742, 1997.
52. L. J. Lewis, P. Jensen, J. –L. Barrat. *Phys. Rev. B*, **56**(4):2248–2257, 1997.
53. A. W. Rosenbaum, M. A. Freedman, S. B. Darling, I. Popova, and S. J. Sibener. *J. Chem. Phys.*, **120**(8):3880–3886, 2004.
54. R. Bhatia and B. J. Garrison. *Langmuir*, **13**:765–769, 1997.

55. T. Hawa and M. R. Zachariah. *Phys. Rev. B*, **69**:035417, 2004.
56. T. Hawa and M. R. Zachariah. *Phys. Rev. B*, **71**:165434, 2005.
57. T. Hawa and M. R. Zachariah. *J. Chem. Phys.*, **121**(18):9043–9049, 2004.
58. H. Grönbeck, A. Curioni, and W. Andreoni. *J. Am. Chem. Soc.*, **122**:3839–3842, 2000.
59. C. L. Kelchner, D. M. Halstead, L. S. Perkins, N. M. Wallace, and A. E. DePristo. *Surf. Sci.*, **310**:425–435, 1994.
60. B. Lee and K. Cho. *Surf. Sci.*, **600**:1982–1990, 2006.
61. M. I. Haftel. *Phys. Rev. B*, **48**(4):2611–2622, 1993.
62. A. F. Voter and S. P. Chen. In *Characterization of Defects in Materials*, volume 82, page 175, Pittsburgh, 1987. Materials Research Society.
63. D. J. Lavrich, S. M. Wetterer, S. L. Bernasek, and G. Scoles. *J. Phys. Chem. B*, **102**:3456–3465, 1998.
64. S. S. Jang, Y. H. Jang, Y.-H. Kim, W. A. Goddard III, A. H. Flood, B. W. Laursen, H.-R. Tseng, J. F. Stoddart, J. O. Jeppesen, J. W. Choi, D. W. Steuerman, E. Delonno, and J. R. Heath. *J. Am. Chem. Soc.*, **127**:1563–1575, 2005.
65. G. Schmid. *Chem. Rev.*, **92**: 1709–1727, 1992.
66. A. Badia, L. Cuccia, L. Demers, F. Morin, and R. B. Lennox. *J. Am. Chem. Soc.*, **119**:2682–2692, 1997.
67. A. S. Dalton and E. G. Seebauer. *Surf. Sci.*, **601**: 728–734, 2007.
68. I. I. Suni. *Surf. Sci.*, **309**: L179–L183, 1995.
69. H. Sellers, A. Ulman, Y. Shnidman, J. E. Eilers. *J. Am. Chem. Soc.*, **115**:530–542, 1993.

70. M. R. Zachariah, M. J. Carrier, and E. Blaisten-Barojas. *J. of Phys. Chem.*, **100**:14856–14864, 1996.
71. J. S. Winn. *Phys. Chem.*, Addison Wesley, Boston, MA, 1995.
72. G. Lang. *Handbook of Chemistry and Physics, 55th edition*. CRC Press, Cleveland, OH, 1974.
73. G. E. Dieter. *Mechanical Metallurgy*. McGraw-Hill Inc., New York, NY, 1986.
74. Yu, M.; Bovet, N.; Satterley, C. J.; Bengio', S.; Lovelock, K. R. J.; Milligan, P. K.; Jones, R. G.; Woodruff, D. P.; Dhanak, V. *Phys. Rev. Lett.* 2006, **97**, 166102.
75. F. Schreiber. *J. of Phys.: Cond. Matt.*, **16**:R881–R900, 2004.
76. J. Hautman and M. L. Klein. *J. of Chem. Phys.*, **93**(10):7483–7492, 1990.
77. X. Phung, J. Groza, E. A. Stach, L. N. Williams, and S. B. Ritchey. *Mater. Sci. Eng. A*, **359**, 261–268, 2003.
78. A. Rai, D. Lee, K. Park, and M. R. Zachariah. *J. of Phys. Chem. B*, **108**, 14793–14795, 2004.
79. H. P. Li. *Mater. Sci. Eng. A*, **404**, 146–152, 2005.
80. S. Gennari, U. A. Tamburini, F. Maglia, G. Spinolo, and Z. A. Munir. *Acta Materialia*, **54**, 2343–2351, (2006).
81. P. Nash, and O. Kleppa. *J. All. Comp.*, **321**, 228–231, 2001.
82. R. Hu, and P. Nash. *J. Mater. Sci.*, **40**, 1067–1069, 2005.
83. J. C. Trenkle, T. P. Weihs, and T. C. Hufnagel. *Scripta Materialia*, **58**, 315–318, 2008.
84. S. Dong, P. Hou, H. Cheng, H. Yang, and G. Zou. *J. Phys.: Cond. Matt.*, **14**, 11023–11030, 2002.

85. T. Hawa, and M. R. Zachariah. *Aerosol Sci.*, **37**, 1–15, 2006.
86. M. R. Zachariah, and M. J. Carrier. *J. Aerosol Sci.*, **30**(9), 1139–1151, 1999.
87. S. H. Ehrman. *J. Coll. Inter. Sci.*, **213**, 258–261, 1999.
88. S. Arcidiacono, N. R. Bieri, D. Poulikakos, and C. P. Grigoropoulos. *Int. J. Multiphase Flow*, **30**, 979–994, 2004.
89. S. Yu, C.-Y. Wang, T. Yu, and J. Cai. *Physica B*, **396**, 138–144, 2007.
90. J. Mei, B. R. Cooper, and S. P. Lim. *Phys. Rev. B*, **54**(1), 178–183, 1996.
91. F. Delogu. *Nanotechnology*, **18**, 505702, 2007.
92. H. X. Zhu, and R. Abbaschian. *J. Mater. Sci.*, **38**, 3861–3870, 2003.
93. M. W. Finnis and J. E. Sinclair. *Philos. Mag. A*, **50**, 45–55 (1984).
94. G. J. Ackland, and V. Vitek. *Phys. Rev. B*, **41**(15), 10324–10333, 1990.
95. P. Pawlow. *Z Phys. Chem.*, **65**, 545, 1909.
96. P. Zhu, J. C. M. Li, and C. T. Liu. *Mater. Sci. Eng. A*, **357**, 248–257, 2003.
97. R. Arroyave, D. Shin, and Z.-K. Liu. *Acta Materialia*, **53**, 1809–1819, 2005.
98. F. Z. Chrifi-Alaoui, M. Nassik, K. Mahdouk, and J. C. Gachon. *J. All. Comp.*, **364**, 121–126, 2004.
99. V. I. Nizhenko. *Powder Metallurgy and Metal Ceramics*, **43**(5–6), 273–279 (2004).
100. A. Y. Lozovoi, A. Alavi, and M. W. Finnis. *Phys. Rev. Lett.*, **85**(3), 610–613, 2000.
101. O. Kubaschewski, *Materials Thermochemistry*, 6th ed., Pergamon Press, New York, 1993, p. 299.

102. D. Mukherjee, C. G. Sonwane, and M. R. Zachariah. *J. Chem. Phys.*, **119**, 3391, 2003.
103. J. Frenkel. *J. Phys.*, **9**, 385, (1945).
104. M. A. Assael, K. Kakosimos, R. M. Banish, J. Brillo, I. Egry, R. Brooks, P. N. Qusted, K. C. Mills, A. Nagashima, Y. Sato, and W. A. Wakeham. *J. Phys. Chem. Ref. Data*, **35**(1), 285–300, (2006).
105. S. Zhao, T. C. Germann, and A. Strachan. *J. of Chem. Phys.*, **125**, 164707, (2006).
106. J.H. Sinfelt. *Bimetallic Catalysis: Discoveries, Concepts and Applications*. Wiley, New York, 1983.
107. J. Uppenbrink and David J. Wales. *J. of Chem. Phys.*, **96**(11), 8520–8534, 1992.
108. V.I. Levitas, B.W. Asay, S.F. Son, and M. Pantoya. *J. of Appl. Phys.*, **89**, 071909, 2006.
109. V.I. Levitas, B.W. Asay, S.F. Son, and M. Pantoya. *J. of Appl. Phys.*, **101**, 083524, 2007.
110. P. Puri and V. Yang. “Thermo-Mechanical Behavior of Nano Aluminum Particles with Oxide Layers”, 46th AIAA Aerospace Sciences Meeting and Exhibit, Reno, NV, 7-10 January 2008.
111. A. Rai, K. Park, L. Zhou, and M.R. Zachariah. *Comb. Theor. Model.*, **10**(5), 843–859, 2006.
112. R. Nakamura, D. Tokozakura, H. Nakajima, J.-G. Lee, and H. Mori. *J. of Appl. Phys.*, **101**, 074303, 2007.

113. N. Cabrera and N.F. Mott. *Rep. Prog. Phys.*, **12**, 163–184, 1948.
114. A.T. Fromhold, jr, and E.L. Cook. *Phys. Rev.*, **163**(3), 650–664, 1967.
115. C. Wagner. *Z. Phys. Chem.*, **B21**, 25, 1933.
116. L.P.H. Jeurgens, W.G. Sloof, F.D. Tichelaar, and E.J. Mittemeijer. *J. of Appl. Phys.*, **92**(3), 1649–1656, 2002.
117. A.C.T. van Duin, S. Dasgupta, F. Lorant, and W.A. Goddard III. *J. of Phys. Chem. A*, **105**, 9396–9409, 2001.
118. F.H. Streitz and J.W. Mintmire. *Phys. Rev. B*, **50**(16), 11996–12003, 1994.
119. N. Pradeep, D.I. Kim, J. Grobelny, T. Hawa, B.J. Henz, and M.R. Zachariah, *Appl. Phys. Lett.*, **91**, 203114, 2007.
120. S. Ogata, H. Iyetomi, K. Tsuruta, F. Shimojo, A. Nakano, R.K. Kalia, and P. Vashishta. *J. of Appl. Phys.*, **88**(10), 6011–6015, 2000.
121. P.P. Mitra, P.N. Sen, L.M. Schwartz, P. Le Doussal. *Phys. Rev. Lett.*, **68**(24), 3555–3558, 1992.
122. V.P. Zhdanov and B. Kasemo. *Chem. Phys. Lett.*, **452**, 285–288, 2008.
123. C.G. Zoski. *Handbook of Electrochemistry*. Elsevier, 2007.
124. J. Dalla Torre, J.-L. Bocquet, Y. Limoge, J.-P. Crocombette, E. Adam, G. Martin, T. Baron, P. Rivallin, and P. Mur. *J. Appl. Phys.*, **92**(2), 1084–1094, 2002.
125. V. Zhukov, I. Popova, and J.T. Yates. *Surf. Sci.*, **441**, 251, 1999.
126. B.J. Henz, T. Hawa, and M.R. Zachariah. *J. of Chem. Phys.*, Submitted for publication.
127. L. Zhou, A. Rai, and M.R. Zachariah. *Int. J. Mass Spec.*, **258**, 104–112, 2006.

128. L. Zhou, K. Park, H. Milchberg, and M.R. Zachariah. *Aeros. Sci. Tech.*, **41**, 818–827, 2007.
129. T.J. Campbell, G. Aral, S. Ogata, R.K. Kalia, A. Nakano, and P. Vashishta. *Phys. Rev. B*, **71**, 205413, 2005.
130. G.E. Moore. *Electronics Magazine*, **38**(8), 1965.
131. J. Fischer, V. Natoli, D. Richie. “Optimization of LAMMPS”, HPCMP Users Group Conference, Denver CO, June 26-29, 2006.